

University of Nebraska - Lincoln

DigitalCommons@University of Nebraska - Lincoln

---

Mechanical (and Materials) Engineering --  
Dissertations, Theses, and Student Research

Mechanical & Materials Engineering, Department  
of

---

4-2017

# Oxidation of $Ti_2AlC$ in High Temperature Steam Environment

Ziyad M. Smoqi

University of Nebraska-Lincoln, [zsmoqi@huskers.unl.edu](mailto:zsmoqi@huskers.unl.edu)

Follow this and additional works at: <http://digitalcommons.unl.edu/mechengdiss>



Part of the [Applied Mechanics Commons](#)

---

Smoqi, Ziyad M., "Oxidation of  $Ti_2AlC$  in High Temperature Steam Environment" (2017). *Mechanical (and Materials) Engineering -- Dissertations, Theses, and Student Research*. 120.

<http://digitalcommons.unl.edu/mechengdiss/120>

This Article is brought to you for free and open access by the Mechanical & Materials Engineering, Department of at DigitalCommons@University of Nebraska - Lincoln. It has been accepted for inclusion in Mechanical (and Materials) Engineering -- Dissertations, Theses, and Student Research by an authorized administrator of DigitalCommons@University of Nebraska - Lincoln.

**OXIDATION OF Ti<sub>2</sub>AlC IN HIGH TEMPERATURE STEAM ENVIRONMENT**

by

Ziyad Smoqi

A THESIS

Presented to the Faculty of  
The Graduate College at the University of Nebraska  
In Partial Fulfillment of Requirements  
For the Degree of Master of Science

Major: Mechanical Engineering and Applied Mechanics

Under the Supervision of Professor Bai Cui

Lincoln, Nebraska

April, 2017

# OXIDATION OF Ti<sub>2</sub>AlC IN HIGH TEMPERATURE STEAM ENVIRONMENT

Ziyad Smoqi, M.S

University of Nebraska 2017

Advisor: Bai Cui

High temperature oxidation of fuel cladding materials, during the loss of coolant accident (LOCA), is of utmost importance for next-generation nuclear energy systems. Ti<sub>2</sub>AlC is a promising candidate material for nuclear applications due to its outstanding properties such as thermal stability at high temperatures, oxidation resistance in air, thermal shock resistance, low neutron absorption cross-section, and the resistance to irradiation-induced amorphization. In this research, high temperature steam oxidation experiments were conducted to evaluate the oxidation resistance of Ti<sub>2</sub>AlC in LOCA conditions. After oxidation in 100% steam at 600 and 800°C, the oxidation kinetics followed a parabolic rate law while it followed a cubic rate law at 1000°C. The oxide microstructure initially consisted of a thin, discontinuous outer layer of TiO<sub>2</sub> and a continuous inner layer of Al<sub>2</sub>O<sub>3</sub>. As the temperature was increased, the concentration of Al<sub>2</sub>O<sub>3</sub> increased in the outer scale, resulting in an excellent oxidation resistance. The steam flow rate accelerates the oxidation kinetics, and this effect is the greatest at 600°C, at which the oxide scale is porous and cracked. This was likely attributed to stresses generated in the oxide scale due to the phase transformation of TiO<sub>2</sub> from anatase to rutile phase.

## **ACKNOWLEDGMENTS**

I would like to express my sincere appreciation to my advisor Professor Cui for his advice and continual encouragement throughout the last two year at UNL. When I first started to think about doing research, I could never imagine how the first step will take place. However, meeting such an excellent, flexible, and open-minded advisor increased my momentum and taught me how to learn things step-by-step under a minimal pressure environment. Without his assistance, this thesis would have not been completed successfully.

I am so lucky to have such committee members including Professor Bai Cui, Professor Jeff Shield, and Professor Michael Nastasi who gladly agreed to be on my committee. Two years ago, I would never imagine that I would have real scientists such as them on my committee. Their valuable time, guidelines, and suggestions will be forever highly appreciated.

Next, I would like to especially thank Professor Eveline Baesu, who was the first person I met at the UNL. Her suggestions, advice, and most importantly her willingness to help played the biggest role in my academic life. I'll never forget the day she welcomed me and introduced me to the other extraordinary UNL faculty members with different research backgrounds. That was a vital key to my success!

I would have never been able to do my experiments so confidently without all the help I received from Fei Wang. He always made himself available to teach me how to use different materials processing and characterization techniques. I am so glad to have him in my group with all other helpful group members. I am so proud to have joined this

extremely knowledgeable group. So, I would like to thank every member of this group from the bottom of my heart for their immense assistance, advice, and sharing of information. I would also like to acknowledge the faculty members at NCMN and NERCF facilities who provided me with all the required training.

I am very grateful to my fellow board members of Yazda, a non-profit organization founded to prevent future genocides against Yazidi people, for their courage and continual support throughout my master's program. While I was busy with my studying, every member in this organization worked tirelessly calling on world to bring justice to the Yazidi case. I am so proud of being on the board with them, and very proud of the fabulous job they have done in the past two years.

Last but not least, I would like to thank my wife Thaura and children Awaz, Azad, and Hivi for their endless support and patience. These people were fantastic; they lived independently providing me with gigantic amounts of time in the past two years. They all shared the difficulties I faced during my studying and encouraged me to overcome all obstacles when I was overwhelmed.

## TABLE OF CONTENTS

<b>1. INTRODUCTION .....</b>	<b>1</b>
1.1. Overview of Nuclear Reactors .....	1
1.2. Classification of Nuclear Reactors .....	5
1.3. Fuel Rods.....	6
1.4. Fuel Cladding Materials. ....	7
1.5. Accident-Tolerant Fuels (ATF) for LWRs.....	10
<b>2. LITERATURE REVIEW .....</b>	<b>13</b>
2.1. Oxidation of Zirconium Alloys (Zircalloys) .....	13
2.1.1. <i>Zircalloys</i> .....	13
2.1.2. <i>Loss of Coolant Accident (LOCA)</i> .....	16
2.1.3. <i>Oxidation of Zircalloys in Water</i> .....	16
2.1.4. <i>Oxidation of Zircalloys in Steam</i> .....	20
2.1.5. <i>Oxidation of Zircalloys in Air</i> .....	24
2.2. High Temperature Oxidation of $Ti_2AlC$ MAX-phase.....	27
2.2.1. <i><math>Ti_2AlC</math> MAX-phase</i> .....	27
2.2.2. <i>Oxidation Kinetics of <math>Ti_2AlC</math> in Steam</i> .....	30
2.2.3. <i>Oxidation Kinetics of <math>T_2AlC</math> in Air</i> .....	35
2.2.4. <i>Phase Evolution during High Temperature Oxidation of <math>Ti_2AlC</math></i> .....	36
2.2.5. <i>Microstructural Evolution during High Temperature Oxidation of <math>Ti_2AlC</math></i>	37
2.2.6. <i>High Temperature Oxidation Mechanism of <math>Ti_2AlC</math></i> .....	43
<b>3. EXPERIMENTAL PROCEDURES .....</b>	<b>46</b>
3.1. Samples Processing Techniques.....	46
3.1.1. <i>Laser Shock Penning (LSP)</i> .....	46
3.1.2. <i>Tube Furnace with Steam Capability</i> .....	48
3.2. Oxidation Studies .....	50
3.2.1. <i>Zicaloy-2 (Zry-2)</i> .....	50
3.2.2. <i><math>Ti_2AlC</math></i> .....	52
3.3. Characterization Methods .....	53
3.3.1. <i>Scanning Electron Microscopy (SEM)</i> .....	54
3.3.2. <i>Energy Dispersive X-Ray Spectroscopy (EDS)</i> .....	57

3.3.3. <i>Focused Ion Beam (FIB)</i> .....	58
<b>4.    HIGH TEMPERATURE OXIDATION OF ZIRCALOY-2 (Zry-2)</b> .....	<b>60</b>
4.1.    Oxidation Behavior of Zry-2 Samples Oxidized in the flowing Steam at 600, 800, 1000°C .....	60
4.2.    Oxidation Behavior of Zry-2 Samples Oxidized at 600°C in Air .....	72
4.3.    Oxidation Kinetics of LSP and Untreated Samples at 600°C in Air .....	79
4.4.    Effect of LSP on Zry-2 Samples .....	83
4.5.    Summary .....	85
<b>5.    HIGH TEMPERATURE OXIDATION OF Ti<sub>2</sub>AlC</b> .....	<b>86</b>
5.1.    Oxidation Behavior of Ti <sub>2</sub> AlC at 600, 800, 1000°C in the Flowing Steam .....	86
5.1.1. <i>Oxidation Kinetics</i> .....	86
5.1.2. <i>Microstructural Evolution of the Scales with Temperature</i> .....	91
5.1.3. <i>Oxidation Mechanism</i> .....	101
5.2.    Effect of Steam Flow Rate on the Oxidation Behavior of Ti <sub>2</sub> AlC at Different Temperatures .....	104
5.3.    Comparison of the Oxidation Kinetics of Zircaloy-2 (Zry-2) and Ti <sub>2</sub> AlC .....	117
5.4.    Summary .....	121
<b>6.    CONCLUSION</b> .....	<b>122</b>
<b>7.    FUTURE WORK</b> .....	<b>124</b>
<b>8.    REFERENCES</b> .....	<b>126</b>
<b>9.    LIST OF PUBLICATIONS</b> .....	<b>134</b>

## LIST OF TABLES

<b>Table 1.1.</b> Neutron Absorption Cross Section for Pure Elements (measured in Barns) ....	9
<b>Table 2.1.</b> Chemical Composition of Zircaloy-2 and Zircaloy-4.....	15
<b>Table 2.2.</b> Cubic Oxidation Constants and Activation Energy .....	33
<b>Table 4.1.</b> Oxidation kinetics constants and breakaway oxidation points for Zry-2 in steam at different temperatures .....	64
<b>Table 5.1.</b> Kinetics rate constants for samples oxidized at different temperature in the flowing steam at 50 mg/s. ....	91
<b>Table 5.2.</b> Comparison between kinetics rate constants at different flow rates of steam. ....	106

## LIST OF FIGURES

<b>Figure 1.1.</b> Generations of nuclear power plants [4].....	3
<b>Figure 1.2.</b> Major requirements of advanced accident-tolerant fuel system (ATF) [24].	11
<b>Figure 2.1.</b> Schematic representation of the corrosion of the zirconium alloys [42].	18
<b>Figure 2.2.</b> Typical oxidation curve of zircaloy at 320°C, adopted from Rion et al. [43]. .....	19
<b>Figure 2.3.</b> Schematic illustration of microstructural evolution of zirconium oxide films prior to the transition of oxidation kinetics [56].	21
<b>Figure 2.4.</b> Crystal structure of Ti <sub>2</sub> AlC with its atomic configurations in the unit cell [70] .....	28
<b>Figure 2.5.</b> SEM images of surface morphology of Ti <sub>2</sub> AlC oxidized at 1400°C [84].	40
<b>Figure 2.6.</b> (a) SEM cross-sectional view of Ti <sub>2</sub> AlC oxidized in air at 1000°C, (b) EDS line-scanning profiles along the black arrow in (a), and (c) EDS line-scanning profiles along the gray arrow in (a) [84].	42
<b>Figure 3.1.</b> Schematic representation of the principle of laser shock processing [98].	47
<b>Figure 3.2.</b> Schematic diagram of the experimental set up for high temperature steam oxidation study.....	49
<b>Figure 3.3.</b> Schematic representation of electron beam interactions, including the relative depths from which various signals can escape the surface [100].	55
<b>Figure 3.4.</b> (a) FEI Nova NanoSEM 450 [101], (b) FEI Helios NanoLab 660 [102].	57
<b>Figure 3.5.</b> Schematic representation two-beam (electron and ion) FIB [100].	59
<b>Figure 4.1.</b> Oxidation behavior of Zry-2 in steam at: (a) 600°C, (b) 800°C, (c) 1000°C, (d) 600, 800, and 1000°C.	62
<b>Figure 4.2.</b> (a), (c), (e) Squares of weight gain as a function of time for pre-transition kinetics at 600, 800, and 1000°C, respectively; and (b), (d), and (f) weight gain as a function of time for post-transition kinetics at 600, 800, and 1000°C, respectively.....	63
<b>Figure 4.3.</b> SEM images of the oxide scale formed on the surface of Zry-2 after breakaway oxidation at (a) 600°C for 133,000s (~37h), (b) 800°C for 37,000s (~10 h), and (c) 1000°C for 18960s (~5h).	65
<b>Figure 4.4.</b> Cross sectional SEM SE micrographs of Zry-2 oxidized in steam at (a) 600°C for 133,000s (~37h), (b) 800°C for 37,000s (~10 h), and (c) 1000°C for 18960s (~5h).	68
<b>Figure 4.5.</b> (a) SEM micrograph of the oxide scale from on the surface of Zry-2 oxidized in steam at 800C (b) EDS spectrum of the intact area shown in (a), and (c) EDS spectrum of the cracked area in (a).....	70

<b>Figure 4.6.</b> (a) Cross-sectional SEM micrograph of Zry-2 after oxidation at 600°C for 133,000s (~37h) in a flowing steam at 100 mg/s. (b) EDS line-scanning profiles along the line shown in (a). Note: Roi means region of interest counts. ....	71
<b>Figure 4.7.</b> Weight gain per unit surface area as a function of time for Zry-2 oxidized in air at 600C.....	73
<b>Figure 4.8.</b> Photographs of partially oxidized Zry-2 samples in air at 600°C after oxidation for the indicated times.....	74
<b>Figure 4.9.</b> SEM SE images of the oxide scale formed on the surface of Zry-2 oxidized in air at 600°C for (a) 5500s, (b) 10000s, and (c) 16600s.....	77
<b>Figure 4.10.</b> SEM SE image of the fracture cross-section of the external part of the oxide scale formed on Zry-2 after oxidation in air at 600°C for 16,600s. ....	78
<b>Figure 4.11.</b> Oxidation kinetics curves of an as received Zry-2 sample (Sample 1) in comparison with a pre-oxidation LSP treated Zry-2 sample (Sample 2) and a post-oxidation LSP treated Zry-2 sample (Sample 3) in air at 600°C. ....	81
<b>Figure 4.12.</b> Difference in the oxidation rate kinetics constants between LSP treated and untreated Zry-2 samples after the breakaway oxidation in air at 600°C for ~ 6 h and 15 min. ....	82
<b>Figure 4.13</b> Photographs show the difference in surface appearance between LSP treated and untreated Zry-2 samples after oxidation in air at 600°C for ~ 6h and 15 min. ....	84
<b>Figure 5.1.</b> Plots of weight gain of Ti <sub>2</sub> AlC per unit surface area as a function of exposure time at 600, 800, and 1000°C in the flowing steam at 50 mg/s. ....	87
<b>Figure 5.2.</b> (a) square of the weight gains verses exposure time of Ti <sub>2</sub> AlC at 600 and 800°C, and (b) and (c) cube and square of the weight gain verses exposure time of Ti <sub>2</sub> AlC at 1000°C.....	89
<b>Figure 5.3.</b> SEM BSE micrographs showing surface morphology of Ti <sub>2</sub> AlC samples oxidized in steam at: (a) 600°C, (b) 800°C, and (c) 1000°C. ....	92
<b>Figure 5.4.</b> (a) SEM BSE image of the polished cross-sectional view of Ti <sub>2</sub> AlC oxidized at 600°C in the flowing steam at 50 mg/s for 37 h; (b) a EDS line scan results along the green line as shown in (a) .....	95
<b>Figure 5.5.</b> (a) SEM BSE image of the polished cross-sectional view of Ti <sub>2</sub> AlC oxidized at 800°C in the flowing steam at 50 mg/s for 30 h; (b) a EDS line scan results along the green line as shown in (a) .....	96
<b>Figure 5.6.</b> (a) SEM BSE image of the FIB exposed cross-sectional view of Ti <sub>2</sub> AlC oxidized at 1000°C in the flowing steam at 50 mg/s for 15 h; (b) a EDS line scan results along the green line as shown in (a).....	97

<b>Figure 5.7.</b> SEM BSE micrograph showing the cross section of the oxide scale formed on Ti <sub>2</sub> AlC after oxidation in steam at (a) 600°C for 37 h, (b) 800° for 30 h, and (c) 1000°C for 15 h. ....	99
<b>Figure 5.8.</b> Oxidation kinetics of Ti <sub>2</sub> AlC oxidized in flowing steam at 50 mg/s (dashed lines) and 100 mg/s (solid lines). ....	104
<b>Figure 5.9.</b> SEM SE micrographs showing surface morphology of Ti <sub>2</sub> AlC oxidized at 600C: (a) High flow rate steam, and (b) low flow rate steam.....	107
<b>Figure 5.10.</b> SEM SE micrographs showing the surface morphology of Ti <sub>2</sub> AlC oxidized at 600C: (a) Before, and (b) After breakaway. ....	109
<b>Figure 5.11.</b> Typical SEM micrographs of the surface of Ti <sub>2</sub> AlC samples oxidized in the flowing steam at 100 mg/s (a) at 800°C, and (b) at 1000°C. ....	110
<b>Figure 5.12.</b> (a) SEM image of the polished cross-sectional view of Ti <sub>2</sub> AlC oxidized at 600°C in the flowing steam at 100 mg/s for 37 h; (b) EDS line scan results along the green line as shown in (a). ....	113
<b>Figure 5.13.</b> (a) SEM image of the polished cross-sectional view of Ti <sub>2</sub> AlC oxidized at 800°C in the flowing steam at 100 mg/s for 30 h; (b) EDS line scan results along the green line as shown in (a). ....	114
<b>Figure 5.14.</b> (a) SEM image of the polished cross-sectional view of Ti <sub>2</sub> AlC oxidized at 1000°C in the flowing steam at 100 mg/s for 15 h; (b) EDS line scan results along the green line as shown in (a). ....	115
<b>Figure 5.15.</b> Comparison of the oxidation kinetics of Ti <sub>2</sub> AlC and Zry-2 in steam at (a) 600, (b) 800, and (c) 1000°C.....	119

## 1. INTRODUCTION

### 1.1. Overview of Nuclear Reactors

The utilization of nuclear energy for benign applications, such as nuclear power plants to produce electricity, was an absolute breakthrough in the human history. The innovation and development of nuclear power plants came as a direct result of volatile fossil fuel prices, global climate changes due to greenhouse gas emissions, and the concern about the depletion of other energy resources in the future. This, in addition to other economic factors, has played a major role in increasing the scientific research effort to develop and assess the security measures pertaining to this technology. Consequently, the future of nuclear power reactors looks very promising.

In nuclear power plants, nuclear reactions are used to generate heat that boils the water, generate steam, and spin the steam turbines that are connected to generators, producing electricity. The development of nuclear power reactors over the past 60 years has resulted in more than three generations of system designs (**Figure 1.1**). Generation-I designs refer to the early prototype and unique system of nuclear reactors used for civil nuclear power. The world's first full-scale electricity-generating nuclear power plant was the Shippingport Atomic Power Station in Pennsylvania, United States [1]. One month after it was launched, the reactor reached an output capability of 60 Megawatts Electric (MWe) and the critical design power was achieved in 1957 [2]. The Shippingport reactor used ordinary water as a coolant to cool the reactor core during the chain reaction and thus classified as a light-water reactor. The success of Shippingport paved the way for

many private industries to develop light-water reactors (LWR) for commercial use while federal nuclear energy programs became more concerned about developing other forms of nuclear reactors [1]. This resulted in a new, more reliable and economical generation referred to as Generation-II, which includes commercial power reactors such as pressurized water reactors (PWRs), boiling water reactors (BWRs), Canada Deuterium Uranium reactors (CANDU) and advanced gas-cooled reactors (AGR). These reactors use traditional safety systems that can be operated automatically involving electrical or mechanical operations or by the operator of the nuclear reactors [3]. This generation started in the 1960s, and some are still in use by the major companies such as General Electric (GE) and Westinghouse [3].

Generation-III reactors were developed from Generation-II with some major improvements in the areas of fuel and safety systems, efficiency, and construction to increase the operational life (60+ years) [3]. Similarly, Generation-III+ reactors began after further significant improvements in the safety system of Generation-III designs in the 1990s. The major improvement of Generation-III+ designs over Generation-III designs includes the incorporation of more passive safety features, which rely on phenomenon such as gravity and natural convection during abnormal events, over active safety features, which require operator intervention [3]. Finally, the International Generation-IV Initiative, established in 2000 and guided by the Generation-IV International Forum (GIF), is seeking development of a new generation of nuclear reactor system [4]. The aim of Generation IV nuclear reactor design is to improve efficiency, enhance safety, minimize waste, and increase proliferation resistance for commercial development by 2020-2030 [4].

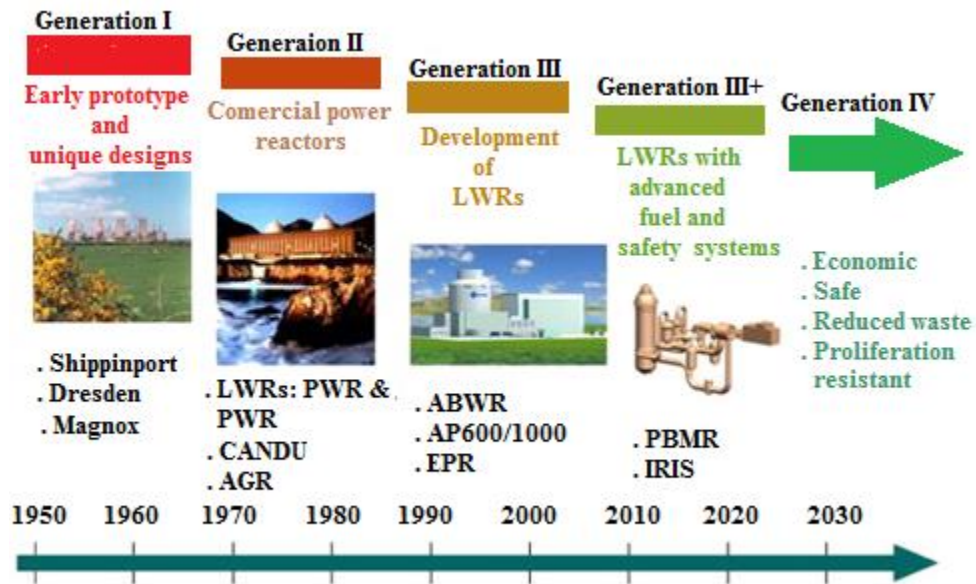


**Figure 1.1.** Generations of nuclear power plants [4]

The perceived importance of nuclear reactors and demand for nuclear power has changed several times over the past 50 years [5]. In the 1960s, the advancement of nuclear power plants in the United States increased rapidly because the nuclear power was considered economically competitive and environmentally friendly by the utility companies. In the 1970s and 1980s, however, the realization of nuclear issues such as potential nuclear hazards and radioactive waste disposal raised some unfavorable attitudes [1, 2]. Even then, the United States ranked as the leading country with the greatest number of operating nuclear reactors, supplying a significant percentage of the total electricity produced in the country [1].

The prospect of nuclear power plants in the United States is currently very bright. The economic performance and necessary safety precautions taken regarding major nuclear accidents are exceptional. More advanced nuclear reactors, with novel and

carefully engineered designs, have been constructed to make them simpler and safer, especially after the accidental partial reactor core meltdown at Three Mile Island in the United States in 1979 and at the Chyrnobl Nuclear Power Plant in the Ukraine in 1982 [6]. Even the economic and safety regulations of nuclear power are being modified significantly to develop a better economic framework for future nuclear power plants, and the authorizations to operate the plants are being extended to 60 years [7].

The increasing capacity of electricity generation from nuclear energy since 1980 is a significant indication of the excellent economic performance of nuclear power plants in the United States. The number of nuclear reactors in the United States as of today is 100 reactors with 4 additional reactors under construction. These reactors are located in 30 different states and managed by 30 different power companies [2]. The contribution of these reactors to the total electricity supplied in 2015 reached 20 percent (798 billion kWh), and the average capacity factor since 2001 had dramatically increased to reach more than 90% [2].

Nuclear power plants are the key to combating global warming through the stabilization of greenhouse gas emissions and as an economical source of energy. So, the research effort should expand to continuously improve the reactors and reduce the causes of their accidents. Though there are several factors such as public perception of safety and proliferation risk that generate some unfavorable attitudes towards increasing the number of nuclear power plants, the new reactor designs are expected to reduce most of these concerns [6].

## 1.2. Classification of Nuclear Reactors

In order to fully grasp the focus of this thesis, it's imperative to possess a fundamental understanding of the most widely used nuclear power reactor types along with the common issues that might lead to their failure. After exploiting nuclear energy for benign applications, there have been many reactor systems proposed and developed for commercial use to produce electricity around the world [7]. These reactors have been classified by several methods such as the type of fission reaction, moderator material, coolant ...etc. Exothermal reactions, which release an enormous amount of heat, are fission and fusion reactions. Nuclear fission occurs when the nucleus of a particle splits while nuclear fusion occurs when particles collide within a nuclear reactor [9, 10]. Here, neutrons from fission play a major role in maintaining the chain reaction. Fission reactors are either called thermal reactors (when neutrons have low energy) or fast reactors (when neutrons have high energy). Thermal reactors are generally favored over the fast reactors in most of the commercial power reactors since the thermal neutron fission of  $^{235}\text{U}$  is more probable than fast neutron fission by more than three orders of magnitude [11]. There are also heavy and light-water reactors depending on type of moderator. The early developed systems of nuclear power used graphite or heavy-water as moderators because these are the only moderators that enable the use of natural uranium containing 0.711 wt. %  $^{235}\text{U}$  as fuel [8]. However, the use of other moderators namely light water requires the enrichment of uranium to approximately 3 wt. %  $^{235}\text{U}$  to maintain the criticality as a fuel [8].

In the United States, the nuclear power plants in commercial operation to generate electricity are light-water reactors which include Pressurized Water Reactors (PWRs) and Boiling Water Reactors (BWRs) [2, 8, 12]. Out of currently 100 nuclear reactors licensed to operate in the United States, 66 are PWRs and 34 are BWRs [12]. The major difference between PWRs and BWRs is the steam generation process. In PWRs, the design is distinguished by having a primary water loop which circulates through the reactor to remove heat generated by the core. The water in the primary loop is always maintained at a high pressure to prevent it from boiling. Then, the primary loop water generates steam in a secondary water loop which drives the turbine and produces electricity [2, 8, 11]. On the other hand, BWRs have only one loop. The water which passes over the reactor core is allowed to boil, and the steam generated is used directly to drive the turbine. Both PWRs and BWRs use enriched uranium dioxide as fuel and have comparable fuel assemblies [11].

### **1.3. Fuel Rods**

After being familiar with fundamental information about the importance of nuclear power reactors and classification of these reactors, including a brief description of the two major types of nuclear power reactors used in the United States, the rest of this chapter is now centered on the fuel rods, which is the focus of this thesis. Nuclear fuel rods are the source of energy in nuclear power plants. They contain fuel pellets and all fission processes that release a huge amount of clean energy used to produce electricity.

In the United States, uranium undergoes different chemical and physical processes to produce nuclear fuel [13]. The final step in this process is called fabrication, which begins after the conversion of uranium ore into uranium hexafluoride  $UF_6$  and the enrichment of  $UF_6$  in  $^{235}U$  [14]. Enriched  $UF_6$  gas is chemically converted into uranium dioxide ( $UO_2$ ) powder, which is then sintered into small cylindrical pellets of approximately 1 cm diameter and 1.5 cm long. Finally, the finished pellets are loaded into long tubes made of materials called “cladding” and welded closed at both ends to form fuel rods [13, 15]. Numerous fuel rods are bundled together to form fuel assemblies that can be lifted into and out of a reactor core.

#### **1.4. Fuel Cladding Materials.**

The cladding material is one of the most important components of nuclear reactors; it acts as a major safety barrier that prevents the release of radioactive fission products during the nuclear chain reaction into the coolant/moderator [14, 17]. Consequently, it reduces the risk of leaking of radioactive isotopes and dangerous gases produced, such as Xenon and Krypton into the atmosphere. Meanwhile, the material chosen for this purpose is exposed to a harsh environment, and it requires some unique properties to survive such an environment and to maintain its protective quality during reactor operation and remain economical.

In general, the selection of material for fuel cladding is a bit challenging and requires multiple design constraints that mainly include the following [17]:

- **High Temperature Tolerance:** cladding material must have a very high melting temperature and resistance to the nuclear core high temperatures in order to keep the fuel and fission products isolated from coolant/moderator and increase the thermal efficiency of the reactor. The reactor core temperatures for Pressurized Water Reactors (PWRs) and Boiling Water Reactors (BWRs) during normal operating conditions are 315°C and 285°C, respectively [16]. However, these temperatures could increase dramatically during accidents, such as a loss of coolant accident (LOCA), and lead to catastrophic consequences.
- **Low Absorption Cross-Section for Thermal Neutrons:** cross-section is a term used to express the probability of an interaction between a thermal neutron and a nucleus. Since the neutron has a neutral charge, it travels in a straight line until it collides with a nucleus. Then, the neutron is transferred, absorbed or scattered. To reduce the number of neutrons lost during the fission process and sustain the chain reaction, cladding material should be transparent to thermal neutrons, i.e. has a low neutron absorption cross section [17, 18]. **Table 1.1** shows the values of neutron absorption cross section for some pure elements in comparison with zirconium, the most widely used cladding material.

Elements	Neutron absorption cross section (Barns)
Be	0.009
C	0.004
Mg	0.063
Si	0.160
Zr	0.185
Al	0.231
Mo	2.480
Cr	3.050
Nb	1.150
Fe	2.550
Ni	4.430
V	5.040
Sn	0.630

**Table 1.1.** Neutron Absorption Cross Section for Pure Elements measured in Barns (Barn =  $10^{-28}$  m<sup>2</sup>) [17].

- **High Corrosion Resistance:** due to the highly corrosive environment of the reactor core, which could get worse in the case of accidents, cladding material must have a high corrosion resistance at elevated temperatures, taking into consideration all possible situations such as high temperature water, steam, and even air.
- **Radiation tolerance:** cladding material must also be resistant to radiation. The intense radiation fluxes produced during the nuclear reactions could generate all possible material defects and change the mechanical properties of the cladding

material. Moreover, radiation can also increase the corrosion and creep rates that result from changing the redistribution of alloying elements, stability of the phases and the kinetics of phase transformations [17, 19].

- **High Thermal Conductivity:** the transfer of the nuclear heat from the edges of fuel pellets to the reactor coolant is remarkably affected by the thermal conductivity of the cladding material. Hence, it's important that the cladding material has a high thermal conductivity to maintain the fuel efficiency.

### **1.5. Accident-Tolerant Fuels (ATF) for LWRs**

Based on an excellent combination of material properties, zirconium alloys were selected for use as nuclear fuel cladding materials since the 1950's [18, 21]. The attractive properties such as low neutron absorption cross-section, high strength, and good corrosion resistance in hot water made zirconium an exceptional cladding material for both conventional Light-Water Reactors (LWRs), including PWRs and BWRs in normal operating conditions [22]. However, the aggressive environment of the nuclear reactor core during off-normal operating conditions makes the cladding material susceptible to many different forms of failure. After several nuclear power plant accidents, including the latest accident in Fukushima Daiichi, the motivation for exploring advanced accident-tolerant fuel (ATF) systems began to increase [23]. Currently, the United States Department of Energy (US DOE) is supporting research activities at multiple national laboratories and universities and within the industries to develop an enhanced ATF system for commercial LWRs [24, 25]. The program was

initiated in 2012, and it is expected to make a breakthrough by the end of 2022 [25]. The goal of this program is to change or modify the current uranium dioxide-zirconium alloy ( $\text{UO}_2 - \text{Zr}$ ) fuel system to tolerate the loss of active cooling for a longer period of time while maintaining or improving its characteristic normal operating performance [23].

The major advantage of developing ATF is to enhance the safety, increase reliability, and lower the operating cost. The focus areas of ATF development include current zirconium-based cladding material, alternative non-zirconium cladding material, and fuel forms with enhanced retention capabilities of fission products [23]. Meanwhile, advanced fuel systems should be backward compatible with current fuel design, safety, cost, and fabrication facilities [24]. **Figure 1.2** depicts the main requirements of the advanced ATF system.

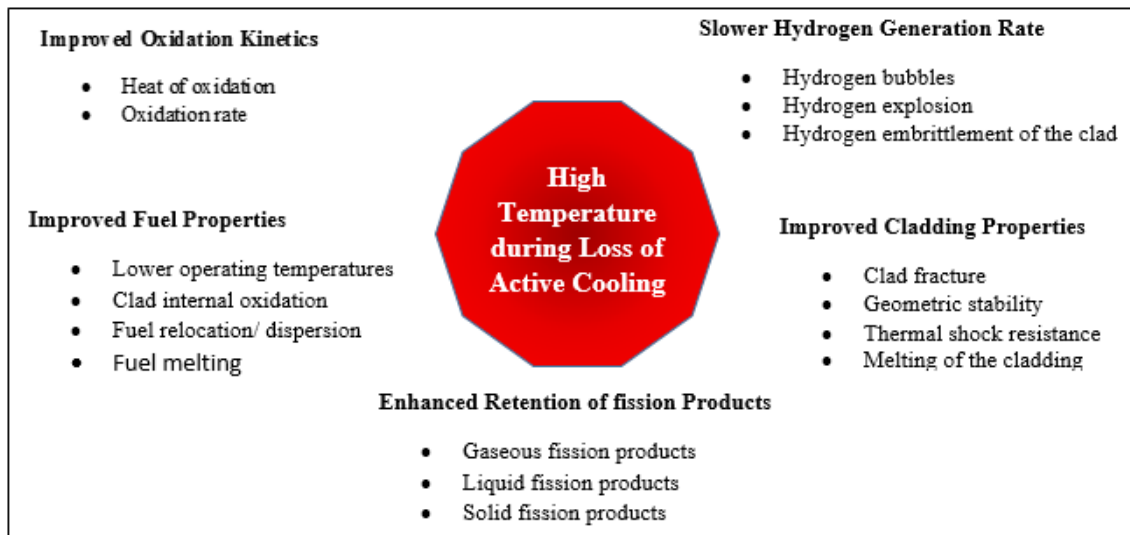


**Figure 1.2.** Major requirements of advanced accident-tolerant fuel system (ATF) [24].

Nuclear-grade zirconium alloys (Zircalloys) are the current fuel cladding materials in almost all water-cooled reactors [26]. To improve the performance of current cladding material to tolerate severe accident scenarios, zirconium alloys have been intensively researched [27, 28]. Therefore, further improvements in Zircalloys are unlikely to result in dramatic changes in their performance during these conditions. Instead, application of highly adherent oxidation-resistance coatings is being considered as an alternative approach to improve Zircalloys performance [23]. However, application of coatings requires a careful selection of material to ensure matching the thermal expansion coefficient of coating with that of Zircaloy. This is to reduce the interfacial stresses that result from heating and cooling and improve the performance of the coated material. Additional endeavors include development of high-density, high thermal conductivity ceramic fuels, and metallic alloys with high corrosion resistance such as iron-chromium-aluminum (FeCrAl) and Molybdenum (Mo) that fulfil some of the ATF concepts as cladding [24].

In this project, the effect of the Laser Shock Peening (LSP) process on the oxidation behavior of Zircaloy-2 (Zry-2) at elevated temperatures is investigated. However, the primary objective of this research project is to examine the oxidation behavior of  $Ti_2AlC$ , as alternative fuel cladding material, in steam at elevated temperatures and compare that to the behavior of Zircaloy-2 (Zry-2) in the same environment.

## 2. LITERATURE REVIEW

This chapter provides an overview of the previous work done to investigate the oxidation mechanisms of the current nuclear fuel cladding materials, Zircalloys, and the proposed alternative cladding material,  $Ti_2AlC$ . Hence, the oxidation related research on these two materials is explored separately to furnish the reader with fundamental information pertaining to the objective of this thesis and pave the way for future research in this area.

### 2.1. Oxidation of Zirconium Alloys (Zircalloys)

Oxidation of zirconium alloys has a great impact on zirconium fuel cladding in most water-cooled nuclear reactors [29, 30, 31]. Since Zircalloys are the primarily used materials for fuel cladding, it is imperative to understand the oxidation mechanisms of these materials not only at normal operating temperatures, but also during failure modes and high temperatures.

#### 2.1.1. Zircalloys

Nuclear-grade zirconium alloys (also called Zircalloys) are the most widely used materials for fuel cladding in almost all water-cooled reactors [26]. Zircalloys contain more than 95% zirconium. To reduce the number of thermal neutrons lost during the fission process, nuclear-grade zirconium is almost entirely separated from hafnium, which has a very high neutron absorption cross-section in comparison with zirconium.

Zircalloys have a hexagonal close-packed (HCP) crystal structure as an alpha phase whereas the beta phase is body centered cubic (BCC), which begins upon heating to 810°C [32]. To improve the oxidation behavior of zircalloys, several changes in the material composition percentages have been investigated in an effort to create a new, more durable alloy. While there are opposing views regarding the similar oxidation rates of pure zirconium and its alloys, there is no significant difference between the oxidation behavior of Zircaloy-2 and Zircaloy-4 [33]. The chemical composition of the two most customarily used alloys, Zircaloy-2 and Zircaloy-4, can be found in **Table 2.1**. The addition of alloying elements such as tin, iron, chromium, and nickel to zirconium is to strengthen the material and offset the effect of impurities, such as nitrogen, on corrosion resistance [34]. Zircaloy-4 has the same chemical specifications as Zircaloy-2 except the maximum range of nickel content is limited to 0.007% and the iron is increased to 0.18 – 0.24%. This change is introduced to reduce the hydrogen pick-up in certain reactor conditions [31, 34]. Zircaloy-2 is mainly used as fuel cladding for BWRs, whereas Zircaloy-4 is more suitable for PWRs because Zircaloy-4 has a lower hydrogen pickup compared to Zircaloy-2. In general, Zircalloys have low thermal neutron absorption cross section, high thermal conductivity, radiation resilience and adequate corrosion resistance in high temperature water [20, 27, 32, 34]. Therefore, Zircalloys have been exceptional materials to serve as fuel cladding and ideal materials at the normal reactor operating temperature (~ 300°C) [34, 35]. However, when the temperature increases beyond the realm of normal operating temperature, during the loss-of-coolant accident, high temperature corrosion reactions take place and result in the reactor failure. The increase

of hydrogen production which results from the oxidation of Zircalloys at elevated temperatures has currently been one of the most studied subjects [27].

	Element	Weight%
<b>Zircaloy-2</b>	Sn	1.2 – 1.7
	Fe	0.07 – 0.20
	Cr	0.05 – 0.15
	Ni	0.03 – 0.08
	Zr	Balance
		+ impurities
<b>Zircaloy-4</b>	Sn	1.2 – 1.7
	Fe	0.18 – 0.24
	Cr	0.07 – 0.13
	Zr	Balance
		+ impurities

**Table 2.1.** Chemical Composition of Zircaloy-2 and Zircaloy-4 [32].

Despite the great precautionary measurements taken to prevent accidents in the nuclear power plant, some accident scenarios could result in devastating consequences. A failure in an emergency core cooling system during LOCA could result in hydrogen explosion, core melt, plant destruction and the release of radioactive materials into the environment [36].

### 2.1.2. Loss of Coolant Accident (LOCA)

Loss-of-coolant accident (LOCA) is considered one of the most dangerous failure modes for nuclear reactors that could easily lead to reactor core damage, if not managed effectively. It is often called a design based accident, but natural phenomenon such as earthquakes could also lead to serious accidents that are out of control. After the Fukushima Daiichi nuclear disaster in March 2011, the LOCA has become the focus of an increased number of researchers around the world in an effort to make the fuel systems safer in the event of a station failure [37, 38]. The most essential part of the reactor that is affected during LOCA is the fuel cladding material, which prevents the direct contact between the nuclear fuel and the coolant inside the reactor vessels and avoid radioactive isotopes from contaminating the system and being released into the environment. This review focuses mainly on the oxidation mechanisms of zircaloy fuel cladding at the onset of LOCA and beyond, which includes oxidation in water, steam, and air.

### 2.1.3. Oxidation of Zircaloy in Water

During normal operating environment, Zircaloy is capable of growing a very thin film of oxide that protects them from further oxidation [32]. This passivating event, which is uniform throughout the metal surface, results from the reaction of zirconium with  $O^{2-}$  ions or  $OH^-$  radicals [39, 40]. The anodic reaction can be expressed as



where  $V^{\circ}_o$  indicates a lattice vacancy in the  $ZrO_2$  layer.

The cathodic reaction is either reduction of water at the oxide/coolant interface:



or as it follows when water contains dissolved oxygen:



However during the long period of its exposure to the volatile water as a fuel cladding, many factors could contribute to the breakdown of this passive film and degradation of the cladding [41]. In general, oxidation of zirconium and its alloys is attributed to the diffusion of oxygen  $O^{2-}$  ions (via anion vacancies) from the external oxidizing medium through the oxide layer and formation of suboxide at the metal/oxide interface [30]. To become electrochemically neutral, an electron current flows from the oxide/metal interface towards the oxide surface while protons flow in the opposite direction [40, 41]. The schematic representation of this reaction can be found in **Figure 2.1**. The oxidation rate in this process is concluded to be governed by the diffusion mechanism through the oxide layer into the metal/oxide interface [30, 32, 40].

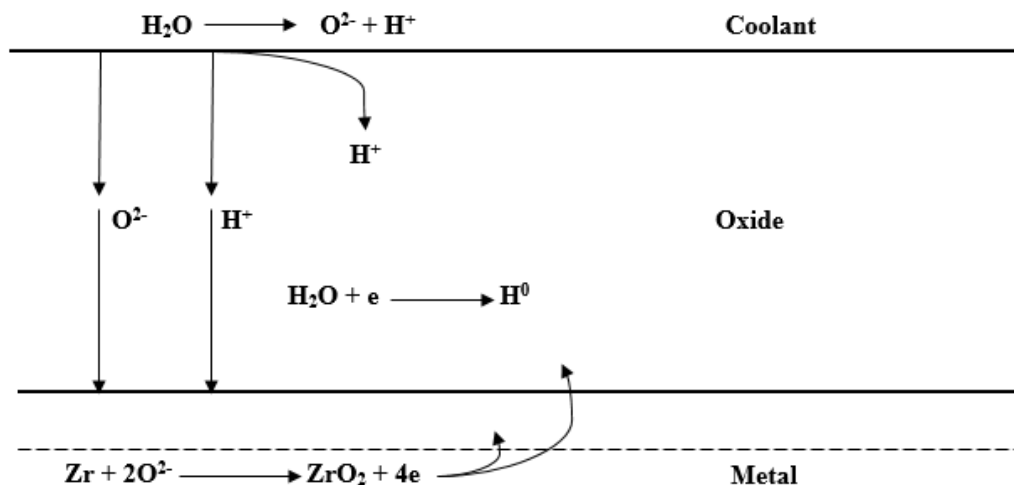


**Figure 2.1.** Schematic representation of the corrosion of the zirconium alloys [42].

The oxidation rate is divided into three phases: pre-transition phase, transition (breakaway), and post transition phase [43, 44]. **Figure 2.2** shows a typical oxidation curve for temperature in the range of 320°C. The oxidation rate is initially very slow because of the limited diffusion through zirconium dioxide film  $\text{ZrO}_2$ , which serves as a poor conductor, and then it becomes cubic or parabolic oxidation rate [45]. According to the Pilling and Bedworth ratio, the growth stress due to the molar volume difference between the metal and oxide was found to be 1.56, which suggests formation of compressive stress in the oxide scale [46]. Moreover, the thermal expansion coefficient of Zircalloys is higher than that of the oxide scale which is also expected to be compressive and added to the growth stress. While the time dependence of oxidation is not confirmed, most researchers agree that it is initially parabolic (weight gain is proportional to  $t^{1/2}$ ) and then it changes to cubic (weight gain is proportional to  $t^{1/3}$ ). After a prolonged

exposure to the corrosive environment, the rate of oxidation changes rapidly and becomes linear (post transition phase). This change occurs due to the “breakaway” behavior, characterized by a breakdown in the passive oxide layer due to the accumulation of compressive stresses that result from the volume expansion or recrystallization of the oxide film [39, 41, 47].

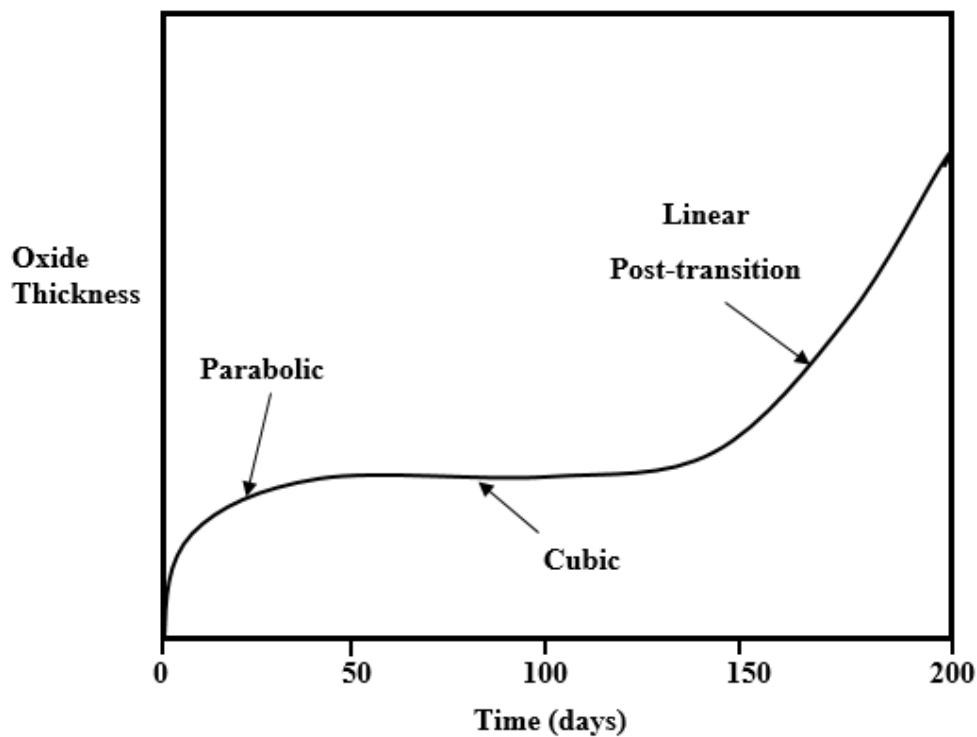


**Figure 2.2.** Typical oxidation curve of zircaloy at 320°C, adopted from Rion et al. [43].

Ni et al. [29] found from the cross-sectional TEM studies of oxides grown on Zircalloys that the oxide porosity increases as the oxidation rate increases and the morphology of the oxide porosity changes progressively. In order to observe a very small area of the oxide/metal interface in pre-transition, post-transition and breakaway oxides,

Fresnel contrast imaging was used. They concluded that the formation of small isolated pores of 1-3 nm initially at the interface which later develop into connected pores in both lateral and vertical directions. These interconnected pores eventually form diffusion paths into the metal/oxide interface and initiate accelerated oxide growth [48].

#### 2.1.4. Oxidation of Zircalloys in Steam

In the range of 600 – 1000°C, the oxidation kinetics is similar regardless of the oxidant (oxygen, steam, or air); it increases with the exposure time [30, 49]. The dense, protective oxide film changes into a porous, cracked, and thick oxide layer. The origin of the pores and cracks in the oxide film could result from several possible mechanisms such as the oxide transformation from tetragonal (t-ZrO<sub>2</sub>) to monoclinic (m-ZrO<sub>2</sub>) form and the oxidation rate correlates with the density of cracks in the oxide layer and the morphology of the oxide grains [36, 47, 50, 51, 52, 53, 54]. Oxide recrystallization process is thought to be the primary cause of generating a network of small pores (10-50 Å radius) which penetrate into the oxide/metal interface and lead to the transition in oxidation kinetics [47, 48, 55]. Gong et al. [47] showed that the morphology and crystal structure of the pre-transition oxides formed on zircaloy-4, oxidized in 400°C/10.3 MPa pure steam, are changed as a function of distance from the oxide/metal interface. **Figure 2.3** illustrates the evolution of zirconium oxide films prior to the transition of oxidation kinetics. The monoclinic columnar grains embedded with small-sized tetragonal equiaxed grains are arranged closely together in the inner oxide, whereas porous monoclinic equiaxed grains with gradually decreasing tetragonal equiaxed grains are in

the outer oxide [47, 56]. When the dense oxide layer becomes porous, the diffusion path of the oxidant decreases in the  $ZrO_2$  layer and the oxidation is no longer controlled by the diffusion of oxygen through the oxide layer [47, 49].

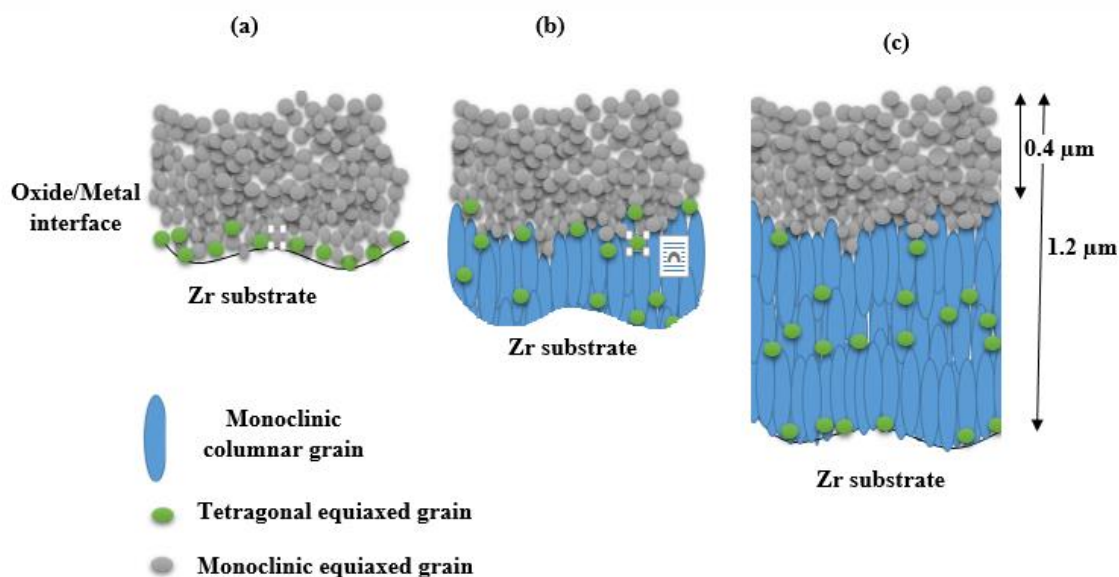


**Figure 2.3.** Schematic illustration of microstructural evolution of zirconium oxide films prior to the transition of oxidation kinetics [56].

Gong et al. [57] claimed that they identified nanoscale pores at grain boundaries of the columnar oxides by SEM. They attributed that to the enrichment of alloying elements at the grain boundaries which causes unequal diffusion of their cations due to their low solid solubility in the  $\alpha$ -Zr matrix and faster diffusion of their cations in  $ZrO_2$  than  $Zr^{4+}$  [32, 57]. During the initial oxidation of Zircalloys, second phase particles (SPPs) remain unoxidized. However, when the oxide reaches a specific thickness, the SPPs start to oxidize and some of the alloying elements of the SPPs may diffuse into the oxide. This

process is expected to change the oxide crystallography and accelerate the oxide breakdown [32]. Baek et al. [58] concluded that the breakaway oxidation becomes faster with increasing the Sn content within zirconium alloys. This is due to the segregation of Sn at the crystalline boundaries in t-ZrO<sub>2</sub> which destabilizes t-ZrO<sub>2</sub> oxide phase and increases its transitioning to the m-ZrO<sub>2</sub> phase [59]. Furthermore, formation of SnO<sub>2</sub> after migration of Sn into the oxide crystallite boundaries in ZrO<sub>2</sub> was observed in high resolution TEM images of the oxide scale [60]. This was also confirmed by Garde et al. [61]; and it was justified that when Sn<sup>3+</sup> ions replaces Zr<sup>4+</sup> in the ZrO<sub>2</sub> lattice, O<sup>2-</sup> vacancy concentration increases and it increases oxygen diffusion through the oxide layer. Conversely, Nb addition retains a relatively more stable phase of the t-ZrO<sub>2</sub> for a prolonged exposure [58].

Zhang et al. [62] used a computation model based on the Wagner's theory and electron theory of solids to show the relationship between the oxidation resistance and grain size of nanocrystalline zirconium at high temperature. Considering conductivity, electronic free path and grain size of the metal, they found that the oxidation/corrosion resistance of nanocrystalline zirconium metal increases significantly with the decrease of grain size.

Platt et al [63] reported that samples with different surface finishes exhibit different oxidation behavior in steam at 400°C. The samples with rougher surfaces initially show enhanced oxidation and continue to gain weight as the oxidation time proceeded. Despite the extensive research conducted in this area since the 1960s, the essential mechanisms of corrosion are not yet completely understood [64]. Throughout

this review of literature and work done on Zircaloy oxidation, it has become obvious that there are a variety of factors that enhances the oxidation of this material in nuclear reactors. The main and most investigated factors are chemical and physical state of the material (including composition, metallurgy and surface condition), coolant chemistry, radiation, pressure and temperature.

Oxidation of Zircaloy fuel cladding by high temperature steam during LOCA is one of the most common phenomenons to rapidly degrade the cladding [27, 65]. If the reactor core is not sufficiently cooled, the decay heat from fission products will continue and increase the overall reactor temperature. The high temperature oxidation in this event also increases the oxygen and hydrogen content in the cladding, reducing its ductility and resistance to rupture [27]. Any increase in temperature above the normal operating temperature plays a significant role on the overall integrity of the fuel cladding. Allen et al. [39] confirmed experimentally that an increase of even 5°C for the typical range of operating temperature (335°C) would accelerate the oxidation kinetics. The rapid increase in temperature during the LOCA accelerates oxidation reactions, which result in the failure of the reactor and release of the radioactive materials.

The primarily high temperature reaction in LOCA is when the zirconium alloys react with steam [66]:



The above reaction is an exothermic reaction in nature, and it produces large amounts of heat and hydrogen when the temperature is close to or above 1200°C [66]. This increase in hydrogen level could result in high explosions, which can damage the core and expose the core components to the atmosphere. Consequently, fission products can release from the fuel matrix, react with steam and hydrogen gas mixture, and escape into the environment through the damaged core containment.

#### **2.1.5. Oxidation of Zircalloys in Air**

Most investigations of inadequate cooling accidents have assumed only one reaction: the reaction between zirconium alloys and steam. However, there are many scenarios where the core components are exposed to air, which increases the oxidation rate and produces 85% higher heat than steam [49, 52, 63, 67]. This occurs due to the low thermal conductivity of air in comparison with steam which results in a poor heat transfer rate [49]. Because of the simultaneous oxidation and nitriding processes, the air oxidation of zircaloy is much more complex than steam oxidation. As a result, a nonprotective oxide (cracked, porous, and nitrated) is formed on the Zircalloys [49, 67]. The oxidation-nitriding process in Zircalloys consists of the following steps:

- Reaction between the Zircaloy cladding and the atmosphere
- Diffusion of oxygen and/or nitrogen through the already formed oxynitride layer to the underneath metal-oxynitride interface.
- Internal reaction between zircaloy and oxygen, and between zircaloy and nitrogen



The mechanism of oxidation kinetics starts with oxygen starvation in the pores (cracks) of the oxide film which makes the oxidation kinetics lower than nitriding kinetics and leads to the formation of ZrN and oxynitride [44, 52]. However, when oxygen partial pressure increases again, the oxidation kinetics becomes higher than the nitriding one because the oxide is thermodynamically more stable than nitride, and the nitride particles are re-oxidized. At this stage of oxidation, nitrogen is released in the oxide or in the metal causing volume increase [52, 67]. Since the molar volume of oxide is greater than that of nitride, the conversion of nitride particles into oxide applies stresses on the metal. This process results in creep and deformation, more surface exposed to air, and eventually kinetics change to the post-breakaway oxidation [65].

The seriousness of the oxidation problem in nuclear reactors and its negative impact on the fuel cladding materials has caused many researchers to study the situation closely and seek the best possible solutions to this issue. As this effect is surface related, one of the solutions to the problem is to cover the surface with a thin film of a protective material in order to keep the advantages of Zircalloys and reinforce its surface chemical resistance. Kratochvílová et al. [68] and Fendrych et al. [55] confirmed that coating cylindrical tubes of Zircaloy-2 nuclear cladding with a 300 nm thick polycrystalline

diamond layer (consisting of crystalline  $sp^3$  and amorphous  $sp^2$  carbon phases) using microwave plasma-enhanced chemical vapor deposition (CVD) apparatus protects Zircaloy-2 against hot steam oxidation. Maier et al (2015) [69] showed that coating the surface of Zircaloy-4 with a thin film of MAX phase  $Ti_2AlC$ , using cold spray deposition process, improves not only its oxidation resistance but also its mechanical properties. During the oxidation tests in ambient air at  $700^\circ C$ , no oxidation was observed on the coated Zircaloy-4 whereas the uncoated Zircaloy-4 developed a 10 micrometer oxide layer. Additionally, simulated LOCA tests that were conducted at  $1005^\circ C$  proved that these coatings can protect the underlying Zircaloy-4. In a separate research study conducted by Baczynski, J. R (2014) [27], it was shown that coating Zircaloy-2 with a thin film (65.4 nm) of titanium, using sputtering technique, exhibited a better oxidation resistance than uncoated Zircaloy-2 in steam at  $700^\circ C$ . Although several coating thicknesses of titanium were considered in this study, only the thicker coating (65.4 nm) showed a promising sign of protection against oxidation.

## 2.2. High Temperature Oxidation of Ti<sub>2</sub>AlC MAX-phase

High temperature oxidation of Ti<sub>2</sub>AlC is one of the foremost topics that is being researched today. Ti<sub>2</sub>AlC is a very promising material for its relatively excellent oxidation resistance at high temperature. This promotes its use as an alternative fuel cladding material that could survive the corrosive nuclear core environment. However, more research is required considering the other aspects of severe nuclear core atmosphere to ascertain the full validity of this material for nuclear use. The work done in this research study is related to the oxidation of Ti<sub>2</sub>AlC in high temperature steam. Therefore, the second part of this literature review focuses on Ti<sub>2</sub>AlC including fundamental knowledge, and high temperature oxidation. To better understand the oxidation behavior of Ti<sub>2</sub>AlC, this section reviews the oxidation behavior from two aspects: Oxidation kinetics and microstructure evolution during high temperature oxidation.

### 2.2.1. Ti<sub>2</sub>AlC MAX-phase

Ti<sub>2</sub>AlC is a member of the MAX-phase family of layered ternary carbide and nitride. The typical formula for this family of MAX-phase is M<sub>n+1</sub>AX<sub>n</sub> (n=1-3), where M is an early transition metal, A is an A-group element, and X is either C or N [70, 71, 72]. The layered ternary Ti<sub>2</sub>AlC ceramic has a hexagonal structure, and it was discovered by Jeitschko et al. in the 1960s [73]. The lattice parameters of Ti<sub>2</sub>AlC are a = 0.304 nm and c = 1.360 nm. **Figure 2.4** shows the crystal structure of Ti<sub>2</sub>AlC with its atomic arrangement in the unit cell. As suggested by the chemical composition, Ti<sub>2</sub>AlC has two layers of Ti and one layer of Al. Al layers are illustrated by underlined letters, and the normal letters

refer to Ti layers. The small size of C atoms make them fit easily into the interstitial sites of Ti atoms, forming octahedral interstitial sites. The chemical bonds between Ti and C atoms are stronger than those between Ti and Al [72]. Due to the charge density distribution, the chemical bonding in  $\text{Ti}_2\text{AlC}$  is anisotropic in nature and can be described as metallic-covalent- ionic [72, 74]. The chains of directional covalent bonding between titanium and carbon (Ti-C-Ti) and layers of the closed packed Al atoms define the properties of  $\text{Ti}_2\text{AlC}$  [74]. As a result, the material combines a unique set of chemical and physical properties, which cannot be found in any metal or ceramic. Similar to metals, it possesses a good electrical and thermal conductivity, superior resistance to thermal shocks, and easy machinability. Similar to ceramics, it has a very high melting point, high modulus and low thermal expansion coefficient. Additionally,  $\text{Ti}_2\text{AlC}$  is one of the most light-weight and oxidation resistant among all the ternary carbides reported to date [71].

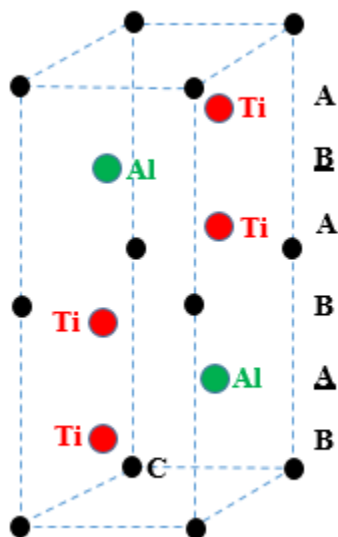


**Figure 2.4.** Crystal structure of  $\text{Ti}_2\text{AlC}$  with its atomic configurations in the unit cell [70]

In spite of the initial great interest in  $\text{Ti}_2\text{AlC}$  after its discovery, the material was left abandoned for a while due to the difficulty in obtaining a fully dense material [75]. Later, Barsoum et al. [76] showed that polycrystalline  $\text{Ti}_2\text{AlC}$ , which is fully dense and readily machinable, can be fabricated by hot pressing at  $1600^\circ\text{C}$  for 4 h. In a more recent study, reactive hot isostatic pressing at  $1300^\circ\text{C}$  for 15 h, in which Ti,  $\text{Al}_4\text{C}_3$  and graphite powders were used, resulted in a dense and predominantly single-phase  $\text{Ti}_2\text{AlC}$  [77]. However, the high reaction temperature ( $1600^\circ\text{C}$  for 4 h) in the first study and long reaction time ( $1300^\circ\text{C}$  for 15 h) in the second one were both considered disadvantages to the use of such an important material for future applications [75]. To overcome these disadvantages, Wang and Zhou [78] used a novel solid-liquid reaction synthesis and simultaneous densification process at a temperature below  $1400^\circ\text{C}$  to fabricate bulk  $\text{Ti}_2\text{AlC}$  using hot pressing. The solid-liquid term used in this process is due to the fact that aluminum melts at  $660^\circ\text{C}$ , which facilitates the reaction between Al and Ti to form intermetallics ( $\text{TiAl}$  and  $\text{Ti}_3\text{Al}$ ) at  $850^\circ\text{C}$ . When the temperature reaches  $\sim 1100^\circ\text{C}$ , TiC forms and reacts with these intermetallics to produce a fully dense, polycrystalline  $\text{Ti}_2\text{AlC}$ . Besides the advantages of low processing temperature and short reaction time,  $\text{Ti}_2\text{AlC}$  fabricated by this method showed an excellent electrical conductivity and high mechanical properties [78]. These properties, in addition to other features such as oxidation resistance, promote the use of  $\text{Ti}_2\text{AlC}$  as a good candidate for high temperature applications [75].

### 2.2.2. Oxidation Kinetics of Ti<sub>2</sub>AlC in Steam

Oxidation kinetics is commonly used to describe the oxidation behavior of MAX-phase. This is the mass gain per unit surface area as a function of time,  $(\Delta W/A)$  vs.  $t$  [71]. According to Wagner's theory, the oxidation kinetics obeys a parabolic rate law if the growth of the oxide scale is diffusion controlled [71]. In this case, the weight gain per unit surface area versus oxidation time is described as follows:

$$\left(\frac{\Delta W}{A}\right)^2 = k_p t \quad (2-1)$$

where,  $(\Delta W/A)$  is the weight gain per unit surface area,  $k_p$  parabolic rate constant, and  $t$  exposure time. However, the oxidation kinetics may deviate from the parabolic and obey a cubic rate law. Hence, the cubic rate constant is calculated from the slope of the fitting line when the cube of weight gain per unit surface area is plotted as a function of time.

The relationship can be described as

$$\left(\frac{\Delta W}{A}\right)^3 = k_c t \quad (2-2)$$

where,  $k_c$  is the cubic rate constant. Moreover,  $(\Delta W/A)$  could also be directly proportional to the exposure time when the oxide scale is no longer protective due to porosities and cracks. In this case the oxidation kinetics can be described as

$$\left(\frac{\Delta W}{A}\right) = k_l t \quad (2-3)$$

where,  $k_l$  is the linear rate constant.

The oxidation kinetics of bulk  $Ti_2AlC$  has been systematically investigated in different environments and at different temperatures. However, there are only several articles published on steam oxidation of  $Ti_2AlC$ . Most recently, Tang et al. [79] investigated the oxidation behavior of  $Ti_2AlC$  in high temperature steam (1400-1600°C) for a time exposure up to 24h.  $Ti_2AlC$  samples used in this study contained 2.39 wt.% free carbon. The oxidation tests were done in a flowing Ar +  $H_2O$  atmosphere (20 l/h Ar and 20 g/h  $H_2O$ ). During oxidation at 1400°C, the oxidation kinetics obeyed a sub-parabolic rate law for 18h before the breakaway oxidation was observed [79]. For the initial stage of oxidation, the oxidation kinetics was described using an equation similar to **Eq. 2.1** with a higher exponential (~2.5). After the breakaway oxidation, a linear rate law was assumed and **Eq 2.3** was used to describe the oxidation kinetics. However, a much faster oxidation kinetic was observed for  $Ti_2AlC$  samples oxidized in steam at 1500°C. The oxidation kinetics at 1500°C maintained a linear rate law for the entire exposure time. Moreover, oxide spallation took place and resulted in weight loss after the exposure for 18h [79]. The high values of correlation coefficients for oxidation data obtained at 1400°C and 1500°C indicate different oxidation behaviors and different growth rate-limiting steps [79]. During oxidation in steam at 1600°C, the oxide scale formed on  $Ti_2AlC$  lost its protective behavior soon after the oxidation started [79]. In other words, the oxide scale formed on the surface of  $Ti_2AlC$  during steam oxidation at 1400°C remained protective after prolonged exposure whereas it lost protection at 1500°C during the initial stage of oxidation [79]. Then, the porosity and cracks generated on the oxide scale provided short diffusion paths for oxygen and other oxidizing gases, resulting in faster oxidation kinetics [79]. Here, it can be concluded that the maximum

high-temperature limit for oxidation resistance of  $\text{Ti}_2\text{AlC}$  in steam is  $1400^\circ\text{C}$ , at which the material can survive for ~18 hours.

Basu et al. [80] studied the oxidation behavior of  $\text{Ti}_2\text{AlC}$  in 100% water vapor for the temperature range ( $1000 - 1300^\circ\text{C}$ ). After a rapid initial weight gain per unit surface area, the oxidation kinetics decreased and obeyed a cubic rate law for 120 hours at all investigated temperatures [80]. Although both parabolic and cubic rate laws were assumed in this study, the cubes of weight gain as a function of time resulted in higher correlation coefficients ( $R^2=0.85 - 0.99$ ) [80]. Smialek J. L. [81] also observed the cubic oxidation of  $\text{Ti}_2\text{AlC}$  at  $1100$ ,  $1200$ , and  $1300^\circ\text{C}$  when  $\text{Ti}_2\text{AlC}$  samples exposed to 10% water vapor at 6 atm and 25 m/s. This indicates that the oxidation kinetics of  $\text{Ti}_2\text{AlC}$  in the investigated temperature range is more complex than parabolic kinetics and suggests diffusion of more than one species as the rate limiting [80]. The results of the fitting using cubic oxidation kinetics (please refer to the reference for more details) clearly represent this behavior. However, this is more obvious when  $(\Delta W/A)^3$  is plotted as a function of oxidation time. The linear relationship between  $(\Delta W/A)^3$  and the exposure time explicitly suggests that the oxidation kinetics follows a cubic rate law at all investigated temperatures. The relatively lower correlation coefficient obtained for oxidation at  $1000^\circ\text{C}$  is attributed to the greater uncertainty in measuring due to the smaller changes in weight at this temperature [80]. The cubic rate constants for  $\text{Ti}_2\text{AlC}$  samples oxidized in air and water vapor at different temperatures are listed in **Table 2.2**. These were obtained using **Eq. 2.2**. The variation in oxidation constants in air and water vapor is trivial at all temperatures, except at  $1000^\circ\text{C}$ . The cubic rate constant obtained

from the oxidation in water vapor at 1000°C is slightly higher than that obtained from oxidation in air [80].

Oxidation Temperature (°C)	Cubic Oxidation Constant (kg <sup>3</sup> /m <sup>6</sup> /s)		Activation Energy (kJ/mol)–this work	
	Air	Steam	Air	Steam
1000	$3.3 \times 10^{-13}$	$5.6 \times 10^{-13}$	279	261
1100	$1.9 \times 10^{-12}$	$2.0 \times 10^{-12}$		
1200	$1.0 \times 10^{-11}$	$1.2 \times 10^{-11}$		
1300	$5.1 \times 10^{-11}$	$6.0 \times 10^{-11}$		

**Table 2.2.** Cubic Oxidation Constants and Activation Energy [80]

The dependence of rate constant on temperature can also be expressed according to an Arrhenius-type equation [80-82] as follows:

$$k = k_o \exp\left(-\frac{Q}{RT}\right) \quad (2-4)$$

where  $k_o$  is a constant,  $R$  the universal gas constant,  $T$  the absolute temperature in Kelvin and  $Q$  the apparent activation energy. Here, it should be noted that  $Q$  is not necessarily the real activation energy excluding the situations where the rate-controlling step is well defined [82]. The nature of the diffusion medium may change with temperature, and consequently changes the oxidation rate and  $Q$  values. Meanwhile, the oxidation rate constant,  $k$ , could be parabolic,  $k_p$  [82] or cubic,  $k_c$  [80]. Therefore,  $Q$  is not a real activation energy. Instead, it is only a temperature coefficient, which is commonly

referred to as the effective activation energy for oxidation [82]. **Eq. 2.4** can also be written as follows:

$$\ln k = \ln k_o - \left(\frac{Q}{R}\right)\left(\frac{1}{T}\right) \quad (2-5)$$

According to **Eq. 2.5**,  $Q$  can be determined from the slopes of the best fitting straight lines when  $\ln k$  is plotted as a function of  $1/T$  [80].

The oxidation kinetics relations are of utmost importance for understanding the oxidation behavior in general. For instance, the oxidation kinetics of  $Ti_2AlC$  investigated in the 1000 - 1300°C for 120 hours is slightly faster in steam than in air [80]. This variation is more obvious in the Arrhenius plot, which can be found in the reference 80. Additionally, the effective activation energy for oxidation in steam is slightly lower than that in air.

The oxidation behavior of  $Ti_2AlC$  at lower temperatures has rarely been studied, especially at temperatures  $< 400^\circ C$ . Lin et al. [83] investigated the influence of water vapor on the oxidation behavior of  $Ti_2AlC$  at 500 – 1200°C in controlled humidity atmospheres. They concluded that water vapor has a strong influence on oxidation of  $Ti_2AlC$  at intermediate temperatures and reported breakaway oxidation at 500 – 600°C. After water vapor was introduced (10%  $H_2O$  + air) at 600°C, a breakaway oxidation occurred after an initial parabolic rate law for 2 hours. Likewise, an oxidation breakaway was observed after 5 hours of oxidation of  $Ti_2AlC$  at 500°C [83]. At higher temperatures, however, the influence of water vapor was found to only slightly accelerate the oxidation

of  $Ti_2AlC$ , and this was attributed to enhanced mass transportation process through the increased oxygen vacancy.

### 2.2.3. Oxidation Kinetics of $Ti_2AlC$ in Air

Basu et al. [80] also studied the oxidation behavior of  $Ti_2AlC$  in air at 1000, 1100, 1200, and 1300°C. They found that the oxidation kinetics obeys a cubic rate law at all investigated temperatures. The corresponding plot of  $(\Delta W/A)^3$  as a function of oxidation time results in nearly straight lines in this study, supporting the cubic rate law. **Eq. 2.2** was used to calculate the kinetics rate constants. The values of kinetics rate constants along with the activation energies for oxidation in air and steam are listed in **Table 2.2** for the sake of comparison.

Wang and Zhou [71] studied the oxidation behavior of  $Ti_2AlC$  in air in the same temperature range (1000 – 1300°C) but for only 20 hours. To determine the oxidation rate constant, they first assumed that the oxidation of  $Ti_2AlC$  obeys a parabolic rate law. Based on the results obtained from the plot of  $(\Delta W/A)^2$  as a function of oxidation time (see the reference paper for this plot), it was obvious that there was a negative deviation from a straight line which suggests that the oxidation of  $Ti_2AlC$  does not obey a parabolic rate law at the investigated temperature range [71].

Alternatively, a linear relationship was obtained when the cube of  $(\Delta W/A)$  was plotted as a function of exposure time. This suggests that the oxidation of  $Ti_2AlC$  obeys a cubic rate law in the temperature range investigated [71]. Here, the oxidation behavior is

quite similar to the near-cubic oxidation of alumina-forming alloys, namely NiCrAl and FeCrAl [71]. The oxide scale on these alloys was found to grow primarily by oxygen grain-boundary transport. Meanwhile, the mass loss instead of mass gain due to the evaporation of carbon at high temperature in  $Ti_2AlC$  should be considered [71].

The values of cubic rate constants obtained from oxidation curves by Wang and Zhou [74] and those obtained by Basu et al. [80] are comparable, suggesting that the oxidation kinetics remains cubic even for an extended period of time [80].

Wang and Zhou [75] also investigated the behavior of  $Ti_2AlC$  at temperatures 500 – 900°C in air for 20 hours. They observed an abnormal oxidation behavior with higher oxidation kinetics at lower temperatures of 500 and 600°C. The weight gain per unit surface area ( $\Delta W/A$ ) for specimen oxidized at 500°C increased faster than that for those oxidized at 700°C, and ( $\Delta W/A$ ) for specimen oxidized at 600°C was significantly greater than that for 700 and 800°C [75]. This anomalous oxidation behavior was attributed to crack-induced oxidation. And, a parabolic rate law was assumed to analyze the weight gain data and determine the rate constants instantaneously at temperatures 700 – 900°C.

#### **2.2.4. Phase Evolution during High Temperature Oxidation of $Ti_2AlC$**

According to available literature,  $Ti_2AlC$  has an excellent high-temperature oxidation resistance in steam as well as in air for up to approximately 1400°C. Recently, Tang et al. [79] studied the oxidation behavior of  $Ti_2AlC$  in steam at 1400-1600°C. Although the oxide scale remains protective at 1400°C for prolonged exposure time, it loses the protection after 18h and provides no protection at 1500°C and 1600°C [79].

After high temperature oxidation of  $\text{Ti}_2\text{AlC}$  in steam at  $1400^\circ\text{C}$  and  $1500^\circ\text{C}$ , a thin oxide scale consisting of  $\alpha\text{-Al}_2\text{O}_3$  and  $\text{Al}_2\text{TiO}_5$  is observed. Here, the XRD detection of  $\text{Al}_2\text{TiO}_5$  rather than  $\text{TiO}_2$  phase is attributed to the reaction between  $\text{TiO}_2$  and  $\text{Al}_2\text{O}_3$  to form  $\text{Al}_2\text{TiO}_5$  [79]. Similarly, Cui et al. [84] reported initiation of cracks in the oxide scale formed in air at  $1400^\circ\text{C}$  after prolonged oxidation. But, all three phases ( $\text{TiO}_2$ ,  $\text{Al}_2\text{O}_3$ , and  $\text{Al}_2\text{TiO}_2$ ) were detectable in the oxide scale formed in air at  $1400^\circ\text{C}$  [84].

During the high temperature oxidation of  $\text{Ti}_2\text{AlC}$  in both air and steam up to  $1300^\circ\text{C}$ , the oxidized surface only consists of  $\text{TiO}_2$  (rutile) and  $\alpha\text{-Al}_2\text{O}_3$  [71, 80, 83, 84, 85, 86]. Peaks of  $\text{Ti}_2\text{AlC}$  in the XRD spectrum on the oxidized surface suggest a very thin oxide scale. Unlike the oxidation at relatively low temperatures ( $500$  and  $600^\circ\text{C}$ ), no anatase- $\text{TiO}_2$  is observed for temperatures  $1000 - 1300^\circ\text{C}$  [71, 75, 80, 83, 84, 85, 87]. In both air and steam, rutile- $\text{TiO}_2$  forms on the surface of the oxide scale after high temperature oxidation of  $\text{Ti}_2\text{AlC}$  [71, 85]. Although both oxides ( $\text{TiO}_2$  and  $\text{Al}_2\text{O}_3$ ) are detectable in the XRD spectra of the surface oxidized in air,  $\text{TiO}_2$  disappears after oxidation in steam at  $1300^\circ\text{C}$  for 120 hours [80]. Moreover, a nearly constant peak of  $\text{TiO}_2$  is detected for samples oxidized in air from  $900$  to  $1400^\circ\text{C}$  [84].

### **2.2.5. Microstructural Evolution during High Temperature Oxidation of $\text{Ti}_2\text{AlC}$**

To fully understand the microstructural evolution of the oxide scale formed on  $\text{Ti}_2\text{AlC}$ , both surface and cross-sectional views of the scale need to be investigated [88]. The SEM images of the oxidized surfaces of  $\text{Ti}_2\text{AlC}$  samples at  $1000$ ,  $1100$ ,  $1200$ , and  $1300^\circ\text{C}$  showed a continuous  $\text{Al}_2\text{O}_3$  scale with a thin layer of  $\text{TiO}_2$  on the top surface

[80].  $\text{TiO}_2$  appeared in a form of elongated grains while  $\text{Al}_2\text{O}_3$  had smaller grains underneath. The larger size of  $\text{TiO}_2$  grains (shown in SEM images in the reference paper) is a good indication that  $\text{TiO}_2$  forms and grows much faster than  $\text{Al}_2\text{O}_3$  at the beginning of oxidation [80, 85]. The isolated outward growth of  $\text{TiO}_2$  grains also suggests the outward diffusion of Ti through the grain boundaries of  $\text{Al}_2\text{O}_3$  [71, 84, 88]. A palpable variation in surface morphology can be seen between  $\text{Ti}_2\text{AlC}$  oxidized in air and steam at  $1000^\circ\text{C}$  for 120 hours (shown in SEM images in the reference paper) [80]. This suggests that the oxidation in air results in smaller and discontinuously distributed  $\text{TiO}_2$  crystals while a more evenly surface covered  $\text{TiO}_2$  layer with larger grains forms during oxidation in steam. This could decipher the slight variation in oxidation kinetics for the two atmospheres [80]. However, similar surface morphologies are observed after isothermal oxidation in air and steam at  $1100$  and  $1200^\circ\text{C}$ , except for a few larger  $\text{TiO}_2$  crystals that are present in  $\text{Ti}_2\text{AlC}$  oxidized in steam. Finally, these  $\text{TiO}_2$  crystals become fewer and smaller after steam oxidation at  $1300^\circ\text{C}$  which strongly confirms the likelihood of  $\text{TiO}_2$  volatilization at higher temperatures in steam [80].

Regardless of the oxidation environment, oxygen vacancy diffusion through  $\text{Al}_2\text{O}_3$  is the rate limiting at high temperatures and for long times [80]. When the temperature is greater than  $1200^\circ\text{C}$ ,  $\text{TiO}_2$  layer becomes volatile after reacting with water vapor and forming gaseous  $\text{TiO}(\text{OH})_2$ . However,  $\text{Al}_2\text{O}_3$  layer remains stable and provides an excellent protection from further oxidation [80, 89].

At  $1400^\circ\text{C}$ , a discontinuous  $\text{Al}_2\text{TiO}_5$  scale forms during isothermal oxidation of  $\text{Ti}_2\text{AlC}$  in both air and steam [79, 80, 85]. After oxidation at  $1400^\circ\text{C}$  for 1h, a few islands

that consist of elongated, Ti-rich grains form on the surface [79]. These Ti-rich islands, which contain cracks and microcracks, are identified by XRD as  $\text{Al}_2\text{TiO}_5$  [79]. The rest of the oxide scale consists of a coarse appearance  $\text{Al}_2\text{O}_3$  with small and random grains [79]. This was also reported by Cui et al. [84] for oxidation of  $\text{Ti}_2\text{AlC}$  in air at  $1400^\circ\text{C}$  which will be discussed later in this section. Similar Ti-rich islands, but smaller in size formed on the surface of  $\text{Ti}_2\text{AlC}$  after oxidation in steam for 1h at  $1500^\circ\text{C}$ . As the oxidation time is increased, the Ti-rich islands decrease [79]. After oxidation at  $1400^\circ\text{C}$  for 12h and as indicated by EDS line-scanning profiles, the oxide scale formed consists of a very thin, discontinuous, and Ti-rich outer layer [79]. This is attributed to generation of gaseous Ti-containing species, which decreases Ti content on the surface. After oxidation in steam at  $1500^\circ\text{C}$  for 12h, the oxide scale formed on the surface has a similar structure but very porous [79].

The oxide scale formed after 1h of oxidation at  $1400^\circ\text{C}$  was adherent and free from cracks, but the one formed at  $1500^\circ\text{C}$  was porous and contained microcracks [79]. These results are well consistent with results obtained from oxidation kinetics discussed in the previous section.

Cui et al. [84] studied the oxidation of  $\text{Ti}_2\text{AlC}$  (containing 4 vol.% impurities) at  $1400^\circ\text{C}$  in a flowing air. After oxidation for 1 hour,  $\text{Al}_2\text{TiO}_5$  is also seen in the oxide scale along with  $\text{TiO}_2$  and a cracked inner layer of  $\alpha\text{-Al}_2\text{O}_3$ . The complex oxide scale, shown in **Figure 2.5**, forms by reaction between  $\text{TiO}_2$  and  $\text{Al}_2\text{O}_3$  according to the following chemical reaction [71, 84]:



The presence of cracks in the commonly protective  $\text{Al}_2\text{O}_3$  layer is attributed to the large difference in the thermal expansion coefficients of  $\text{TiO}_2$  -  $\text{Al}_2\text{TiO}_5$  and the volume changes by reactions, which resulted in cracks in  $\text{TiO}_2$  and propagated into the  $\text{Al}_2\text{O}_3$  [84].

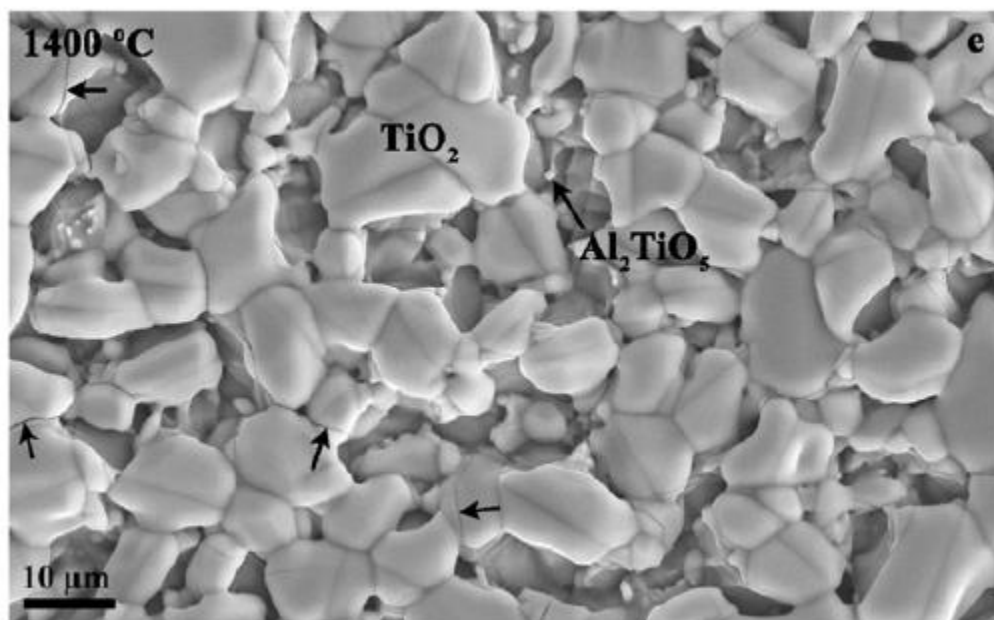


**Figure 2.5.** SEM images of surface morphology of  $\text{Ti}_2\text{AlC}$  oxidized at  $1400^\circ\text{C}$  [84].

The information obtained from SEM images and EDS of cross-sectional views is mostly consistent with XRD [84]. For instance, **Figure 2.6** (a) is an SEM image of cross-sectional view of  $\text{Ti}_2\text{AlC}$  oxidized at  $1000^\circ\text{C}$  in the flowing air, and **Figure 2.6** b and c are the corresponding EDS line-scanning profiles. It can be seen that the scale formed on the surface after oxidation at  $1000^\circ\text{C}$  is very thin ( $\sim 1\mu\text{m}$ ). Additionally, thick bumps, ranging from  $1 - 4\mu\text{m}$ , are apparent in the scale and several microns apart [84]. To investigate the microstructure of the thin oxide scale and thick bumps, EDS line-scans

were made along the two regions separately [84]. The black arrow indicates the line-scan across the thin oxide scale while the gray arrow indicates the line-scan across the thick bump [84]. According to the results obtained from the EDS line-scans (**Figure 2.6b**), the signals of Al and O concentrations are detected throughout the scale, which implies formation of  $\alpha$ -Al<sub>2</sub>O<sub>3</sub> [84]. The concentration of Ti decreases in the direction away from bulk Ti<sub>2</sub>AlC towards the surface, where a small peak is present. This indicates formation of TiO<sub>2</sub> on the top surface. In other words, both TiO<sub>2</sub> and  $\alpha$ -Al<sub>2</sub>O<sub>3</sub> are present in the scale with more TiO<sub>2</sub> near the oxide scale surface. However, different features are acquired from the gray arrow (**Figure 2.6c**), which was made across the thick bump. Peak of Al concentration is present at the inner layer while the peak of Ti is present at the outer layer, suggesting that an outer layer of TiO<sub>2</sub> and an inner layer of  $\alpha$ -Al<sub>2</sub>O<sub>3</sub> are formed on the thick bumps. The features present on the thick bumps are very similar to those on the oxide scale formed at 1200°C, which implies that the oxidation of Ti<sub>2</sub>AlC in thick bumps is more rapid than that in thin layers [88]. These thick bumps are associated with the defects or cracks induced by polishing on the surface, which reduced the activation energy of oxidation [84].

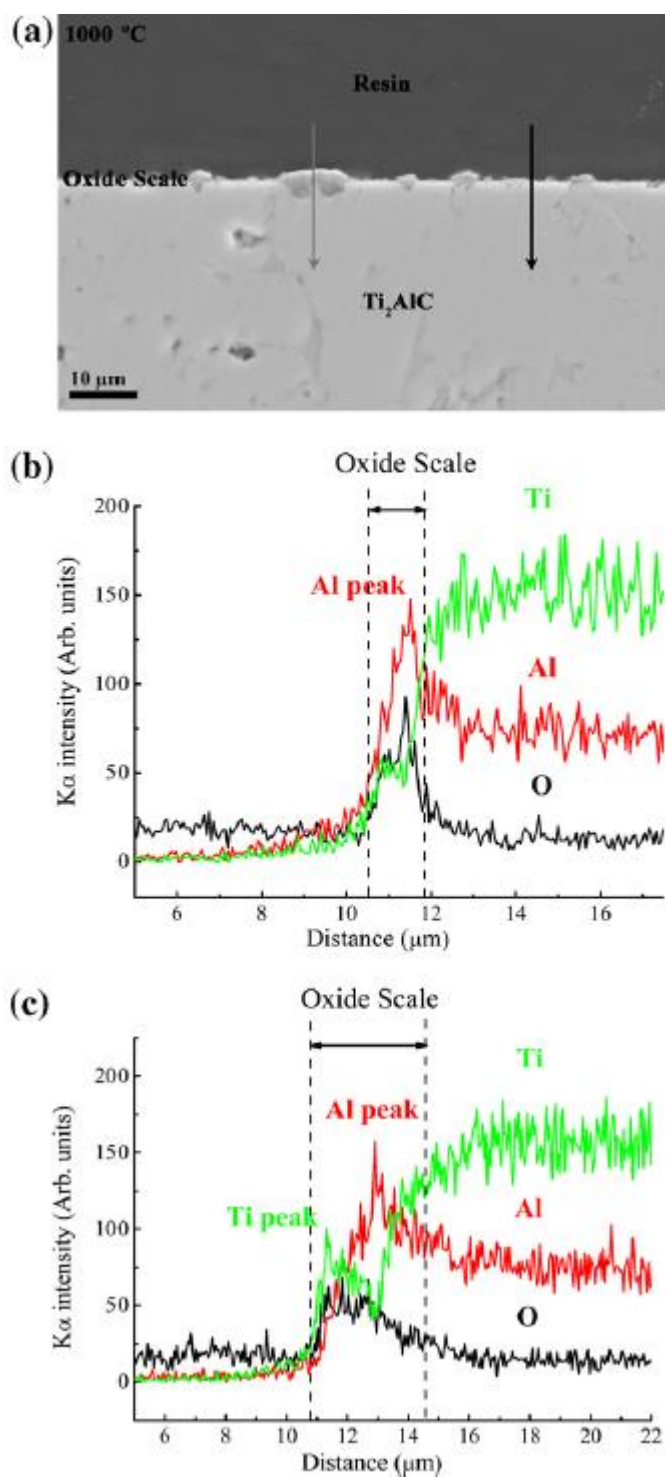


**Figure 2.6.** (a) SEM cross-sectional view of  $\text{Ti}_2\text{AlC}$  oxidized in air at  $1000^\circ\text{C}$ , (b) EDS line-scanning profiles along the black arrow in (a), and (c) EDS line-scanning profiles along the gray arrow in (a) [84].

The anomalous oxidation behavior of  $\text{Ti}_2\text{AlC}$  at intermediate temperatures is also confirmed by SEM. The SEM images of the surface and cross-sectional views of  $\text{Ti}_2\text{AlC}$  after oxidation in 10%  $\text{H}_2\text{O}$  + air at  $600^\circ\text{C}$  for 10 hours indicates initiation of cracks on both the surface and within the oxide scale [83]. Small cracks were also reported by Wang and Zhou for  $\text{Ti}_2\text{AlC}$  samples oxidized in air at  $500$  and  $600^\circ\text{C}$  for 20 hours [75]. They associated these cracks with anatase- $\text{TiO}_2$  for being the major oxidation product after oxidation at  $500$  and  $600^\circ\text{C}$ . They proposed that the oxidation of  $\text{Ti}_2\text{AlC}$  into anatase- $\text{TiO}_2$  at these temperatures causes volume expansion and generates stresses, which lead to the initiation of the cracks and poor protective ability of the scale. The density of anatase- $\text{TiO}_2$  is  $3.893 \text{ g cm}^{-3}$  while the density of rutile- $\text{TiO}_2$  is  $4.25 \text{ g cm}^{-3}$  [83]. Thus, the transformation of the scale from anatase- $\text{TiO}_2$  to rutile- $\text{TiO}_2$ , which could be promoted by water vapor, will result in an increase in the density of  $\text{TiO}_2$  and lead to cracks in the oxide scales [83].

Alternatively, the influence of water vapor on  $\text{Ti}_2\text{AlC}$  during oxidation at  $600^\circ\text{C}$  in wet atmospheres is associated with poor crystallinity of the oxide scale, assuming water vapor hinders the crystallization of the oxide scale [83].

#### **2.2.6. High Temperature Oxidation Mechanism of $\text{Ti}_2\text{AlC}$**

$\text{Ti}_2\text{AlC}$  is the most oxidation resistant MAX-phase; it forms a protective oxide layer of  $\text{Al}_2\text{O}_3$  that can maintain stability, crack-free, and spallation-free during thermal cycling up to  $1350^\circ\text{C}$  for 8,000 cycles [90]. The earliest oxidation study conducted by Barsoum [91] showed that the oxidation of  $\text{Ti}_2\text{AlC}$  is generally caused by the inward

diffusion of  $O^{2-}$  and the outward diffusion of  $Al^{3+}$  and  $Ti^{4+}$  ions through the surface oxide scale. Meanwhile, the compressive residual stress generated in alumina scale formed during the oxidation of  $Ti_2AlC$  at 1000, 1200 and 1400°C are insignificant for both isothermal and cyclic oxidation [85]. The reason for trivial residual stress produced at high temperature oxidation is the similar thermal expansion coefficients of  $Ti_2AlC$  and alumina. This promotes the stability and good adherence of the scale to the substrate, increasing oxidation/spallation resistance.

According to the data obtained from the oxidation kinetics, phase characterization and microstructural evolution, the high temperature oxidation resistance of  $Ti_2AlC$  is associated with the formation of a protective  $Al_2O_3$  layer. During high temperature oxidation of  $Ti_2AlC$  in air, both  $TiO_2$  and  $Al_2O_3$  are formed on the surface. However, the growth of these layers is different and dependent on the oxidation temperature. At the early stage of oxidation, both  $TiO_2$  and  $Al_2O_3$  nucleate and grow simultaneously on  $Ti_2AlC$  substrate [80]. Later, when the temperature is relatively low,  $TiO_2$  grows faster due to its higher formation kinetics [80]. As the oxide scale becomes more stable,  $Al_2O_3$  starts to grow faster because  $Al_2O_3$  needs much lower oxygen partial pressure than  $TiO_2$  to grow. After a uniform layer of  $Al_2O_3$  scale is formed at the substrate/oxide interface, the formation of  $TiO_2$  is stopped due to the low diffusivity of Ti through  $Al_2O_3$  [80]. Here, the diffusion of Al from  $Ti_2AlC$  to form  $Al_2O_3$  becomes the rate limiting. Therefore, only small islands of  $TiO_2$  are observed on the surface as the temperature increases [80].

During high temperature oxidation of  $Ti_2AlC$  in steam, a similar mechanism is proposed since the formation of a protective  $Al_2O_3$  layer remains governed by oxygen vacancies and the inward diffusion of oxygen [80]. However, the hydrogen generated during the reactions between  $Ti_2AlC$  and water vapor could also play a role in its oxidation. The presence of hydrogen increases the concentration of oxygen vacancies, which in turn enhances the diffusion of oxygen and thus accelerates the oxidation of material [83]. Angle et al. [92] also reported that water vapor enhances the diffusion of oxygen in polycrystalline  $Al_2O_3$  during high temperature oxidation. The faster diffusion of oxygen is attributed to the formation of hydroxyl  $(OH)^-$  ion, which is much smaller than  $O^{2-}$  ion. In other words, the oxygen ions embedded with the protons to form hydroxyl ions are much smaller and can diffuse faster due to their lower charge and more flexible shapes [92]. Although the  $(OH)^-$  ions diffuse faster than  $O^{2-}$  ions through the bulk material, grain boundaries are more accommodating, so  $(OH)^-$  ions will less likely diffuse into the bulk through the lattice [92].

### 3. EXPERIMENTAL PROCEDURES

This Chapter briefly introduces the essential sample processing and characterization techniques used throughout this research and the specific purpose of utilizing each technique. The experimental set up and sample preparation for oxidation studies are also pointed out to allow the reader to understand the approach used in this project and use the results as a future reference for similar studies.

#### 3.1. Samples Processing Techniques

The two main components of this section include Laser Shock Penning (LSP) process and the oxidation tube furnace, which was modified to include the use of steam in order to generate a high temperature steam atmosphere.

##### 3.1.1. Laser Shock Penning (LSP)

Laser shock processing, commonly known as LSP, is among the most advanced surface modification processes that are used to improve the mechanical and metallurgical properties of metallic surfaces. It is widely recognized as an effective technique for extending fatigue life, and improving wear and corrosion resistance without introducing excessive surface and microstructural damage [93, 94, 95]. **Figure 3.1** illustrates a schematic representation of the principle of LSP. In this process, high-energy laser pulses are used to irradiate a material surface. When the laser beam is directed onto the material surface through the transparent overlay, it vaporizes a thin surface layer after

striking the material [96]. Plasma is formed due to the high thermal energy produced by laser beam, and it expands and generates shock waves by continuously absorbing the laser energy. Due to the pressure exerted in this process (100 MPa to several GPa), significant compressive residual stresses are induced in the bulk material as a result of plastic deformation. Compressive residual stresses can take place in a depth of more than 1 mm from the surface [97].

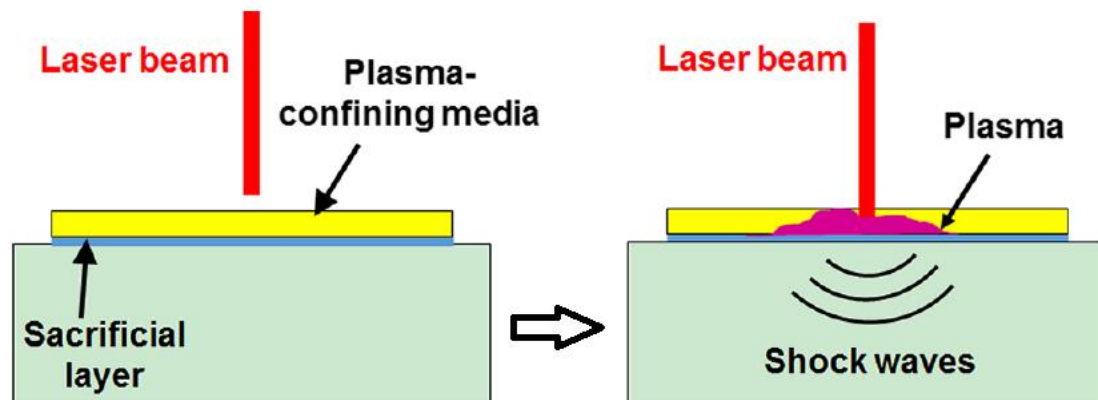


**Figure 3.1.** Schematic representation of the principle of laser shock processing [98].

To protect the working material from melting and ablation by laser heating, a sacrificial coating (absorbent coating) is used on the top to maintain room temperature during the processing [98]. There are essentially two types of sacrificial coatings: metallic coating and organic coating. Metallic coating consists of a metal with a high melting point and good thermal conductivity such as Al, Zn, or Cu while organic coating has a high thermal absorption, and it provides a good surface finish. The transparent overlay, shown in the **Figure 3.1**, could be water, air, or another confining medium to

maintain a high concentration of plasma on the material surface and ensure enough shock waves propagate into the material [96]. Working parameters in this process include laser energy, spot size, duration time, overlap rate, wavelength of the laser beam, and beam profile. These parameters have a significant impact on the LSP process, and it is important that they are adjusted in accordance with the material used in the process. Additionally, both transparent and absorbent layers can play a major role in LSP.

The purpose of using the LSP technique in this research project is to depress the micro-cracking of the oxide scale by inducing compressive residual stresses. LSP is used to form defects by plastic deformation and generate refined and more homogenous grains. Since the high temperature oxidation resistance is mostly affected by the top surface microstructure, the LSP could generate good diffusion paths to the surface and promote the formation of a protective oxide layer during the initial stage of oxidation.

### **3.1.2. Tube Furnace with Steam Capability**

To study the oxidation behavior in steam at different temperatures, a horizontal tube furnace was built to include a steam capability. The complete testing system consisted of a steam generator to push pure steam into the tube furnace, and a steam condenser on the other end to calculate the steam flow rate by measuring the amount of condensed water. The steam flow rate was controlled by the water temperature. A schematic representation diagram of the experimental set up is shown in **Figure 3.2**.

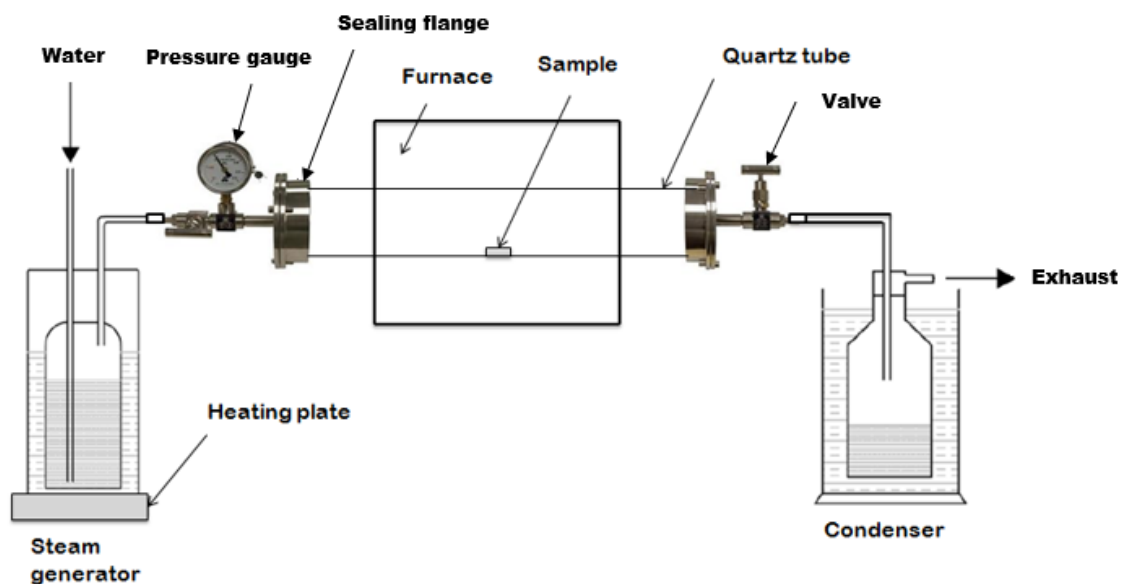


**Figure 3.2.** Schematic diagram of the experimental set up for high temperature steam oxidation study.

The maximum working temperature of the furnace is  $1200^{\circ}\text{C}$  with a heating zone of 8-inch long and temperature accuracy of  $\pm 1^{\circ}\text{C}$ . The heating and cooling rates are  $20^{\circ}\text{C}/\text{min}$  and  $10^{\circ}\text{C}/\text{min}$ , respectively. The diameter of the quartz tube used is 2 inches, and the furnace is equipped with a built-in precision temperature controller that can provide up to 30 segments of heating and cooling steps with great accuracy.

### 3.2. Oxidation Studies

Oxidation behaviors of the current nuclear cladding material (Zry-2), and the proposed alternative cladding material ( $Ti_2AlC$ ) were investigated at 600, 800, and 1000°C in the flowing steam. Additionally, the oxidation behavior of LSP-treated Zry-2 was investigated in air at 600°C. For this study, an as-received Zry-2 sample was LSP treated before the oxidation process, and a different one was treated after it was oxidized but before the breakaway oxidation. The purpose of LSP treatment was to study the effect of LSP on the oxidation behavior of Zry-2. After the oxidation tests, the oxidation kinetics was studied, and the microstructures of the oxide scales from both surface and cross-sectional areas were analyzed by the means of SEM and EDS at room temperature.

#### 3.2.1. Zicaloy-2 (Zry-2)

The Zry-2 samples were supplied by ATI Specialty Alloys & Components. The chemical composition of Zry-2 can be found in **Table 2.1**.

Initially, two as-received Zry-2 samples were oxidized in air simultaneously to get the most reliable calculations. The samples were cut from the bulk material into approximately  $13 \times 6 \times 3$  mm using Electrical Discharge Machining (EDM) and ground carefully up to 1200 grit using SiC. Next, the samples were polished with 3 and 1 micron diamond paste, and cleaned ultrasonically in acetone. Then the samples were put into an open hearth furnace to investigate the actual oxidation behavior in air at 600°C for different periods of time. The weight gain per unit surface area was recorded periodically

for each sample and plotted as a function of time to determine the region of breakaway oxidation.

The purpose of this experiment was to find the effect of the LSP on the oxidation behavior of Zry-2. After the approximate breakaway time was identified, three more samples were prepared using the same steps as mentioned above, and one of the samples was LSP treated four times at pulse energy of 850 mJ prior to the oxidation test. Then, all three samples were put into the furnace and heated at 600°C for a period of time just before the time when the breakaway oxidation had occurred according to the two initially examined samples. At this point, the samples were slowly cooled down in air and another sample was LSP treated four times using a lower LSP energy (400 mj), to avoid damaging the oxide scale formed on the sample's surface. Then, the heating process was resumed for all three samples until the oxide breakaway time had slightly elapsed.

To investigate the oxidation behavior of Zr-2 in the flowing steam at 600, 800, and 1000°C, the same sample size and preparation steps as for air oxidation were used. However, steam experiments were conducted in the tube furnace with steam capability. The specimens were heated in the flowing steam at temperatures 600, 800, and 1000 °C. The heating process from the room temperature to the desired temperature was performed at a rate of 20°C/min, and the samples were naturally cooled down to the room temperature at approximately 10°C/min

For all oxidation studies, the surface and cross-sectional microstructures of the oxide scale were investigated by Scanning Electron Microscopy (SEM) and Energy Dispersive X-ray Spectroscopy (EDS). Prior to SEM examination, a thin layer of gold

was sputtered on the surface of oxidized samples to prevent charge accumulation on the surface.

### 3.2.2. Ti<sub>2</sub>AlC

The Ti<sub>2</sub>AlC samples were supplied by Prof. Yanchun Zhou (Shenyang National Laboratory for Materials Science, Chinese Academy of Sciences). The material was prepared by using a uniaxial hot-pressing process under an Ar atmosphere according to the following procedure: mixed powders of Ti, Al and graphite were milled and heated to 1400 °C for 1h under a pressure of 30MPa.

The phase composition of as-received samples was analyzed by using X-ray diffraction (XRD). The Ti<sub>2</sub>AlC ceramic samples were seen to be mainly single phase. The density of the samples was measured using the Archimedes method, and was found to be 4.10 g/cm<sup>3</sup> (99.8% theoretical).

Specimens of approximately 12 × 7 × 6 mm<sup>3</sup> were cut from the bulk material using Electrical Discharge Machining (EDM) and the specimen surface was ground carefully up to Grit No. 1200 of SiC paper. Then all the specimens were polished with 3 and 1 micron diamond paste and cleaned ultrasonically in acetone.

The specimens were heated in the flowing steam at temperatures 600, 800, and 1000 °C. The heating process from the room temperature to the desired temperature was performed at a rate of 20 °C/min, and the samples were naturally cooled down to the room temperature at approximately 10 °C/min. The heating and cooling times were found to have a negligible influence on the oxidation behavior; this was confirmed by extending

oxidation of a single sample for 8 hours and comparing it with the other samples, which were exposed to a cyclic oxidation process. This is most likely due to the near-identical thermal expansion coefficients of  $Ti_2AlC$  and the oxidation products such as  $Al_2O_3$ . The steam was maintained at an average flow rate of 50 mg/s and 100 mg/s for two different tests to study the influence of flow rate on oxidation behavior. Then, specimens were left inside the furnace in the flowing steam until they were naturally cooled down to the room temperature. The weight of each specimen was measured before and after the oxidation test by means of an electronic balance, and the weight gain per unit surface area was calculated. Mass change was periodically recorded and plotted as a function of time throughout the experiment time.

At the end of the oxidation process, the surface and cross-section microstructure of each specimen was investigated by the means of SEM equipped with Electron Dispersive Spectroscopy (EDS) and Focused Ion Beam (FIB) systems. To study the cross-section microstructure, specimens were either embedded in resin, ground up to 1200 grid, polished down to 1  $\mu m$ , and degreased with acetone; or subjected to an ion beam in several steps in order to get a very well-polished cross section. Prior to SEM examination, a thin layer of gold was sputtered on the surface of oxidized samples to prevent the charge accumulation on the surface.

### **3.3. Characterization Methods**

The following are the most commonly used characterization instruments to study the surface and cross-sectional views of the oxide scale:

### 3.3.1. Scanning Electron Microscopy (SEM)

The SEM is one of the most powerful characterization techniques that are used to examine and analyze the microstructure of solids. It can produce very high resolution images of a specimen surface and reveal details as small as 1 nm on the surface. In SEM, a finely-focused beam of high-energy electrons is used to irradiate the area to be examined or microvolume to be analyzed.

An SEM instrument, which requires a good vacuum level, is comprised of several key components including electron source, lenses, scanning coil, sample chamber, and detectors. The electron source is usually a tungsten filament, LaB<sub>6</sub>, or Field Emission Gun (FEG). Electrons are produced by thermionic heating and accelerated by voltages between 1-40 kV. As the electrons move from the source down the column, the electron beam is focused through a series of electromagnetic lenses until its contact with the surface. The finely-focused beam is deflected in the X and Y directions by scanning coils. As a result, the sample surface is scanned in a raster pattern. Sample chamber contains a variety of devices such as optical cameras, translation stage, tilt and rotation ...etc. that assist in imaging the sample. And, the detectors are used to collect the various electrons that eject from the sample [99]. **Figure 3.3** is a schematic representation of electron beam interaction.

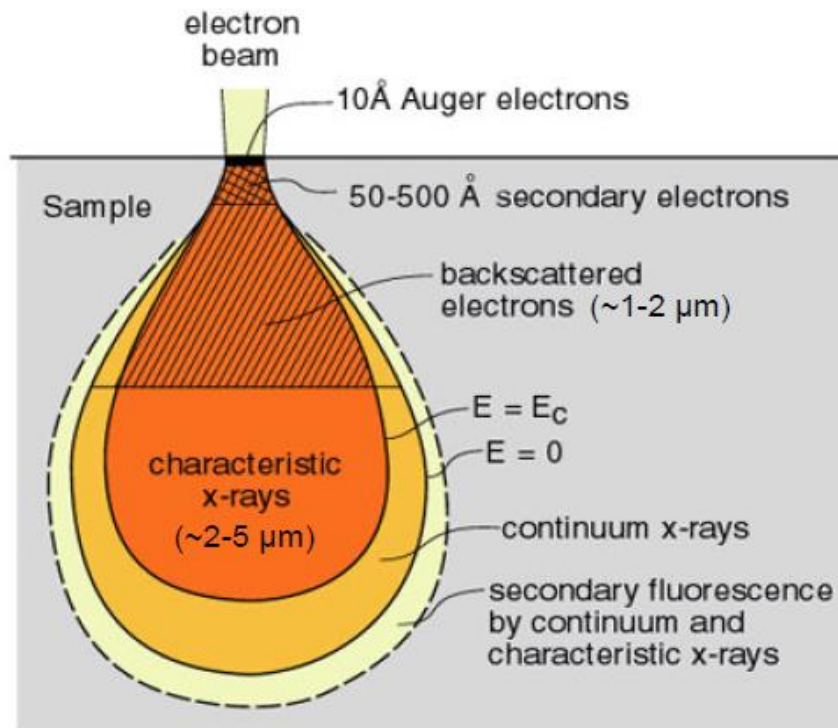


**Figure 3.3.** Schematic representation of electron beam interactions, including the relative depths from which various signals can escape the surface [100].

There are typically two types of electrons used for imaging in the SEM: secondary electrons (SE) and backscattered electrons (BSE). Due to their low energies (typically 20 eV), secondary electrons are ejected from the outer most region of the sample at a volume near the beam impact area during the scanning process. Consequently, they contain very useful information about the surface topography. On the other hand, backscattered electrons have higher energies and are elastically scattered by the atoms of the sample. This type of electron is highly sensitive to the atomic number of the sample (atoms with higher atomic numbers backscatter more efficiently) and can provide valuable compositional information about the sample [99].

In typical SEM imaging, the sample must be electrically conductive to inhibit charging and enable or improve imaging. Meanwhile, non-conductive samples can be coated with a thin layer of a conductive material such as gold or graphite that reduces or eliminates the accumulation of electrical charges when scanning by a high-energy electron beam. Although both materials used in this research (Zry-2 and Ti<sub>2</sub>AlC) were conductive, the oxide layers formed on the surface during the oxidation process were not sufficiently conductive and required surface coating. Therefore, all samples were coated with a thin layer of gold using a sputter coating machine prior to any SEM imaging or EDS chemical analysis.

In this research, two different SEM instruments were used alternatively according to their availability: FEI Nova NanoSEM 450 (**Figure 3.4 a**) and FEI Helios NanoLab 660 (**Figure 3.4 b**). Both of the instruments are coupled with EDS systems for chemical analysis, and FEI Helios NanoLab 660 is also equipped with a Focused Ion Beam (FIB) system.



**Figure 3.4.** (a) FEI Nova NanoSEM 450 [101], (b) FEI Helios NanoLab 660 [102].

### 3.3.2. Energy Dispersive X-Ray Spectroscopy (EDS)

Most of the modern SEM instruments are coupled with EDS systems. The EDS system is used for the chemical analysis or chemical characterization of a sample. In EDS, the characteristic X-rays are emitted when a high energy beam of charged particles (usually electrons) is focused into the sample being studied. In this case, a ground state electron from the inner shell is ejected by the incident electron leaving behind an electron hole. When an electron from an outer, higher energy shell fills the hole, the difference in energy between these two shells is emitted in the form of an X-ray. The emitted X-ray spectrum is unique for each element because each element has a unique set of energy

levels. Moreover, the concentration of an element in a sample is measured by the intensity of the X-rays; the intensity of the X-ray increases as the concentration of the corresponding element increases [103]. The EDS can be used to get data from a point analysis, line scan and a full-scan X-ray mapping.

### **3.3.3. Focused Ion Beam (FIB)**

The FIB instrument is very similar to an SEM, but it uses a beam of ions instead of electrons. The ion source in the FIB is a liquid metal ion source such as gallium ion source ( $\text{Ga}^+$ ). Using this versatile instrument, several operations can be performed in one setting. In addition to the secondary electrons and ions imaging, the specimen surface can be modified (milled) with nanometer precision via the sputtering process. Furthermore, production of minute components or removal of unwanted material can be performed precisely when the energy and intensity of the ion beam are well controlled. This technique is especially powerful for exposing a cross-sectional view at any desired location on a sample and preparing TEM samples. Additionally, the FIB is able to deposit conductive or insulating materials on a specimen surface with great precision using ion beam assisted chemical vapor deposition.

Recently, both the FIB and SEM are available in one system such as in the FEI DualBeam system, which combines the benefits of the two. FEI Helios NanoLab 660, shown in **Figure 3.4** (a), is an example of these systems.

In the FIB/SEM system, high resolution images of the FIB-milled surface are also possible when both the electron and ion beams intersect at a 52° angle coincident point as shown in **Figure 3.5**.

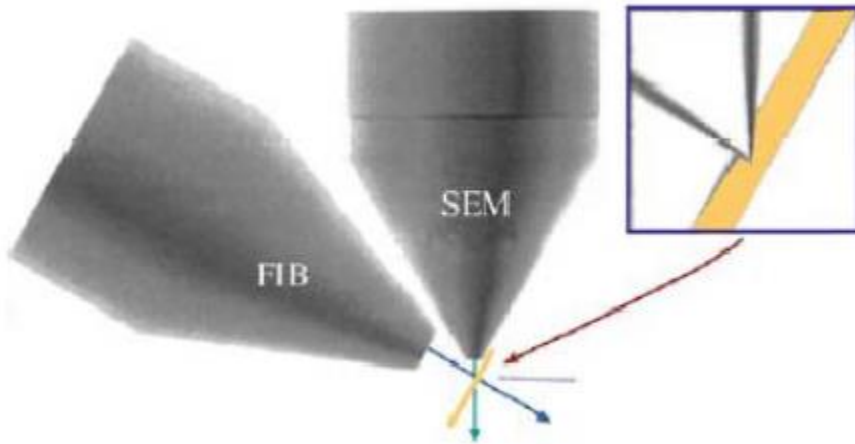


**Figure 3.5.** Schematic representation two-beam (electron and ion) FIB [100]

In this research, most of the cross-sectional views made for oxidation experiments were made using FIB. The advantage of FIB-made cross sections over traditional resin-embedded cross sections is the ability to choose different areas on the same sample and maintain the intactness of the oxide scale. Besides the possible grinding damage that may occur on the surface when preparing a cross section, resin can apply a significant amount of stress on the oxide scale during the time it sets up.

#### 4. HIGH TEMPERATURE OXIDATION OF ZIRCALOY-2 (Zry-2)

This chapter centers on the high temperature oxidation behavior of Zry-2 in steam and air. The steam oxidation experiments were carried out at 600, 800, and 1000°C while the air oxidation experiments were done at 600°C. For oxidation in air, the effect of laser shock peening (LSP) on the oxidation behavior was investigated and the results of the oxidation behavior in air were compared with those obtained from the oxidation in steam at the same temperature.

##### 4.1. Oxidation Behavior of Zry-2 Samples Oxidized in the flowing Steam at 600, 800, 1000°C

###### Oxidation Kinetics

**Figure 4.1** shows the oxidation behavior of Zry-2 in the flowing steam at the average of 100 mg/s for the steam oxidation experiments performed at 600, 800, and 1000°C. This is the continuous weight gains of the samples as a function of oxidation time. At all investigated temperatures, the weight gain increased according to the parabolic rate law at the early stages of oxidation, which is generally agreed upon for a high-temperature oxidation of Zr alloys in a steam atmosphere [104]. According to Wagner's theory [105], the parabolic oxidation behavior of Zry-2 is initially diffusion controlled at all investigated temperatures. Thus, the weight gain per unit surface area ( $\Delta W/A$ ) and oxidation time ( $t$ ) can be described as

$$\left(\frac{\Delta W}{A}\right)^2 = k_p t \quad 4.1$$

where  $k_p$  is the parabolic rate constant. **Figure 4.2** (a), (c), and (f) represent the squares of weight gain per unit surface area at the early stages of oxidation at 600, 800, and 1000°C, respectively. It is obvious that the oxidation rate is strongly dependent upon the oxidation temperature and exposure time; the initial parabolic rate constant increased as the temperature increased. Meanwhile, the weight gain at the early stage most likely resulted from the oxygen diffusion through the oxide layer in accordance with the parabolic rate. However, the transition of the weight gain as a function of time, which is called a breakaway oxidation, occurred earlier at higher temperatures. As shown in **Figure 4.1**, the oxidation kinetics was changed from a parabolic rate to a linear rate at all investigated temperatures. This suggests that the oxide layer was cracked and no longer protective. At this stage of oxidation, the relationship between the weight gain and exposure time can be described as

$$\left(\frac{\Delta W}{A}\right) = k_L t \quad 4.2$$

where  $k_L$  is the linear rate constant. **Figure 4.2** (b), (d), and (e) represents the weight gain per unit surface area as a function of time after the breakaway oxidation at 600, 800, 1000°C, respectively. The parabolic and linear rate constants were determined using **Eq. 4.1** and **Eq. 4.2**, respectively, and the approximate breakaway times for steam oxidation at all investigated temperatures are listed in **Table 4.1**.

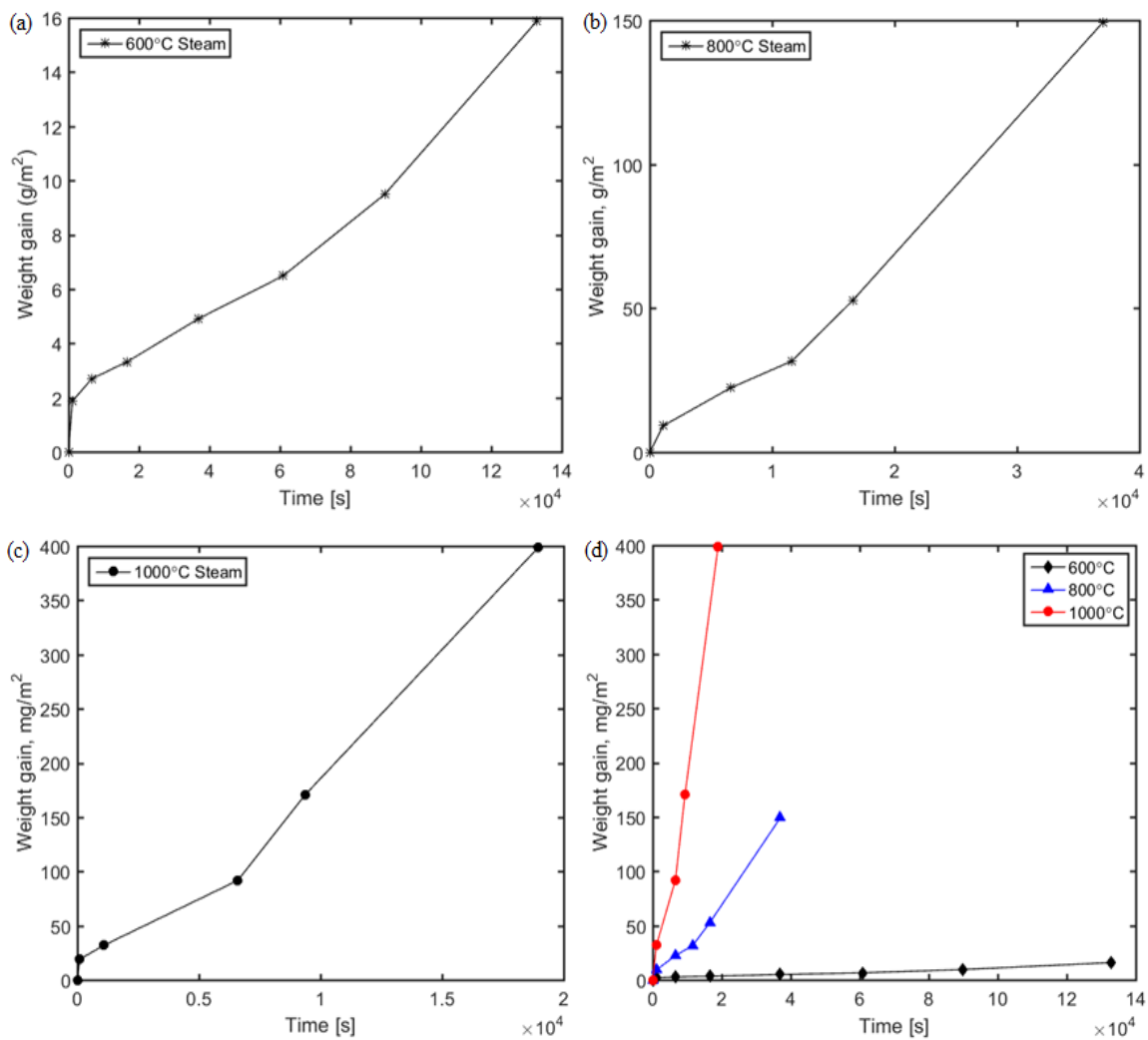


**Figure 4.1.** Oxidation behavior of Zry-2 in steam at: (a) 600°C, (b) 800°C, (c) 1000°C, (d) 600, 800, and 1000°C.

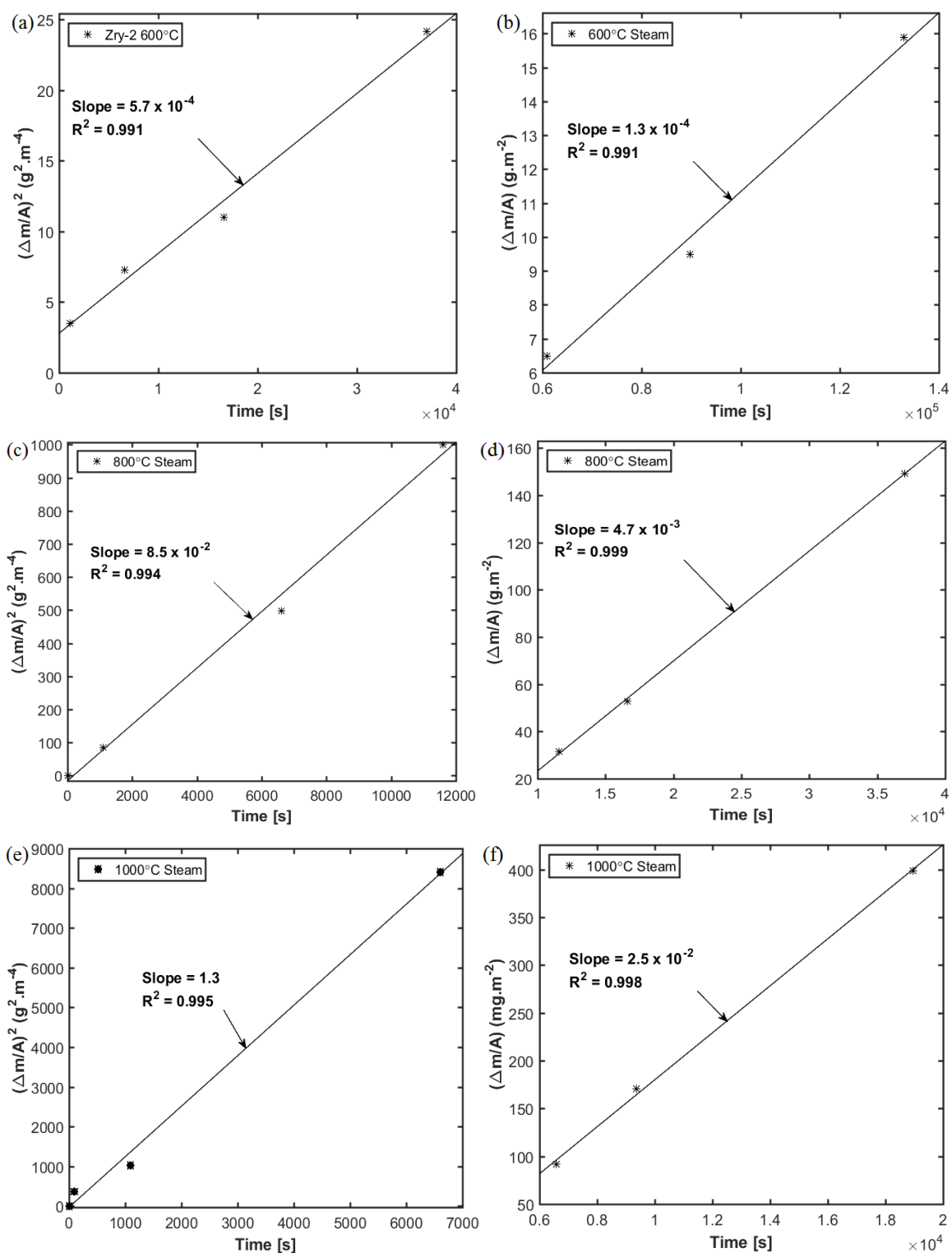


**Figure 4.2.** (a), (c), (e) Squares of weight gain as a function of time for pre-transition kinetics at 600, 800, and 1000°C, respectively; and (b), (d), and (f) weight gain as a function of time for post-transition kinetics at 600, 800, and 1000°C, respectively.

Oxidation Temperature (°C)	Pre-transition Parabolic Oxidation Constant $k_p$ ( $\text{g}^2 \cdot \text{m}^{-4} \cdot \text{s}^{-1}$ )	Estimated Transition (Breakaway Oxidation) Time (s)	Post-transition Linear Oxidation Constant $k_L$ ( $\text{g} \cdot \text{m}^{-2} \cdot \text{s}^{-1}$ )
600	$5.7 \times 10^{-4}$	61,000	$1.3 \times 10^{-4}$
800	$8.5 \times 10^{-2}$	11,600	$4.7 \times 10^{-3}$
1000	1.3	6,600	$2.5 \times 10^{-2}$

**Table 4.1.** Oxidation kinetics constants and breakaway oxidation points for Zry-2 in steam at different temperatures

### Microstructural Evolution of the Scales with Temperature

SEM observations were conducted to further understand the influence of high temperature oxidation on Zry-2. **Figure 4.3** shows typical SEM images of the surface of Zry-2 after the breakaway oxidation in steam at 600, 800, and 1000°C. Although no visible cracks are seen on the surface of the specimen oxidized at 600°C for approximately 37 h, many cracks can be seen at higher temperatures of 800 and 1000°C. However, the SEM images of the cross-sections, shown in **Figure 4.4**, reveal several microcracks below the surface of the oxide scale for the specimen oxidized at 600°C while numerous larger cracks with different orientations within the oxide scale are seen for specimens oxidized at higher temperatures. The density of these cracks increased and the cracks became wider as the temperature increased.

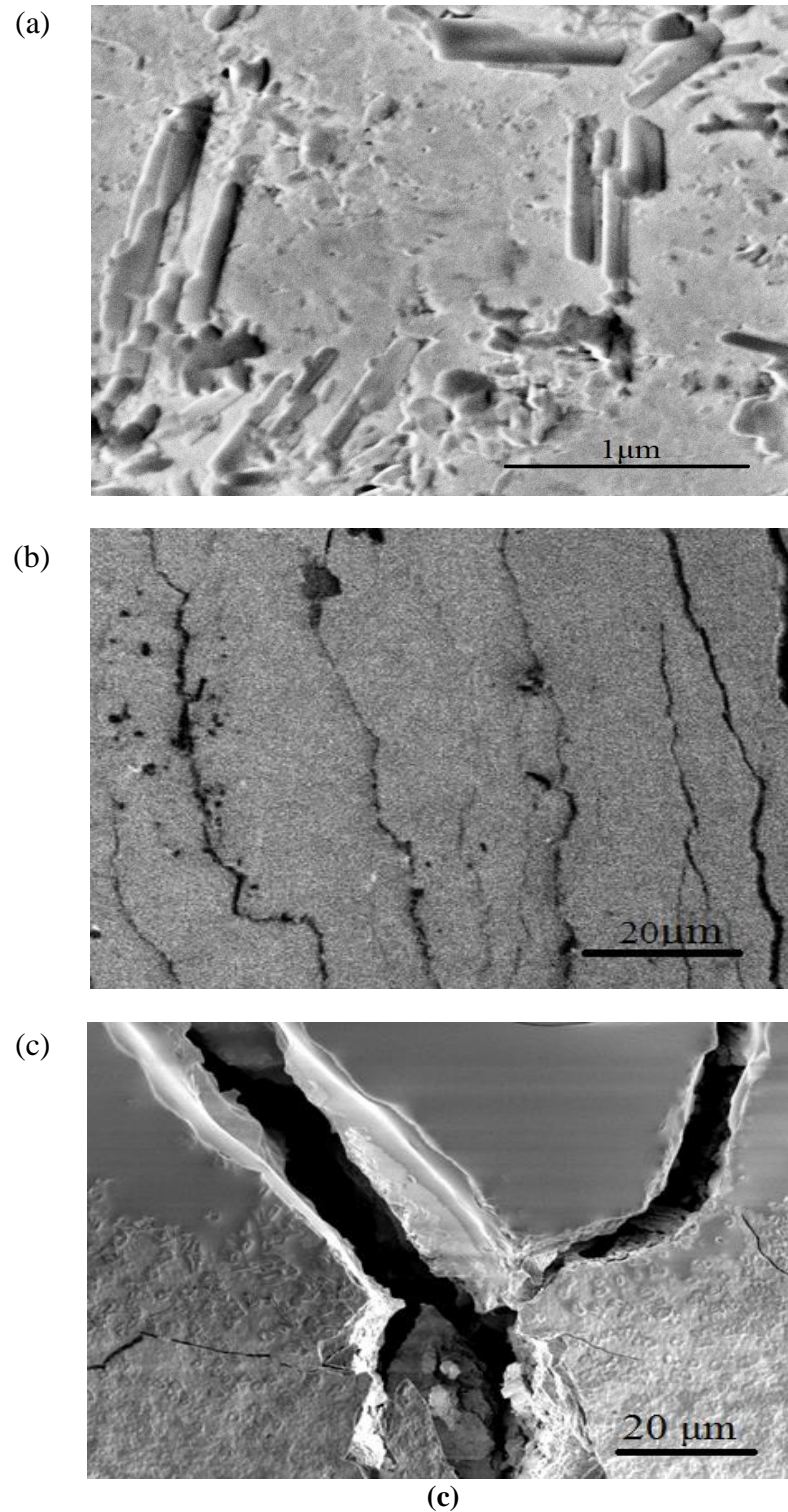


**Figure 4.3.** SEM images of the oxide scale formed on the surface of Zry-2 after breakaway oxidation at (a) 600°C for 133,000s (~37h), (b) 800°C for 37,000s (~10 h), and (c) 1000°C for 18960s (~5h).

This indicates that high temperature plays a major role in accelerating the oxidation process of Zry-2. It is apparent from **Figure 4.3** that the dense, protective oxide layer formed during the initial stages of oxidation has transformed into a porous, thick and cracked oxide layer. With careful investigation of the oxide scale formed on Zry-2, it can be seen that these cracks propagate along the crystalline boundaries in the  $ZrO_2$  film. This becomes more obvious as the temperature increases. The origin of these cracks is attributed to the low solid solubility of some of the alloying elements in the  $\alpha$ -Zr matrix which leads to the segregation of these alloys at the grain boundaries in a form of second phase particles (SPPs). This mechanism can be explained as follows. When the surface of Zry-2 is exposed to the oxidative medium, Zr is preferentially oxidized due to its relatively strong affinity for oxygen. Therefore, the second phase particles (SPPs) remain unoxidized. As the oxidation process continues, additional layers of oxide are formed but at lower rates due to the protection provided by the previous oxide layer. This is in good agreement with the oxidation kinetics results presented in **Figure 4.1**. While only zirconium atoms are oxidized so far, other atoms are continuously pushed back, forming an enriched layer of SPPs under the oxide film. When zirconium oxide is thick enough, the concentration gradient comes into play, and some of these alloying elements become prone to diffusing into the oxide layer. But, the diffusion is limited due to the relatively large size of some alloying atoms. Eventually, when the temperature is high enough, these elements diffuse into both  $ZrO_2$  via the grain boundaries and Zry-2 via vacancy diffusion. Hence, some of the alloying elements are oxidized which disrupts the oxide layer and initiates cracks at high temperatures. In addition to producing large amounts of hydrogen, the exothermal nature of the chemical reaction between Zr and steam further promotes

the increase in temperature which enhances the diffusion of alloying elements. This process is expected to change the oxide crystallography and accelerate the breakaway oxidation. Baek et al. [58] observed a similar phenomenon during the oxidation of Zr-based alloys under a steam atmosphere. The breakaway oxidation time was found to be shorter for Sn-containing Zr-alloys with higher Sn content. This was attributed to the destabilization of the tetragonal oxide layer by Sn addition and the consequent transition of  $ZrO_2$  from tetragonal phase into monoclinic phase, resulting in oxide cracking. The presence of these cracks within the oxide layer provides short paths for oxygen and hydrogen through the oxide which results in faster breakaway oxidation. **Figure 4.5** shows EDS spectrums of the oxide scale formed on the surface of Zry-2 after oxidation in steam at  $800^\circ C$  for 10h. The EDS spectrum of the cracked area of the oxide scale shows small peaks of both Sn and Fe, which also supports the above explanation of the crack initiation mechanism. Here, it should be noted that the Au signals in EDS spectrums resulted from the surface coating with a thin film of gold in order to enhance the surface conductivity and reduce the accumulation of charge.

**Figure 4.6** illustrates the EDS line-scanning profiles along the cross section of the oxide scale formed on Zry-2 after oxidation in steam at  $600^\circ C$  for 37h. In this analysis, only Zr and O were selected to investigate the extent to which the oxygen had diffused into the Zry-2 substrate. The O  $K\alpha$  peaks are clearly seen several microns away from the main oxide layer towards the substrate. This is postulated to have occurred due to the short diffusion paths that resulted from the cracks within the oxide layer.

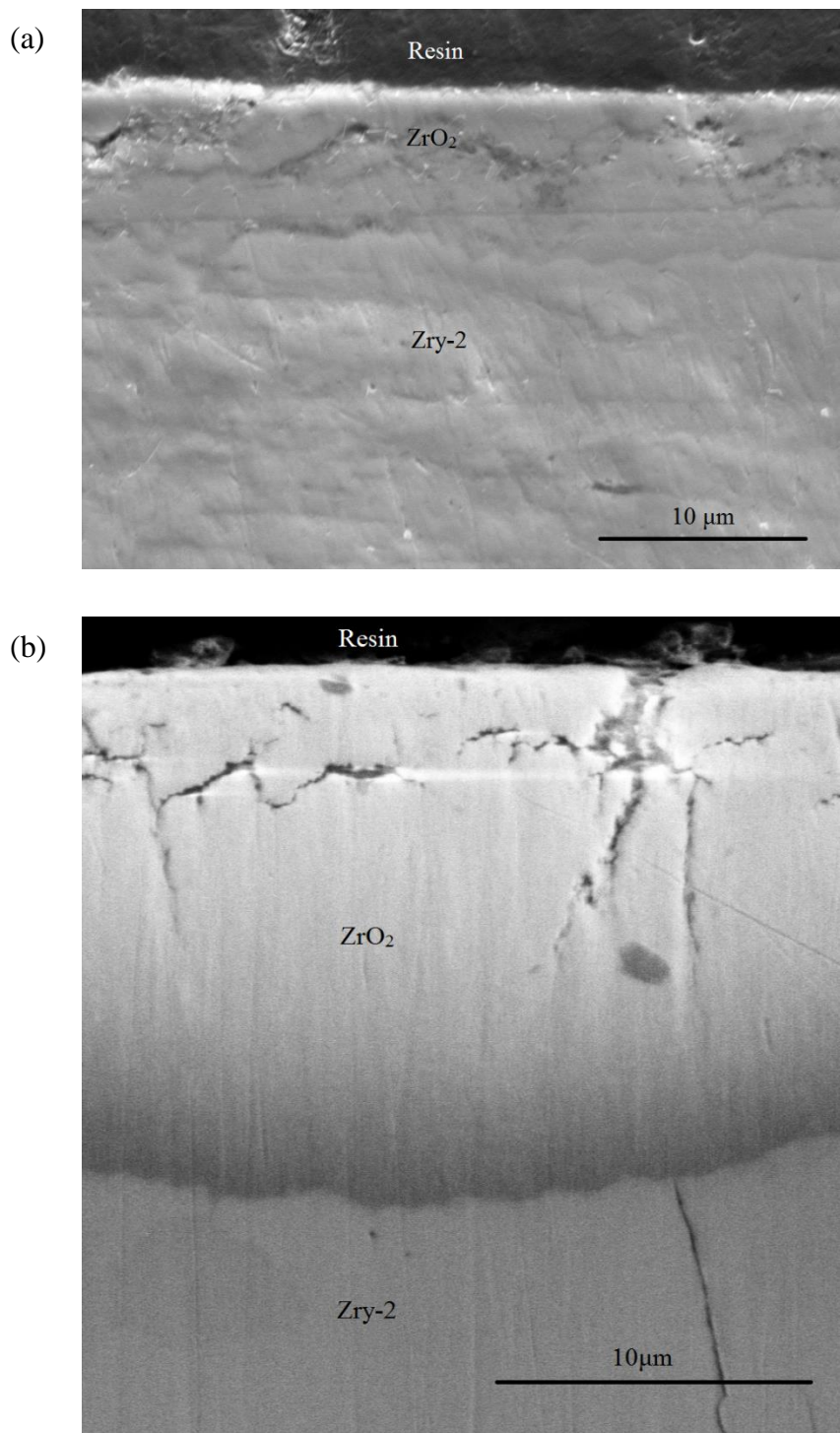


**Figure 4.4.** Cross sectional SEM SE micrographs of Zry-2 oxidized in steam at (a) 600°C for 133,000s (~37h), (b) 800°C for 37,000s (~10 h), and (c) 1000°C for 18960s (~5h).

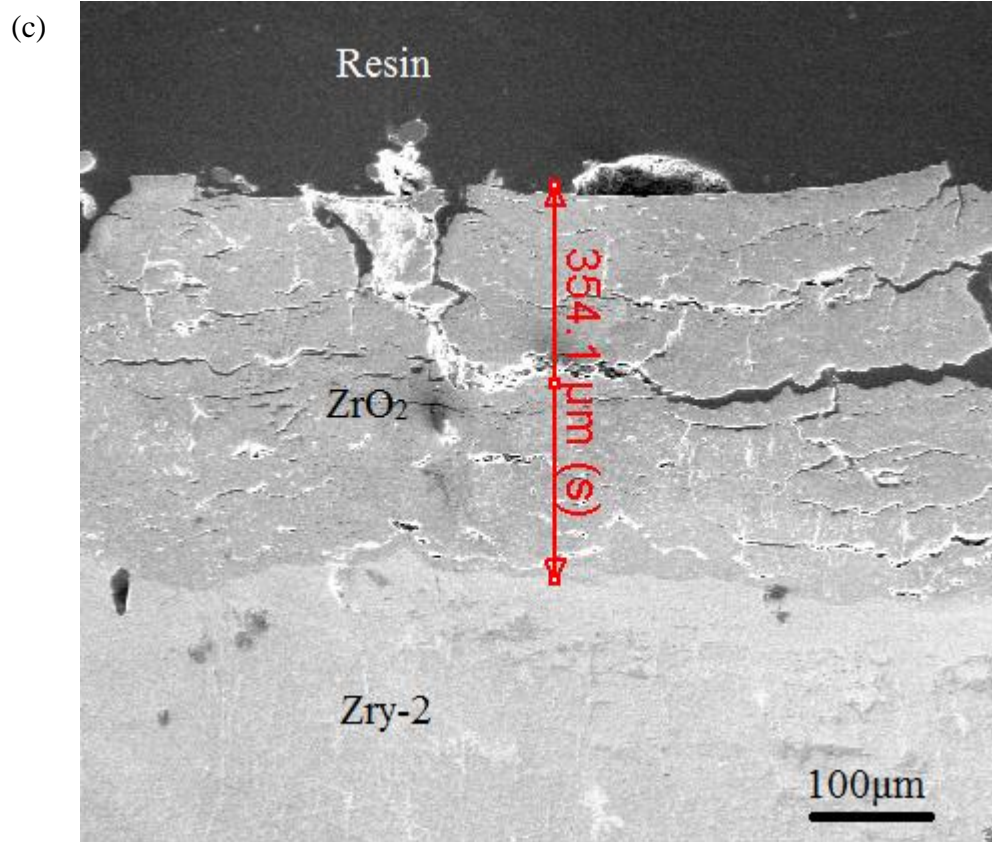
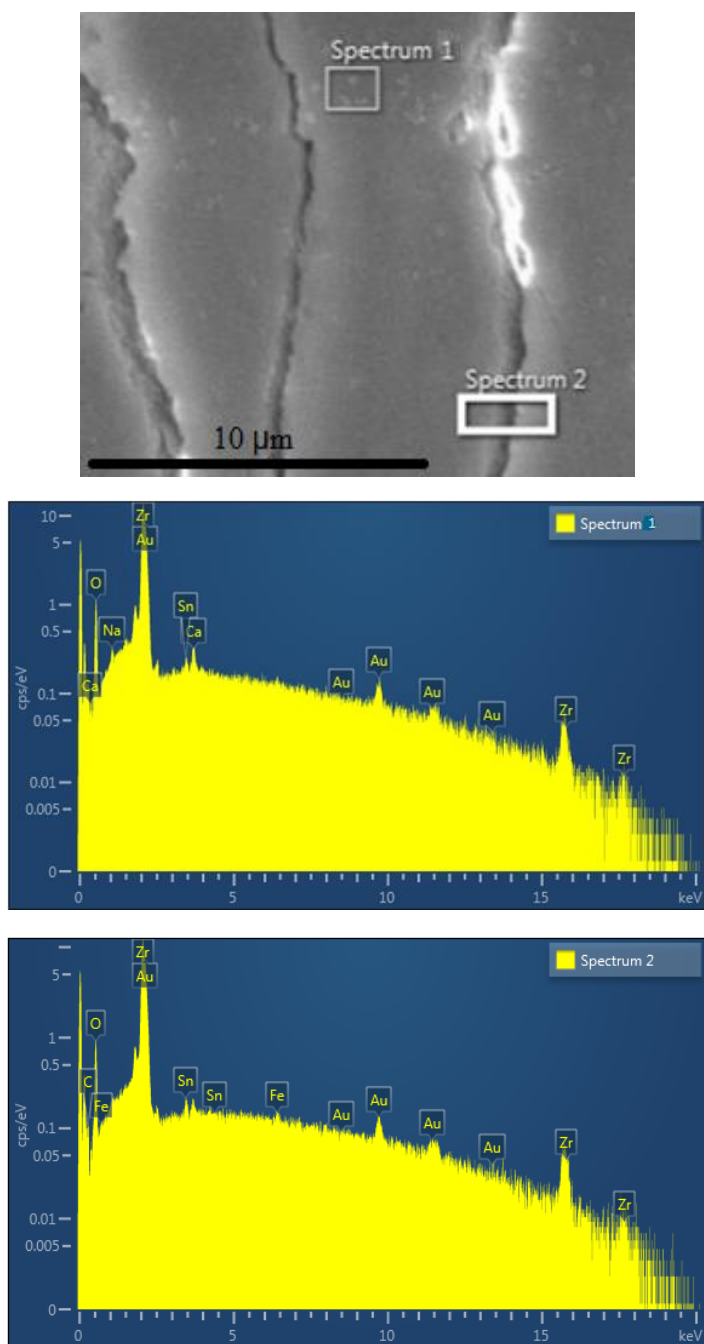
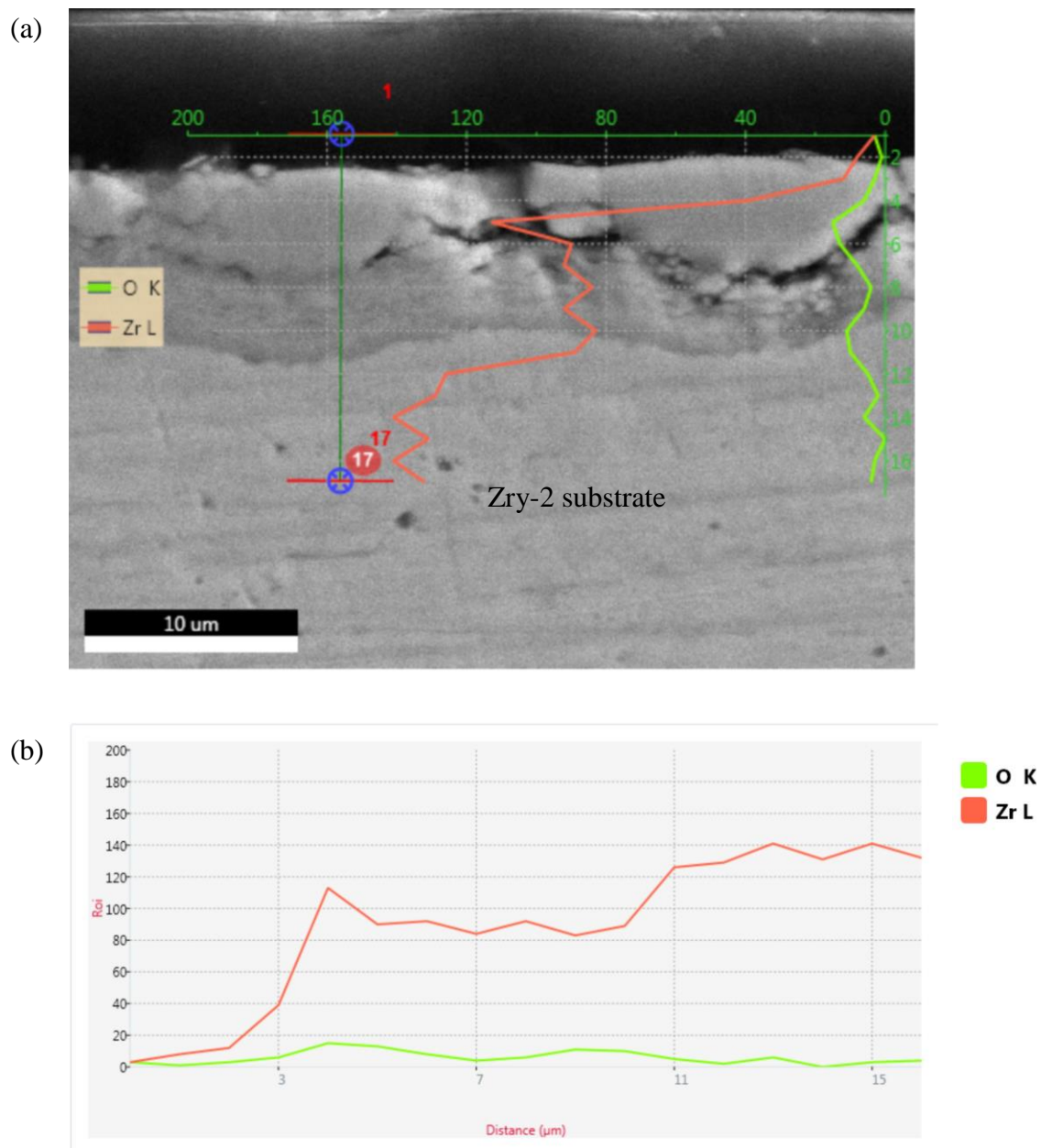


Figure 4.4 continued.



**Figure 4.5.** (a) SEM micrograph of the oxide scale from on the surface of Zry-2 oxidized in steam at 800C (b) EDS spectrum of the intact area shown in (a), and (c) EDS spectrum of the cracked area in (a)



**Figure 4.6.** (a) Cross-sectional SEM micrograph of Zry-2 after oxidation at 600°C for 133,000s (~37h) in a flowing steam at 100 mg/s. (b) EDS line-scanning profiles along the line shown in (a). Note: Roi means region of interest counts.

## 4.2. Oxidation Behavior of Zry-2 Samples Oxidized at 600°C in Air

### Oxidation Kinetics

**Figure 4.7** shows the oxidation behavior of Zry-2 in air at 600°C, including weight gain per unit surface area as a function of time and the post-transition rate constant. During the pre-transition, the oxidation rate follows a parabolic rate law for approximately 3.5 h. This behavior can be explained by the growth of a dense and protective oxide scale, controlled by the diffusion of oxygen, which is quite similar to that for oxidation in steam. However, the breakaway oxidation during the oxidation in air took place in a significantly shorter time than that in steam at the same temperature. This is attributed to the influence of nitrogen on the oxidation of zirconium alloys in air which will be explained further in this section. Duriez et al [105] and Coindreau et al. [106] also confirmed the strong influence of nitrogen-containing atmospheres on zirconium alloys corrosion resistance. After the kinetic transition, the oxidation curve changed from parabolic to linear indicating that the oxidation rate is no longer controlled by the oxygen diffusion through the oxide layer. This transition is associated to the formation of cracks close to the  $ZrO_2/Zry-2$  interface that could result from several possible mechanisms including the oxide transformation from the tetragonal to the monoclinic form. **Eq. 4.2** was used to calculate the post-transition kinetics rate constant  $k_L$ . This was found to be  $1.3 \times 10^{-3} \text{g.m}^{-2}.\text{s}^{-1}$ , which is one order of magnitude higher than kinetics rate constant in steam. The higher rate constant indicates that oxidation in air is more severe than oxidation in steam, which results from the lower thermal conductivity of air than for

steam. It should also be noted that oxidation in air was conducted in an open hearth furnace where oxygen starvation was possible while oxidation in steam was conducted in the steam furnace where pure steam continuously pushed over the specimen. **Figure 4.8** shows photographs of the partially oxidized Zr-2 specimens in air at different times corresponding to the pre-transition and post-transition regions. It is obvious that the oxidation took place uniformly on the entire surface up to the onset of the breakaway oxidation. Then, the cracking took place at the specimen edges during oxidation time corresponding to the kinetic transition while the central area of the specimen stayed in the pre-transition state. Subsequently, the cracking advanced towards the center of the specimen until the whole surface was cracked. This could explain the stable linear oxidation kinetics after the short time needed for the complete oxidation transition.

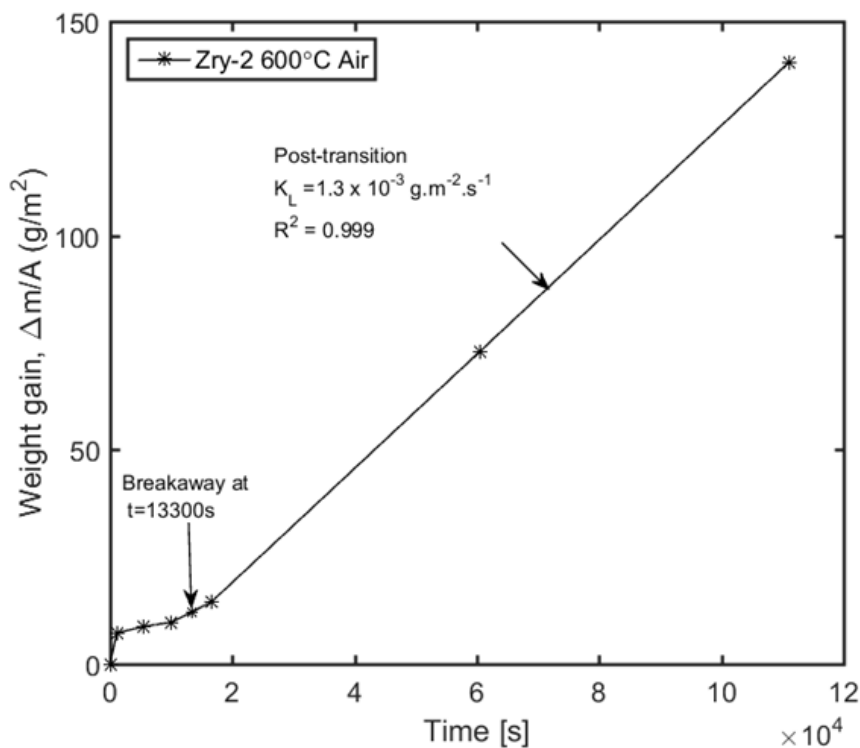


**Figure 4.7.** Weight gain per unit surface area as a function of time for Zry-2 oxidized in air at 600C.

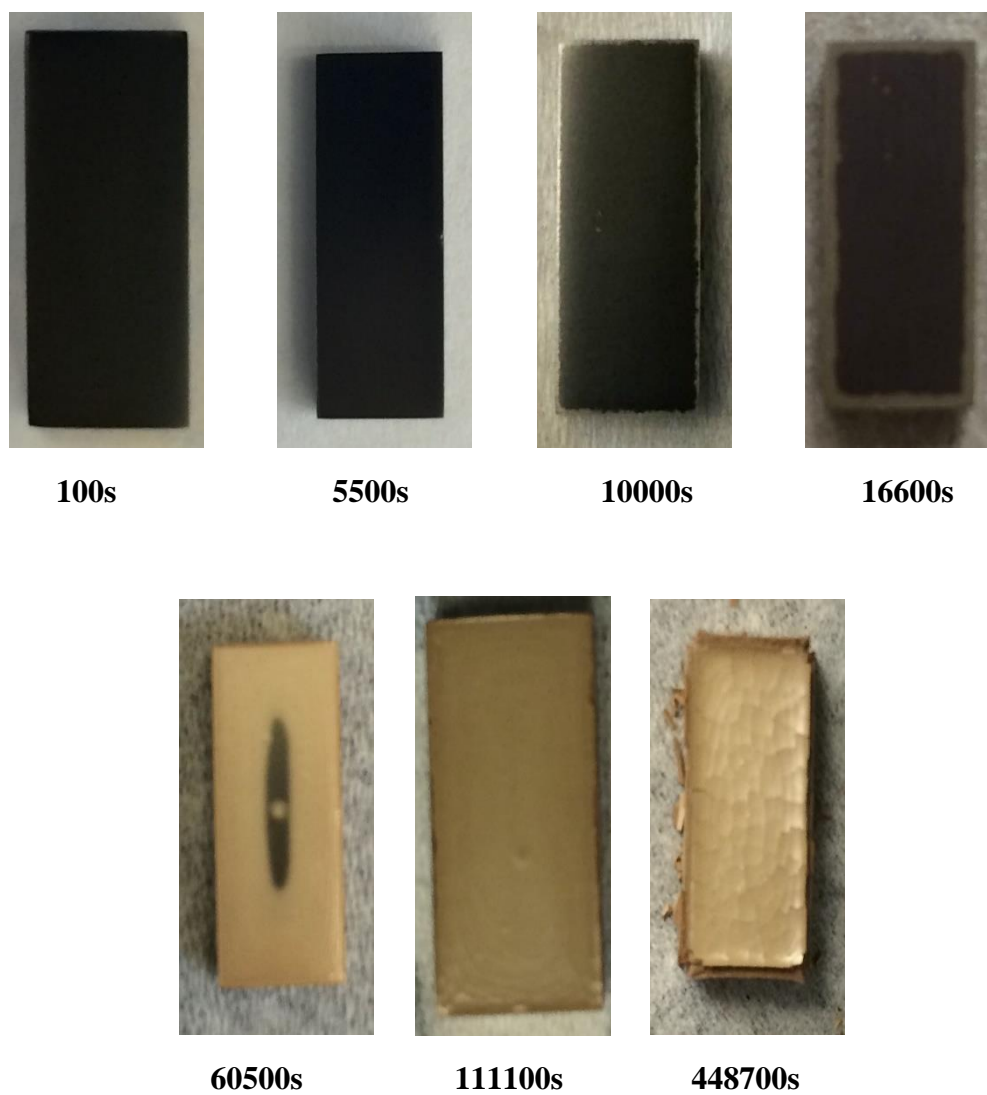


**Figure 4.8.** Photographs of partially oxidized Zry-2 samples in air at 600°C after oxidation for the indicated times.

### SEM Examination

**Figure 4.9** (a) – (c) shows SEM SE images of the oxide scale formed on the surface of Zry-2 oxidized in air at 600°C for different periods of time. For the times corresponding to the pre-transition stages (5,500s and 10,000s), the oxide scale formed on the surface of Zry-2 is very dense and protective. This agrees well with the parabolic oxidation rate, which suggests that the oxidation rate is controlled by the diffusion of oxygen vacancies in the oxide scale. Although no cracks were clearly observed on the oxide surface corresponding to the breakaway oxidation time (Figure 4.9 (c)), the oxide scale is clearly less compact than that formed during the pre-transition stage. Additionally, several cracks can be located close to the ZrO<sub>2</sub>/Zry-2 interface. These cracks are indicated by arrows in **Figure 4.10**, an SEM SE image of the oxide cross-section after oxidation for 16,600s. The microstructural change represented by the oxide transformation from the tetragonal to the monoclinic form is considered the most possible mechanism for the crack formation in the oxide scale. This was also observed by Duriez [106] and others for air oxidation of Zircalloys at elevated temperatures. Consequently, the diffusion paths for oxygen and nitrogen through the oxide scale are decreased and the corrosion resistance of the scale is damaged. Shortly after these cracks propagate to the entire surface of a sample, the oxidation rate becomes more stable and the whole surface starts to experience a post-transition linear kinetics.

Regardless of the oxidant (oxygen and hydrogen in steam, oxygen and nitrogen in air), the post-transition oxidation rate is linear and relatively close when the influence of nitrogen in air is assumed to be weak and no oxygen starvation is possible [104].

However, most of the experiments conducted in this area used the flowing air while the current study did not. So, it is very likely that the oxygen starvation occurred in the cracks of the oxide during the air oxidation of Zry-2. Although no XRD analyses were carried out in this study, many others reported formation of zirconium nitride particles in the oxide scale formed on Zircalloys at high temperatures. As a result, it is assumed here that nitrogen has played an influential role in increasing the oxidation rate in comparison with oxidation in steam at the same temperature. In other words, nitriding kinetics dominates the kinetics rate when the oxygen partial pressure decreases in the cracks and leads to the formation of zirconium nitride or oxinitride. Upon an increase in oxygen partial pressure, the oxidation kinetics starts to dominate the reaction again and the nitride particles are re-oxidized. This occurs because the oxide is thermodynamically more stable than the nitride [107]. Hence, nitrogen is released in the oxide or in the metal which leads to a volume increase since the molar volume of oxide is greater than the molar volume of nitride. This change in volume enhances cracking of the oxide and leads to a faster oxidation kinetics.

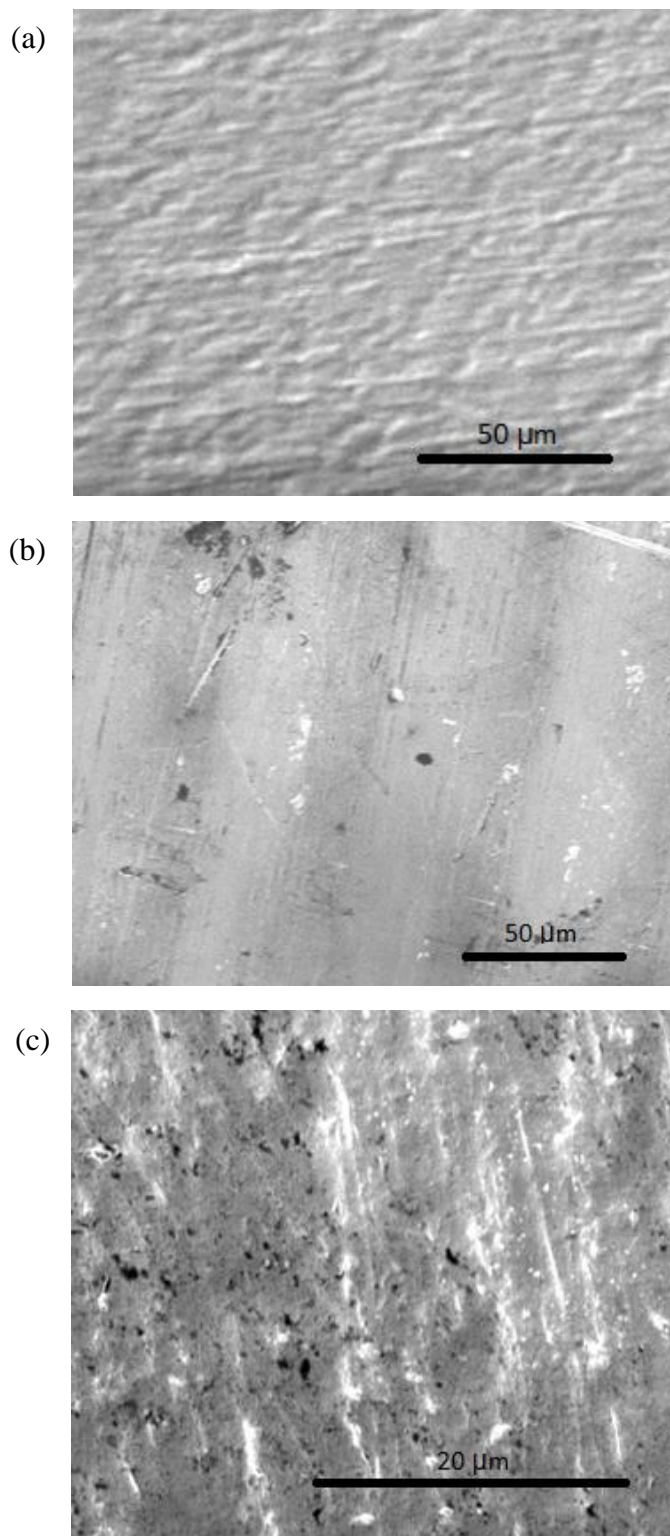


**Figure 4.9.** SEM SE images of the oxide scale formed on the surface of Zry-2 oxidized in air at 600°C for (a) 5500s, (b) 10000s, and (c) 16600s

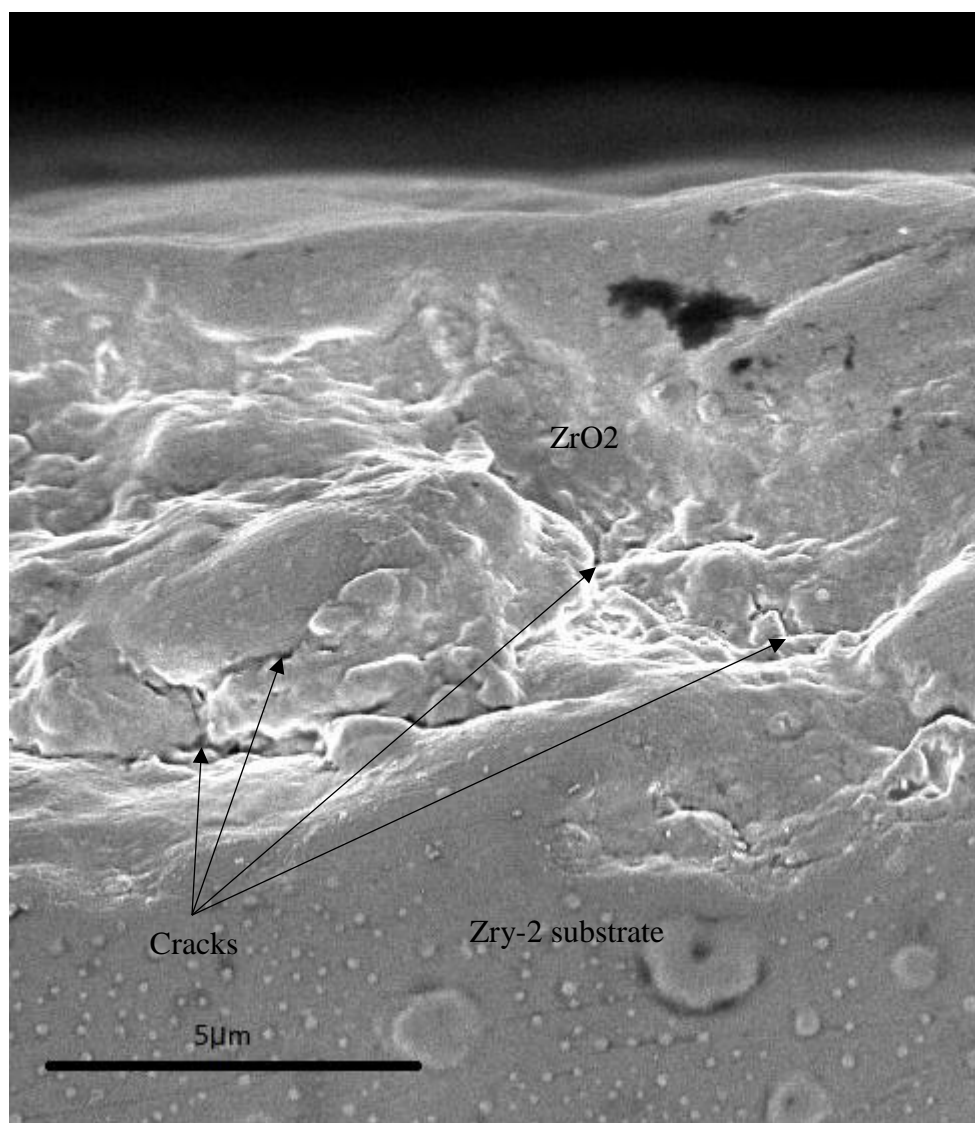


**Figure 4.10.** SEM SE image of the fracture cross-section of the external part of the oxide scale formed on Zry-2 after oxidation in air at 600°C for 16,600s.

### 4.3. Oxidation Kinetics of LSP and Untreated Samples at 600°C in Air

#### LSP and Oxidation Resistance

Although the oxidation resistance of alloys treated by LSP has been rarely investigated, several studies were published in this area, indicating the improvement of the oxidation resistance after the LSP. The process was performed on different alloys, and the results were promising for improving their oxidation resistance. According to Hua et al. [93] the high temperature oxidation resistance of Ni-based super alloy GH586 in static air was significantly improved by the laser shock peening. The oxidation kinetics obeyed a parabolic rate law at 800 and 900°C which was lower after LSP due to the formation of a dense, tiny and homogeneous oxide layer. In a separate study [110], it was found that the hot corrosion resistance of TC11 Titanium alloy in Na<sub>2</sub>SO<sub>4</sub> containing 20 wt.% NaCl was improved by 50% after it was treated by laser shock peening. This was associated with the formation of more protective oxidation films such as TiO<sub>2</sub>, Al<sub>2</sub>O<sub>3</sub>, MoO<sub>3</sub>, etc. on the LSP treated samples which was caused by the generation of high amount of twins and highly tangled and dense dislocation arrangements and grain refinement. Trdan and Grum [109] also studied the effect of laser shock peening without coating (LSPwC) on the corrosion behavior of AA6082-T651 alloy in a near natural chloride environment. The results showed that the corrosion resistance of the LSPwC treated samples was significantly greater than that of untreated samples. Here, the idea was adopted in an attempt to improve the high temperature oxidation resistance of Zry-2 at elevated temperatures. However, the LSP effect on the oxidation behavior of Zry-2

was rather damaging. Following are the results of the oxidation kinetics and the effects of the LSP treated Zry-2 after oxidation in air at 600°C.

### **LSP Parameters**

The LSP experiments were performed using Q-switched Nd:YAG laser with a wavelength of 1.06  $\mu\text{m}$ . Pulse energy of the laser system for pre-oxidation and post-oxidation Zry-2 samples was 850 mJ and 400 mJ, respectively. The laser beam spot on the target was set to 1 mm with an overlapping rate of 50% during LSP.

### **Oxidation Kinetics**

**Figure 4.11** compares the oxidation kinetics of an as-received Zry-2 sample to a pre-oxidation LSP treated sample and another which was treated before the onset of oxidation transition at 5,500s. As it was investigated previously, the oxidation kinetics of the untreated Zry-2 sample (Sample 1) obeyed a parabolic rate law after a short increase in weight gain with exposure time. This increase in weight is commonly attributed to the growth of the initially protective  $\text{ZrO}_2$  scale. The oxide breakdown occurred after approximately 3.5 h of oxidation in air at 600°C and the oxidation kinetics followed a linear rate law. Although the initial increase in  $(\Delta W/A)$  was very similar for both the LSP treated and untreated samples, the LSP treated samples showed different behaviors afterward. Sample 2, which was LSP treated four times at a pulse energy of 850 mJ prior the oxidation test, showed an increase in  $(\Delta W/A)$  up to approximately 5,500s. Then, the  $(\Delta W/A)$  became stable and had almost a constant difference compared to Sample 1 for the

remainder of the experiment time. On the contrary, Sample 3, which was LSP treated four times using a lower LSP energy (400 mJ) after it was oxidized for 5,500s, exhibited a consistent increase in  $(\Delta W/A)$  with oxidation time.

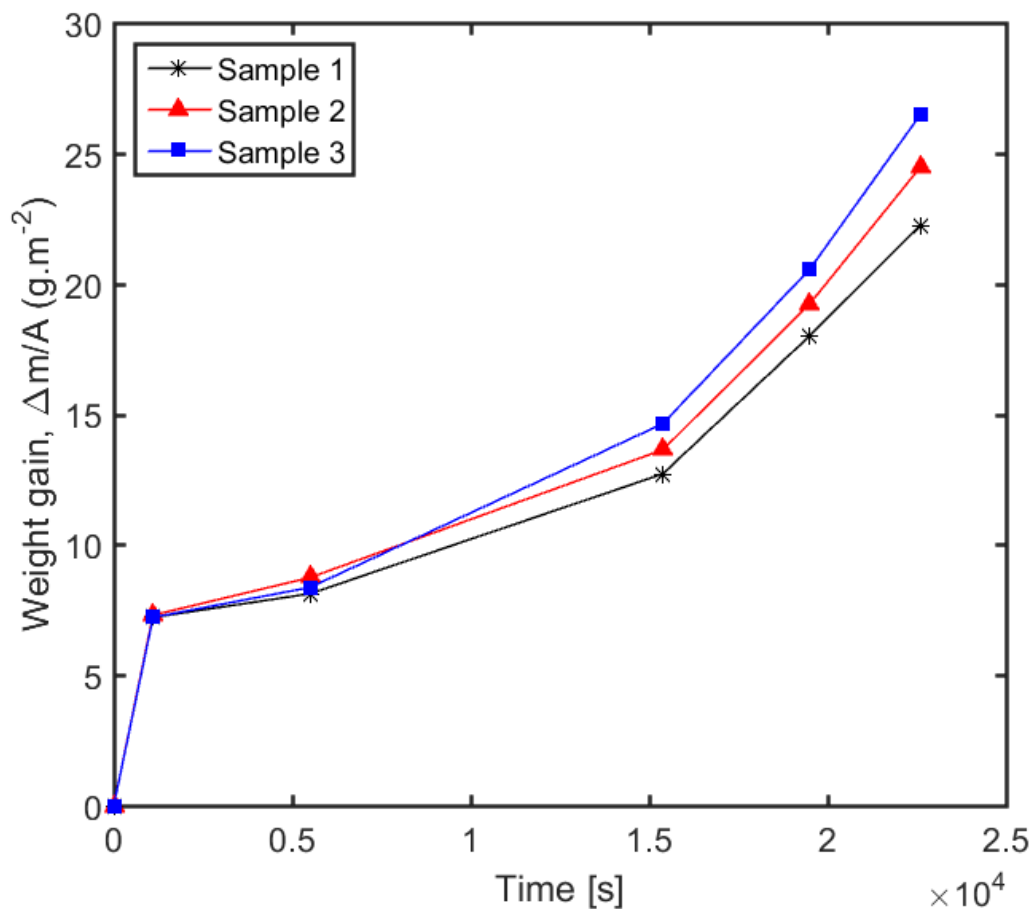


**Figure 4.11.** Oxidation kinetics curves of an as received Zry-2 sample (Sample 1) in comparison with a pre-oxidation LSP treated Zry-2 sample (Sample 2) and a post-oxidation LSP treated Zry-2 sample (Sample 3) in air at 600°C.

The difference in oxidation kinetics rate constants for LSP treated and untreated Zry-2 samples after the breakaway oxidation is illustrated in **Figure 4.12**. After the breakaway oxidation, all three samples followed a linear rate law. The kinetics rate

constant for the as-received sample was found to be exactly the same as it was previously obtained from the air oxidation of Zry-2 at 600°C. This indicates the accuracy of using the same atmosphere and experimental set ups. However, the post-transition kinetics rate constants of the LSP treated samples were found to be higher than that for the untreated sample. The linear rate constants, calculated using Eq. 2, are shown in Figure 4.12, assuming a linear post-transition behavior and the slopes of the lines correspond to the kinetics rate constants.

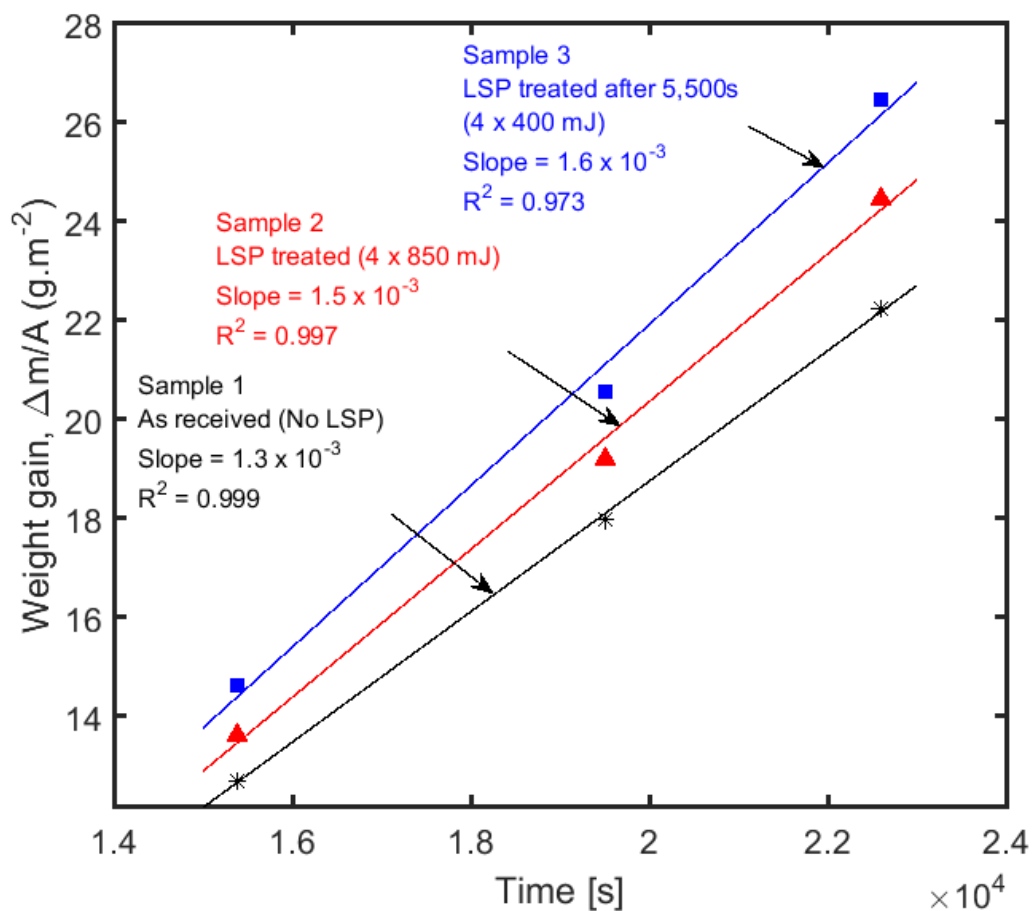


**Figure 4.12.** Difference in the oxidation rate kinetics constants between LSP treated and untreated Zry-2 samples after the breakaway oxidation in air at 600°C for ~ 6 h and 15 min.

Although the difference between any of the two LSP treated samples and the untreated sample is insignificant, Sample 3 shows the larger difference. This could be associated with the damage produced on the oxide scale by the LSP. Even though the pulse energy was very low, it is believed to have damaged the protective oxide scale since Sample 3 was already oxidized when it was LSP treated.

#### 4.4. Effect of LSP on Zry-2 Samples

The LSP effect on the Zry-2 samples is clearly visible in the photographs taken of the surface. **Figure 4.13** presents these photographs with details of the LSP energies used. It is obvious that Sample 3 is the most effected sample by LSP. The lines generated by the LSP on the surface are clearly seen. This is expected to have damaged the oxide scale and generated short paths for oxygen and nitrogen into the  $ZrO_2/Zry-2$  interface which resulted in a significant increase in  $(\Delta W/A)$  with the exposure time. One of the possible reasons for this damaging effect is the LSP parameters used in this study such as the laser beam spot size (1 mm) and the number of pulses. The successful previous utilization of this process to enhance the corrosion resistance adopted a laser beam spot size of 4 mm [93], which is four times larger than the one used in the current study. The laser beam with a small spot size expands like a sphere while the one with a large spot size behaves like a planar front [110]. Although the propagation distance for the smaller configuration reduces [111], it is expected to be more detrimental to a very thin oxide scale.

Platt et al. [63] showed that different surface roughness of Zircaloy demonstrate different oxidation behaviors with the initially rougher surface exhibiting enhanced oxidation. It was further revealed that the peaks in surface roughness of this material are preferentially corroded due to out-of-plane stresses [63]. Meanwhile, a significant increase in the surface roughness by the LSP was confirmed Petan et al. [112]. This is also evident on the surface of the all LSP treated samples in this study, and it is expected to be the primary reason for the increase in  $(\Delta W/A)$  versus time for Sample 3, which was LSP treated before the oxidation process.

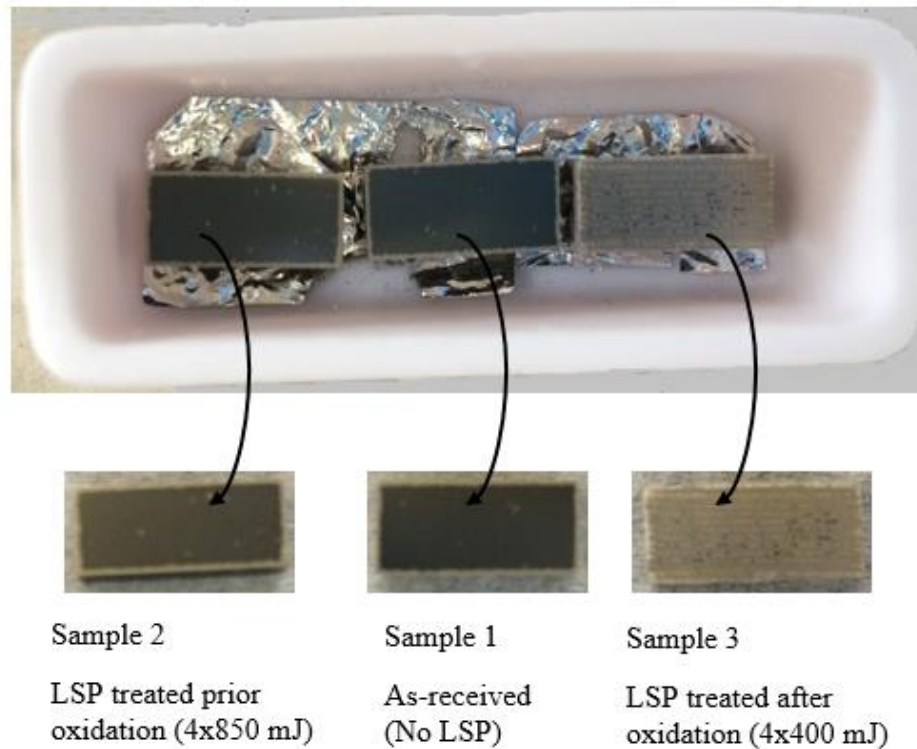


**Figure 4.13** Photographs show the difference in surface appearance between LSP treated and untreated Zry-2 samples after oxidation in air at 600°C for ~ 6h and 15 min.

#### 4.5. Summary

The oxidation behavior of the Zry-2 in both steam and air atmospheres and the effect of LSP on the oxidation behavior in air have been investigated. The oxidation kinetics of Zry-2 followed a parabolic rate law before the breakaway oxidation and changed into a linear post transition rate law at the all investigated temperatures. The breakaway oxidation was found to be generally dependent on the oxidation temperature; it took place earlier as the temperature was increased. Meanwhile, the oxidation of Zry-2 in air was more severe than it was in steam, and the oxidation breakaway took place sooner in air than it did in steam. The microstructure of  $ZrO_2$  formed on the surface of Zry-2 during the pre-transition stage was continuous, dense and protective. On the other hand, the post-transition  $ZrO_2$  oxide was porous and cracked.

After the approximate time of transitioning from parabolic to linear rate was found, the effect of LSP on the oxidation behavior of Zry-2 has been investigated. The LSP was only employed for air oxidation at  $600^\circ C$  and the effect was found to be damaging for the both the pre-oxidation and post-oxidation treatment.

## 5. HIGH TEMPERATURE OXIDATION OF Ti<sub>2</sub>AlC

In this chapter, the oxidation behavior of Ti<sub>2</sub>AlC at 600, 800, and 1000°C in the flowing steam is investigated. This also includes the influence of the steam flow rate on the oxidation kinetics at different temperatures and a comparison between the oxidation kinetics of Ti<sub>2</sub>AlC and Zry-2 in a steam atmosphere.

### 5.1. Oxidation Behavior of Ti<sub>2</sub>AlC at 600, 800, 1000°C in the Flowing Steam

#### 5.1.1. Oxidation Kinetics

Oxidation behavior of Ti<sub>2</sub>AlC samples at 600, 800, and 1000°C in the flowing steam is illustrated in **Figure 5.1**. Kinetics data was analyzed according to linear, parabolic, and cubic laws by plotting the number, square and cube of the weight gains per unit surface area, respectively, versus the oxidation time. Since the oxidation rate could be changed in terms of the oxidation temperature, the relationship between the weight gain per unit surface area and reaction time can be generalized as follows:

$$\left(\frac{\Delta W}{A}\right)^n = k_n t \quad 5.1$$

where  $(\Delta W/A)$  is the weight gain per unit surface area,  $k$  the rate constant, and  $t$  oxidation time. The value of exponent  $n$  in the above equation is  $n = 1, 2, \text{ or } 3$  according to the best linear regression fitting line for linear, parabolic, or cubic rate law.

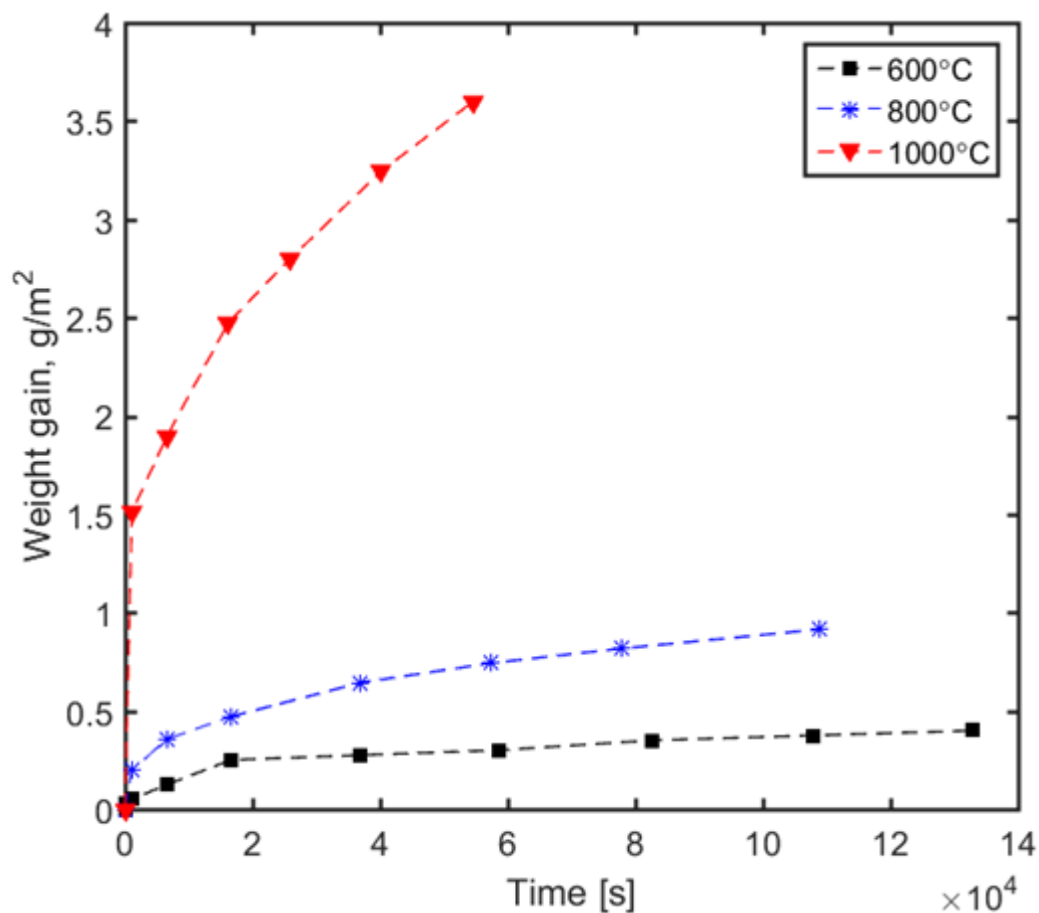


**Figure 5.1.** Plots of weight gain of  $Ti_2AlC$  per unit surface area as a function of exposure time at 600, 800, and 1000°C in the flowing steam at 50 mg/s.

$Ti_2AlC$  shows an excellent oxidation resistance at all investigated temperatures in the flowing steam at 50 mg/s. After a relatively rapid initial change in mass, the oxidation reaction slows down significantly due to formation of a protective scale on the surface.

The oxidation kinetics of  $Ti_2AlC$  obeys a parabolic rate law at relatively low temperatures, 600 and 800°C, while it follows a cubic rate law at 1000°C. **Figure 5.2** (a) and (b) show the square and cube of the weight gains per unit surface area versus the oxidation time, yielding approximately straight lines for oxidation behaviors at 600 and 800°C, and 1000°C, respectively. The slope of these lines were used to estimate the

kinetics rate constants. This shows that the oxidation kinetics constant for samples oxidized at 600°C is lower than that for samples oxidized at 800°C by approximately one order of magnitude. Here, it should be noted that fitting of the oxidation data at 800, and 1000°C into both parabolic and cubic rate laws yielded very high correlation coefficients. However, a parabolic rate law is assumed for oxidation of Ti<sub>2</sub>AlC at 800°C and both parabolic and cubic rate laws are presented for oxidation at 1000°C for the sake of comparison (**Figure 5.2b** and c). The parabolic rate suggests that the growth of the oxide scale is diffusion controlled at these temperatures. However, a cubic rate law is assumed for oxidation of Ti<sub>2</sub>AlC at 1000°C rather than a parabolic rate law due to the better regression fitting line resulted from plotting  $(\Delta W/A)^3$  versus exposure time, which yielded a slightly higher correlation coefficient. The cubic rate law is commonly observed during high temperature oxidation, where  $(\Delta W/A)^3 = k_c \cdot t$  is used to describe the oxidation kinetics. Basu et al. reported a cubic rate law rather than a parabolic one for Ti<sub>2</sub>AlC oxidized at temperatures 1000 - 1300°C in both air and water vapor [80]. This was attributed to a more complex oxidation mechanism at this range of temperature, assuming diffusion of more than one species in the oxide system [80]. In a separate study [78], Wang and Zhou also observed a cubic rate law for oxidation of Ti<sub>2</sub>AlC in air at 1000 – 1300°C. However, no explanation was provided for such behavior except comparing it to the Near-cubic oxidation behavior of other alumina-forming alloys such as NiCrAl and FeCrAl [113], in which the growth of the oxide scale is governed by oxygen grain boundary transport. Similarly, the cubic rate that is generally observed during the pre-transition kinetics of Zircalloys in water is attributed to the mass transfer along the grain boundaries and the continuous growth of the scale grain size with

increasing the oxide thickness [123]. **Table 5.1** presents the kinetics rate constants of  $\text{Ti}_2\text{AlC}$  oxidized at different temperatures in the flowing steam at 50 mg/s. Although the rate of oxidation kinetics increases as the temperature increases, the oxide scale maintains a perfectly dense structure, free from any cracks and adhesive to the substrate. More details about the oxide microstructure is provided in the following section.

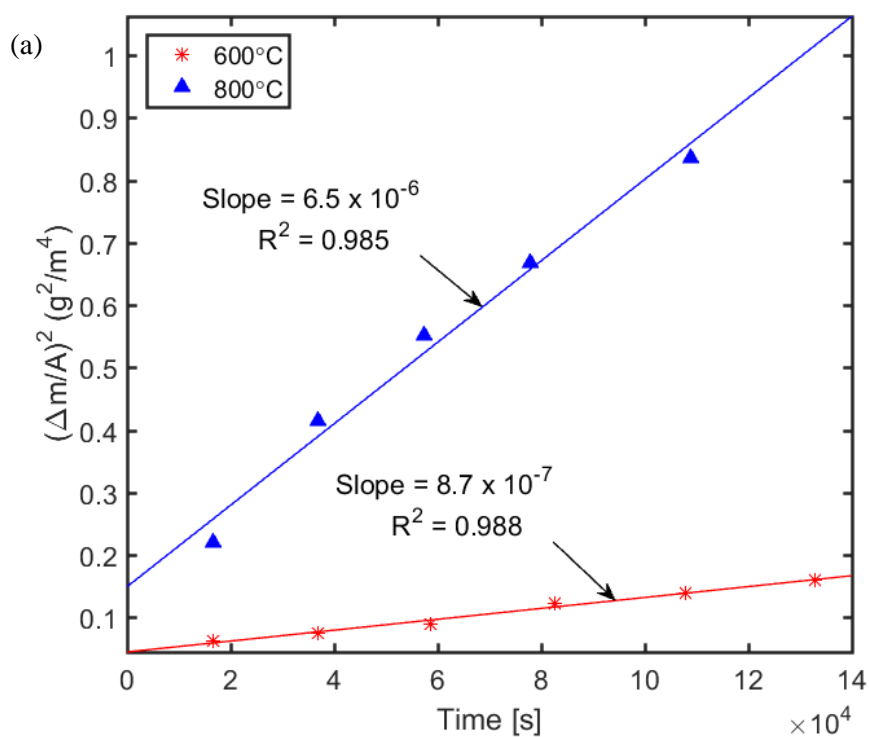


**Figure 5.2.** (a) square of the weight gains versus exposure time of  $\text{Ti}_2\text{AlC}$  at 600 and 800°C, and (b) and (c) cube and square of the weight gain versus exposure time of  $\text{Ti}_2\text{AlC}$  at 1000°C.

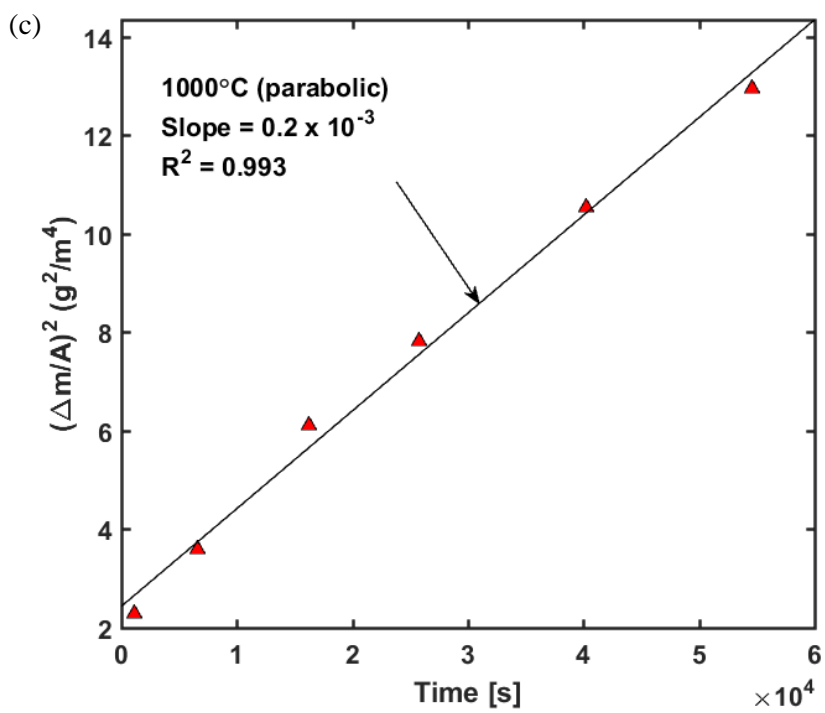
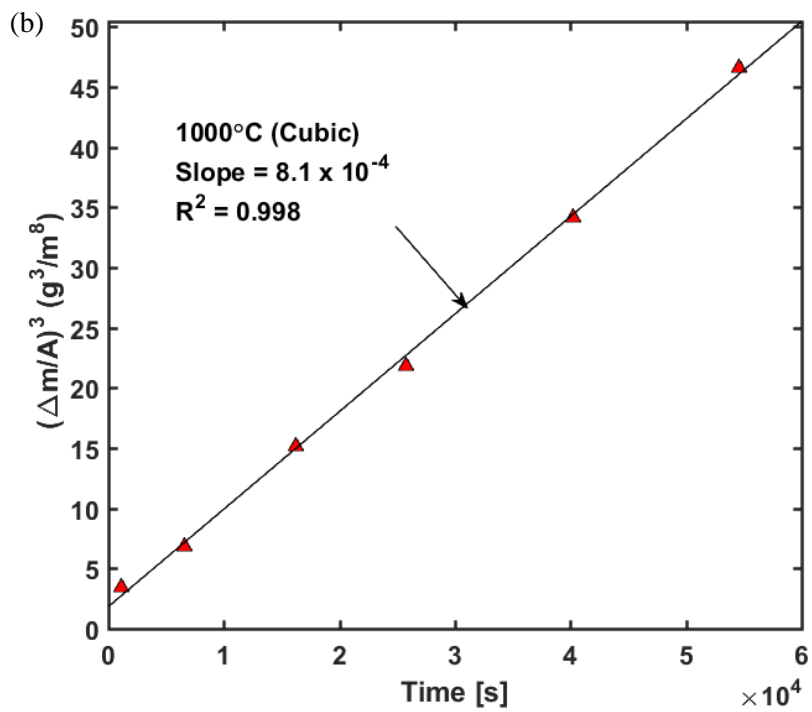


(Figure 5.2 continued)

Temperature T(°C)	Kinetics Rate Constant
600	$k_P = 8.7 \times 10^{-7} \text{ g}^2 \cdot \text{m}^{-4} \cdot \text{s}^{-1}$
800	$k_P = 6.5 \times 10^{-6} \text{ g}^2 \cdot \text{m}^{-4} \cdot \text{s}^{-1}$
1000	$k_C = 8.1 \times 10^{-4} \text{ g}^3 \cdot \text{m}^{-6} \cdot \text{s}^{-1}$ $k_P = 0.2 \times 10^{-3} \text{ g}^2 \cdot \text{m}^{-4} \cdot \text{s}^{-1}$

**Table 5.1.** Kinetics rate constants for samples oxidized at different temperature in the flowing steam at 50 mg/s.

### 5.1.2. Microstructural Evolution of the Scales with Temperature

Oxidation experiments performed at 600, 800, and 1000°C in the flowing steam at 50 mg/s showed that Ti<sub>2</sub>AlC has an excellent oxidation resistance. To fully understand the oxidation behavior, both surface and cross sectional views of the scale formed on Ti<sub>2</sub>AlC were investigated in a field-emission scanning-electron microscope equipped with an energy dispersive spectroscopy (EDS) system.

**Figure 5.3** (a), (b), and (c) shows SEM BSE surface images of the Ti<sub>2</sub>AlC samples oxidized at different temperatures in the flowing steam at 50 mg/s. At 600°C and 800°C, a very thin oxide scale (<1 μm) formed on the surface. The surface morphologies and oxidation products formed on Ti<sub>2</sub>AlC changed with temperature. After oxidation at 600°C for 37 h (**Figure 5.3** a), scattered and small size gray spots formed on the surface of Ti<sub>2</sub>AlC, which were analyzed by EDS to be mainly Al and O presumably present as Al<sub>2</sub>O<sub>3</sub>. Meanwhile, the more continuous scale formed on the surface was composed of a higher concentration of Ti and O, which is most likely present as TiO<sub>2</sub>. This suggests that

the oxidation products during oxidation of  $\text{Ti}_2\text{AlC}$  at  $600^\circ\text{C}$  are mainly  $\text{TiO}_2$  and  $\text{Al}_2\text{O}_3$  with  $\text{TiO}_2$  being the dominant oxidation product. After oxidation at  $800^\circ\text{C}$  for 30 h (**Figure 5.3b**), EDS analysis indicated that the concentration of Al and O increased on the surface while the concentration of Ti decreased. Both  $\text{TiO}_2$  and  $\text{Al}_2\text{O}_3$ -rich areas existed simultaneously on the surface. After oxidation at  $1000^\circ\text{C}$  for 15 h (**Figure 5.3c**), the concentration of Al and O further increased to indicate that  $\text{Al}_2\text{O}_3$  had eventually become the dominant phase. This clearly shows the transition of the oxide scale from outer rich  $\text{TiO}_2$  layer to mostly  $\text{Al}_2\text{O}_3$  as the temperature increased from 600 to  $1000^\circ\text{C}$ .

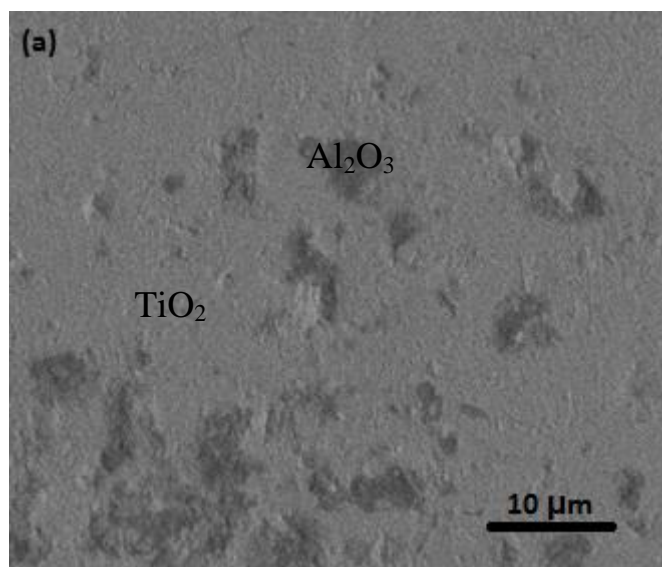


**Figure 5.3.** SEM BSE micrographs showing surface morphology of  $\text{Ti}_2\text{AlC}$  samples oxidized in steam at: (a)  $600^\circ\text{C}$ , (b)  $800^\circ\text{C}$ , and (c)  $1000^\circ\text{C}$ .

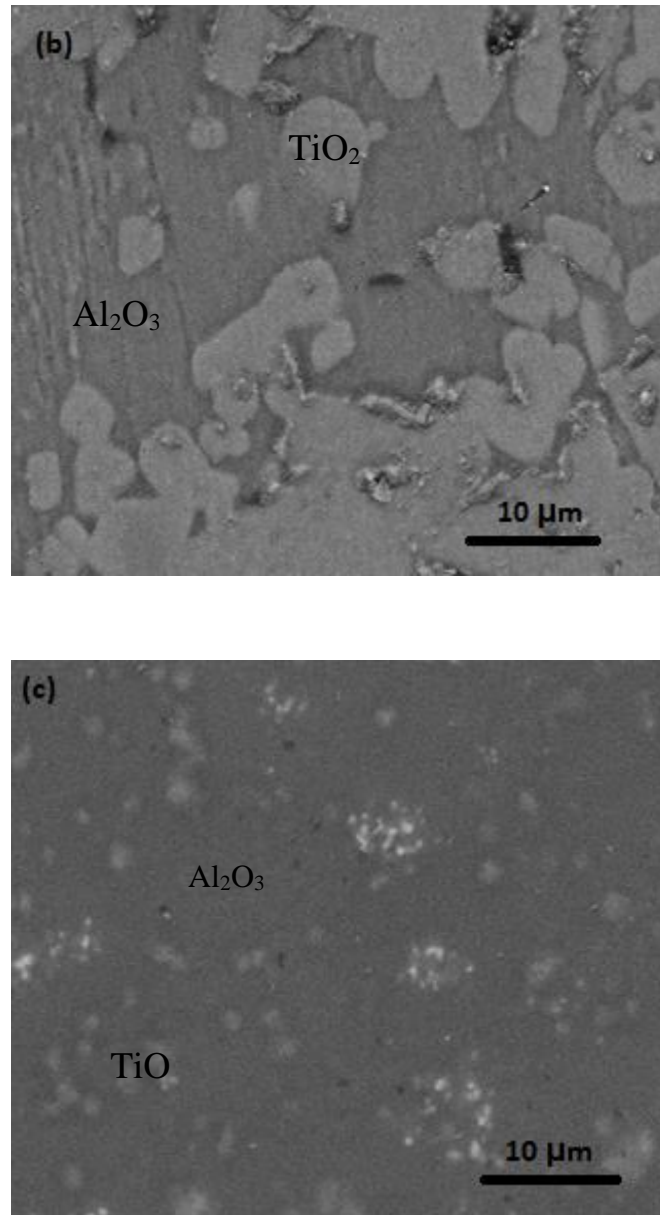


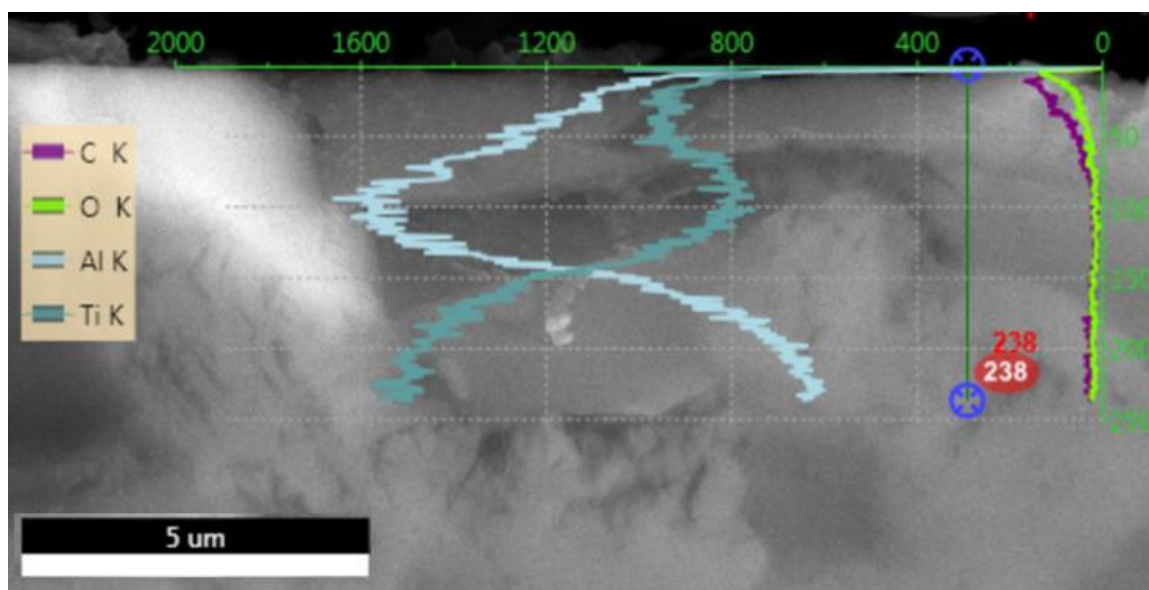
**Figure 5.3** (Continued)

**Figure 5.4-5.6** show SEM images of the cross-sectional views and the corresponding EDS line-scanning profiles of  $\text{Ti}_2\text{AlC}$  samples oxidized at 600, 800, and 1000°C, respectively.

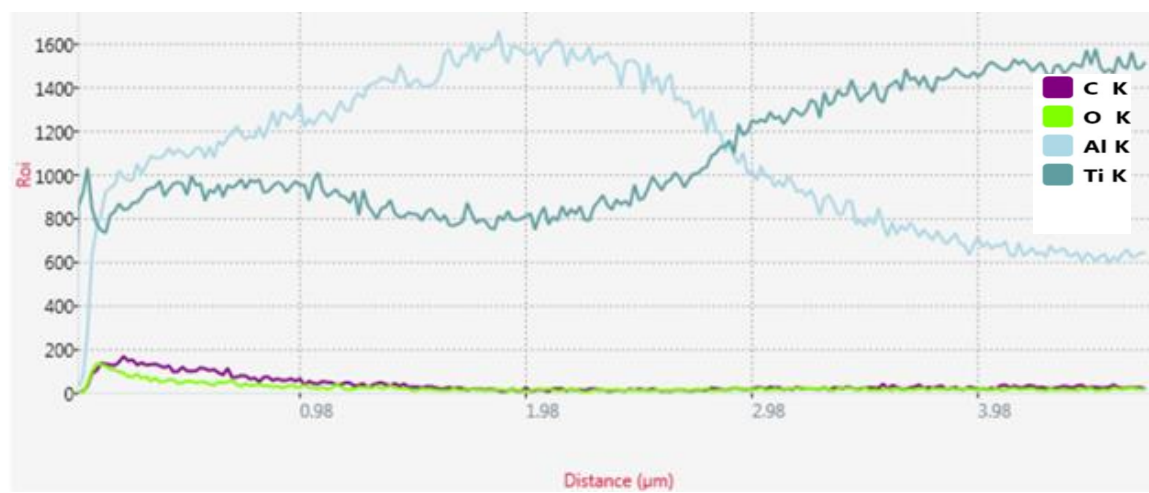
After oxidation at 600°C (**Figure 5.4**), the results obtained from the line-scanning profiles along the green line indicate formation of a very thin oxide scale (less than 1  $\mu\text{m}$ ) on the  $\text{Ti}_2\text{AlC}$  surface. The peaks of Ti and O concentrations are clearly seen in the oxide scale close to the surface, indicating formation of  $\text{TiO}_2$  as a dominant outer-most oxide layer. However, the peak of Al concentration is observed throughout the oxide scale and it has a lesser intensity than Ti on the surface, indicating formation of an inner continuous layer of  $\text{Al}_2\text{O}_3$  beneath the thin  $\text{TiO}_2$  layer at this temperature.

After oxidation at 800°C (**Figure 5.5**), a thin oxide scale ( $\sim 1\mu\text{m}$ ) was formed on the surface of  $\text{Ti}_2\text{AlC}$ . The EDS analysis of the line-scan made across the oxide cross-section indicates that the peak of Al concentration increased compared to the peak of Ti concentration near the oxide surface. This is in good agreement with the results obtained from the surface observation (**Figure 5.3b**), which suggests formation of continuous  $\text{Al}_2\text{O}_3$  and  $\text{TiO}_2$ -rich areas simultaneously on the surface.

After oxidation at 1000°C (**Figure 5.6**), the peaks of Al and O concentrations significantly increased at the outer-most layer of the oxide scale as indicated by the EDS line-scan made along the green line across the oxide scale. Meanwhile, the peak of Ti concentration decreased in a direction away from the unoxidized  $\text{Ti}_2\text{AlC}$  towards the oxide scale surface, resulting in a very small peak of Ti concentration near the oxide surface. This suggests formation of a more continuous  $\text{Al}_2\text{O}_3$  layer on the surface and a discontinuous layer of  $\text{TiO}_2$  near the oxide surface.

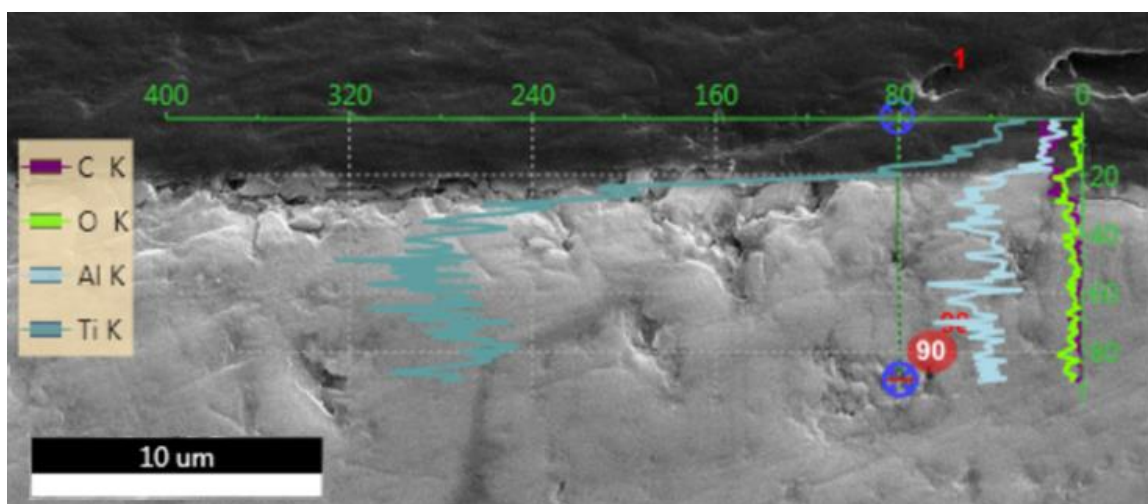


(a)

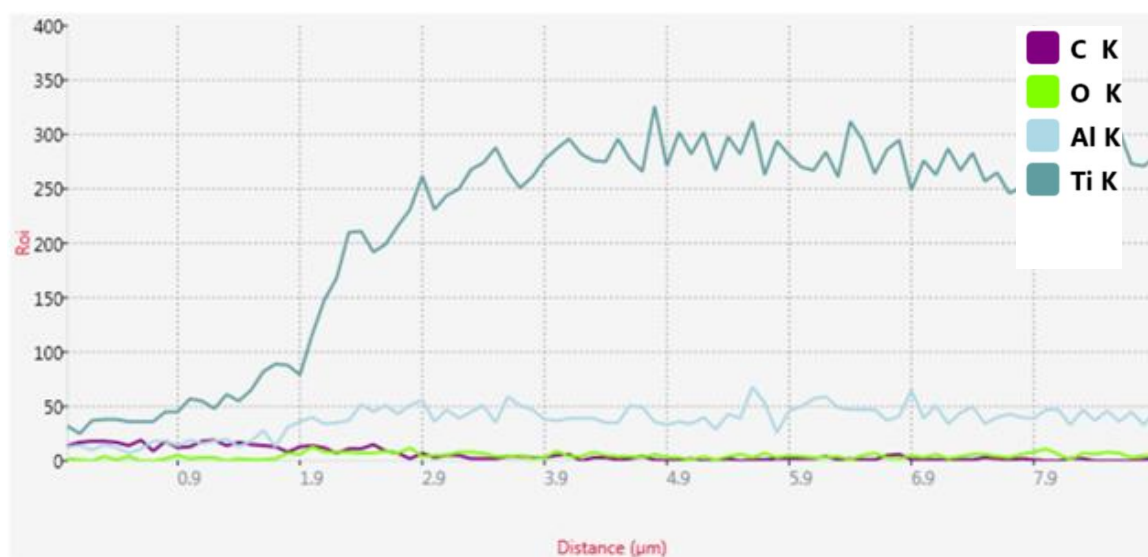


(b)

**Figure 5.4.** (a) SEM BSE image of the polished cross-sectional view of  $\text{Ti}_2\text{AlC}$  oxidized at  $600^\circ\text{C}$  in the flowing steam at  $50\text{ mg/s}$  for  $37\text{ h}$ ; (b) a EDS line scan results along the green line as shown in (a)

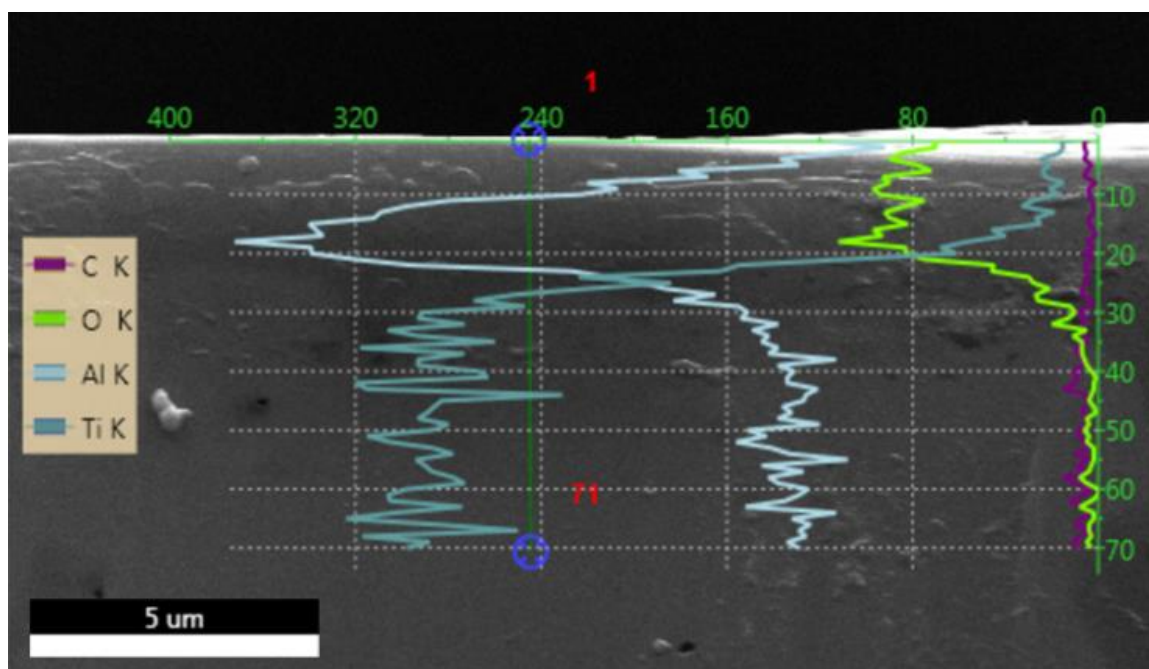


(a)

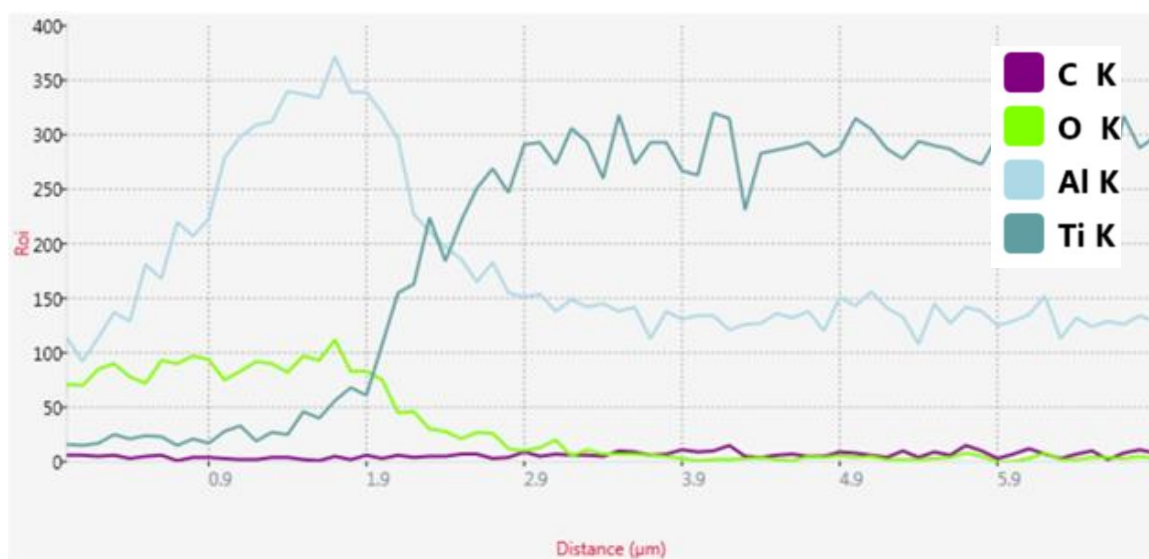


(b)

**Figure 5.5.** (a) SEM BSE image of the polished cross-sectional view of  $\text{Ti}_2\text{AlC}$  oxidized at  $800^\circ\text{C}$  in the flowing steam at  $50\text{ mg/s}$  for  $30\text{ h}$ ; (b) a EDS line scan results along the green line as shown in (a)



(a)



(b)

**Figure 5.6.** (a) SEM BSE image of the FIB exposed cross-sectional view of  $\text{Ti}_2\text{AlC}$  oxidized at  $1000^\circ\text{C}$  in the flowing steam at  $50\text{ mg/s}$  for  $15\text{ h}$ ; (b) a EDS line scan results along the green line as shown in (a)

At all investigated temperatures, the oxide scale formed on  $\text{Ti}_2\text{AlC}$  was free from cracks and cavities, and it was very adhesive to the substrate. This is clearly obvious in **Figure 5.7** (a), (b), and (c), which reveal the high magnification cross-sectional views of  $\text{Ti}_2\text{AlC}$  samples oxidized in steam at 600, 800, and 1000°C, respectively. Although the thickness of the oxide scale didn't exceed 1  $\mu\text{m}$  for  $\text{Ti}_2\text{AlC}$  samples oxidized at 600 and 800°C, a relatively very thick (2-3  $\mu\text{m}$ ) scale formed after oxidation at 1000°C.

From the EDS results (**Figure 5.4-5.6**), it can be concluded that oxygen has a low solubility and diffusivity in  $\text{Ti}_2\text{AlC}$  at all investigated temperatures. This makes the external oxidation more favorable. The excellent adhesion of the oxide scale to the substrate can be associated with the negligible difference in the density and thermal expansion coefficient between the oxides and  $\text{Ti}_2\text{AlC}$  substrate. The densities of  $\text{Al}_2\text{O}_3$  and  $\text{Ti}_2\text{AlC}$  are 4.21 and 3.98  $\text{g}/\text{cm}^3$ , respectively [71], which is believed to have caused a little change in volume during the formation of the oxide scale and resulted in a good adhesion between the oxide scale and substrate.

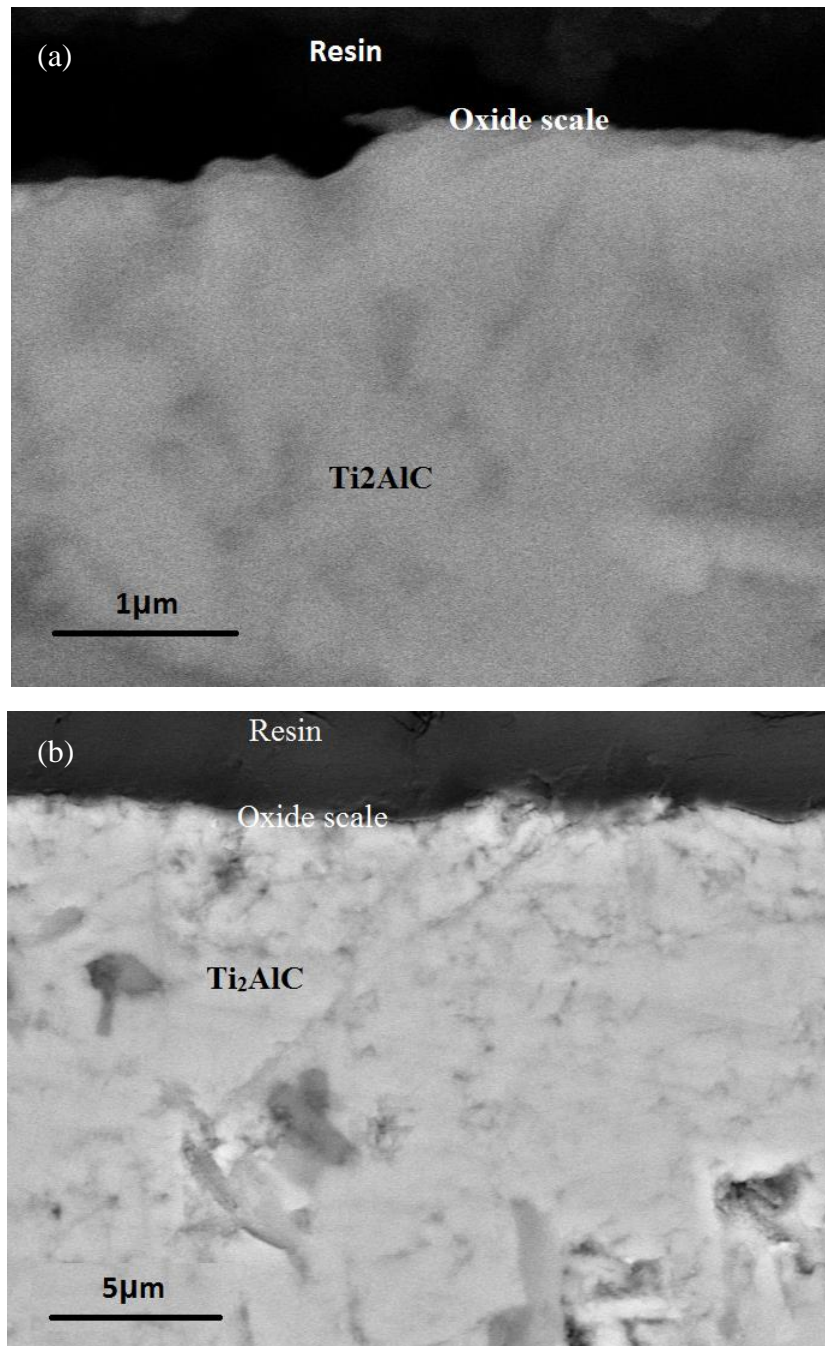


**Figure 5.7.** SEM BSE micrograph showing the cross section of the oxide scale formed on  $\text{Ti}_2\text{AlC}$  after oxidation in steam at (a)  $600^\circ\text{C}$  for 37 h, (b)  $800^\circ\text{C}$  for 30 h, and (c)  $1000^\circ\text{C}$  for 15 h.

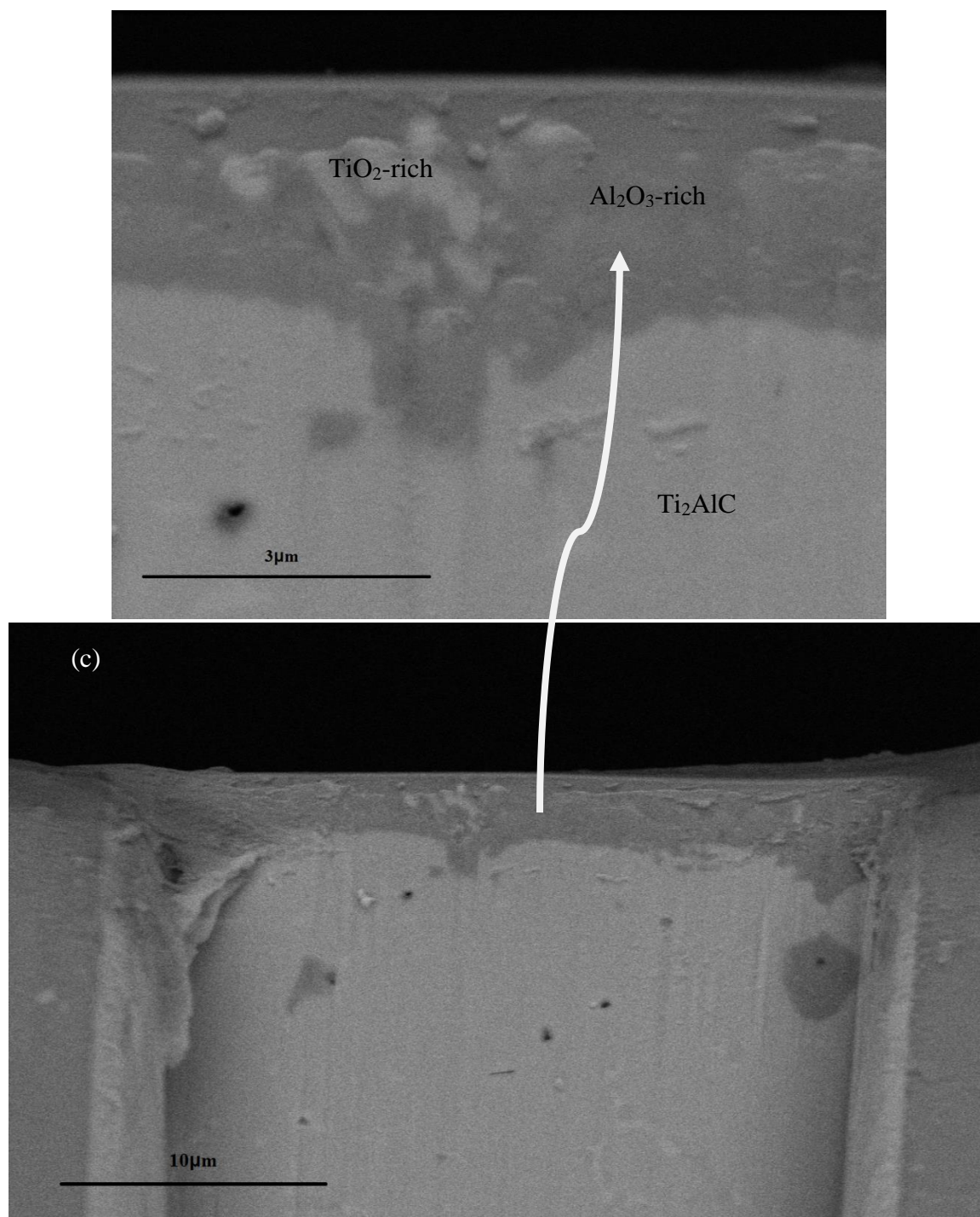


Figure 5.7 (continued)

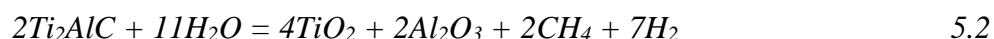
### 5.1.3. Oxidation Mechanism

In general, the oxidation of  $\text{Ti}_2\text{AlC}$  is diffusion controlled. The proposed mechanism for the growth of the oxide scale on  $\text{Ti}_2\text{AlC}$  is explained by the inward diffusion of the  $\text{O}^{2-}$  and the outward diffusion of  $\text{Al}^{+3}$  and  $\text{Ti}^{4+}$  [71, 114]. The oxide scale formed on  $\text{Ti}_2\text{AlC}$  is composed of an inner continuous layer of  $\text{Al}_2\text{O}_3$  and an outer discontinuous layer of  $\text{TiO}_2$ . According to many researchers,  $\text{Al}_2\text{O}_3$  layer has a very good adhesion to the substrate. The combination of a continuous  $\text{Al}_2\text{O}_3$  layer on  $\text{Ti}_2\text{AlC}$  and its good adhesion to the substrate are promising indications for the excellent oxidation resistance of  $\text{Ti}_2\text{AlC}$  [71].

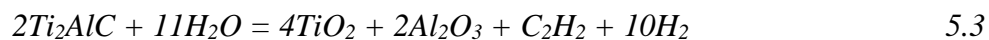
At all investigated temperatures,  $\text{TiO}_2$  and  $\text{Al}_2\text{O}_3$  are formed on the surface of  $\text{Ti}_2\text{AlC}$  by the inward diffusion of  $\text{O}^{2-}$  and the outward diffusion of  $\text{Al}^{+3}$  and  $\text{Ti}^{4+}$ . During the initial stage of the oxidation of  $\text{Ti}_2\text{AlC}$ , both  $\text{TiO}_2$  and  $\text{Al}_2\text{O}_3$  nucleate and grow on the surface simultaneously [71]. When the oxide scale is more stable and the oxygen partial pressure at the oxide/substrate-interface is low enough,  $\text{Al}_2\text{O}_3$  is more likely to form because it needs a much lower oxygen partial pressure than  $\text{TiO}_2$  to form [80]. Additionally,  $\text{Al}_2\text{O}_3$  is thermodynamically more stable than  $\text{TiO}_2$  [114] and Al is more weakly bound in the structure of  $\text{Ti}_2\text{AlC}$  than Ti [115, 116]. As a result,  $\text{Al}_2\text{O}_3$  continues to grow. At the early stages of oxidation, especially when the temperature is relatively low,  $\text{Ti}^{4+}$  is diffused through the grain boundaries of  $\text{Al}_2\text{O}_3$  to form a discontinuous layer on the surface. As the oxidation temperature is increased, the outward diffusion of  $\text{Al}^{3+}$  is also increased. This is also evident in the surface morphologies illustrated in **Figure 5.3**. Once  $\text{Al}_2\text{O}_3$  is more stable, the diffusion of  $\text{Ti}^{4+}$  through  $\text{Al}_2\text{O}_3$  layer is slowed down due

to the low diffusivity of Ti in  $Al_2O_3$ , yielding a dominant layer of  $Al_2O_3$  and resulting in an excellent oxidation resistance.

The chemical reactions involved in the oxidation of  $Ti_2AlC$  in steam and formation of the oxide scale can be written as follows [83]:



Or



It is noted from the above chemical reactions that the oxidation of  $Ti_2AlC$  in steam is accompanied by generation of hydrogen, which could play a significant role in the oxidation of  $Ti_2AlC$  as the amount of hydrogen is increased in the atmosphere [83]. More facts about this effect are discussed in section 5.2.

Additionally, the thin layer of  $TiO_2$ , pushed to the surface during oxidation process of  $Ti_2AlC$ , was further reacted with steam as the temperature was increased according to the following reaction [89]:



Equation 5.4 could provide a reasonable explanation for the reduced amount of  $\text{TiO}_2$  on the surface of  $\text{Ti}_2\text{AlC}$ , which was observed in **Figure 5.3** as the temperature was increased from 600 to 1000°C. Based on the same chemical equation, Basu et al. [80] attributed the diminishing of  $\text{TiO}_2$  to the formation of gaseous  $\text{TiO}(\text{OH})_2$ , which volatilizes the thin  $\text{TiO}_2$  layer in the oxide scale on  $\text{Ti}_2\text{AlC}$  at high temperatures. This is most possibly the case in the current study.

## 5.2. Effect of Steam Flow Rate on the Oxidation Behavior of $Ti_2AlC$ at Different Temperatures

When the average flow rate of the steam was increased from 50 mg/s to 100 mg/s, the oxidation kinetics increased considerably. **Figure 5.8** depicts the difference in oxidation kinetics between  $Ti_2AlC$  samples oxidized at 50 mg/s and those oxidized at 100 mg/s at 600, 800 and 1000°C.

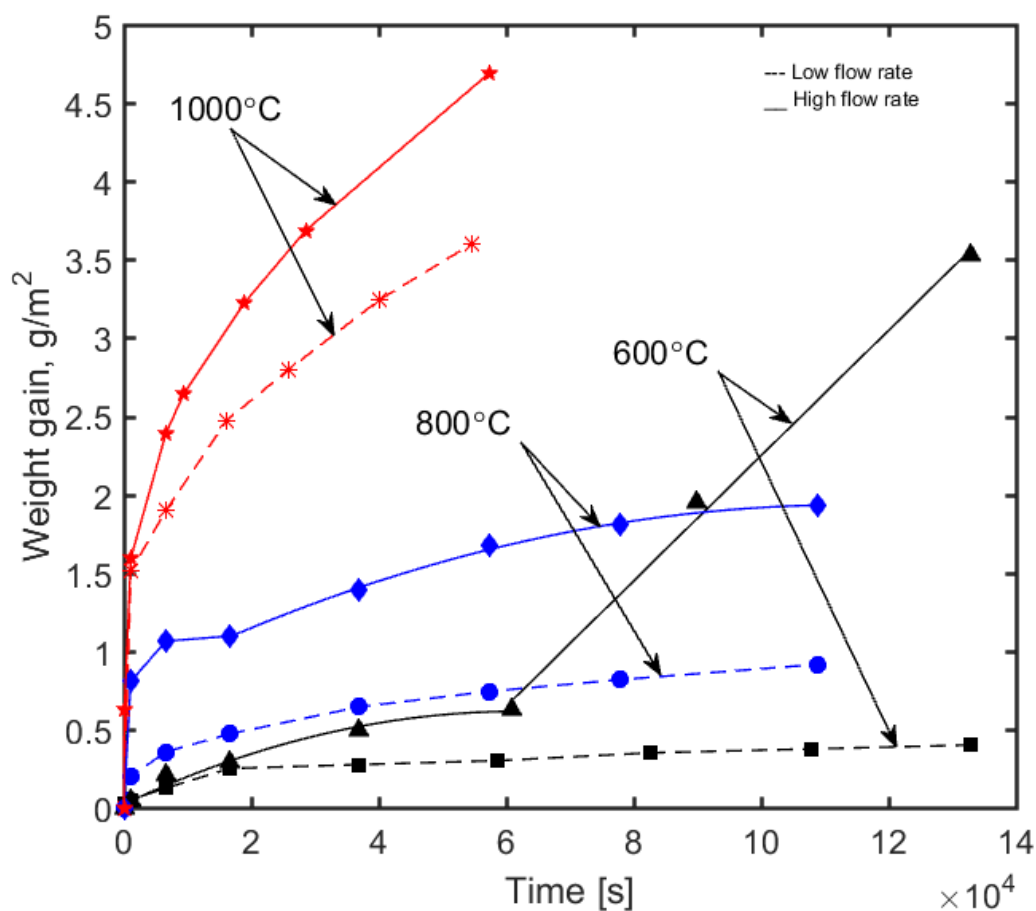


**Figure 5.8.** Oxidation kinetics of  $Ti_2AlC$  oxidized in flowing steam at 50 mg/s (dashed lines) and 100 mg/s (solid lines).

Although the oxidation kinetics maintained a parabolic rate law at 600 and 800°C and a cubic rate law at 1000°C during the oxidation in the flowing steam at 100 mg/s, the breakaway phenomenon was observed after 17 hours of oxidation at 600°C. This suggests that increasing the amount of steam greatly accelerates the oxidation kinetics of Ti<sub>2</sub>AlC at 600°C. Similar results have been reported by several researchers from the oxidation experiments of Ti<sub>2</sub>AlC at this temperature in both dry air and water vapor. Wang and Zhou [75] observed this phenomenon during oxidation of Ti<sub>2</sub>AlC in air at temperatures of 500 and 600°C. They attributed this anomalous behavior to the initiation of cracks in the oxide scales. In a separate study [83], Z. J. Lin et al. also reported that the oxidation kinetics of Ti<sub>2</sub>AlC oxidized in the presence of water vapor at 600°C followed a parabolic rate law for a couple of hours before a linear oxidation with a rapid mass gain was seen. Yet, this anomalous behavior is not fully understood and requires more investigation.

After the kinetics transition at 600°C, the oxidation kinetics did not obey a parabolic rate law indicating that the oxidation rate was no longer controlled by oxygen diffusion through the oxide scale. The post-transition kinetics was analyzed by plotting the weight gain per unit surface area as a function of time, which resulted in a straight line as an indication of obeying a linear kinetics rate law. Moreover, the kinetics rate constants for samples oxidized at 800 and 1000°C increased by approximately one order of magnitude when the average flow rate of steam was increased from 50 mg/s to 100 mg/s. **Table 5.2** reveals the difference in oxidation rate constants for the Ti<sub>2</sub>AlC samples oxidized in steam at different flow rates for each temperature.

Temperature T(°C)	Kinetics Rate Constant	
	Steam (50 mg/s)	Steam (100 mg/s)
600	$k_P = 8.7 \times 10^{-7} \text{ g}^2 \cdot \text{m}^{-4} \cdot \text{s}^{-1}$	$k_P = 6.4 \times 10^{-6} \text{ g}^2 \cdot \text{m}^{-4} \cdot \text{s}^{-1}$ $k_L = 4.0 \times 10^{-5} \text{ g} \cdot \text{m}^{-2} \cdot \text{s}^{-1}$
800	$k_P = 6.5 \times 10^{-6} \text{ g}^2 \cdot \text{m}^{-4} \cdot \text{s}^{-1}$	$k_P = 6.6 \times 10^{-5} \text{ g}^2 \cdot \text{m}^{-4} \cdot \text{s}^{-1}$
1000	$k_C = 8.1 \times 10^{-4} \text{ g}^3 \cdot \text{m}^{-6} \cdot \text{s}^{-1}$	$k_C = 1.8 \times 10^{-3} \text{ g}^3 \cdot \text{m}^{-6} \cdot \text{s}^{-1}$

**Table 5.2.** Comparison between kinetics rate constants at different flow rates of steam.

To better understand the variation in oxidation kinetics at different averages of the steam flow rate, SEM observation of the surface and cross sectional views were conducted. Meanwhile, the polished cross section of Ti<sub>2</sub>AlC was analyzed by EDS to investigate the microstructure of the oxide scale. The SEM images of Ti<sub>2</sub>AlC samples oxidized at all temperatures in steam reveal a densely compact scale on the surface except for those oxidized at 600°C for 37 hours. **Figure 5.9** (a) and (b) shows the difference in oxide microstructures formed after the oxidation of Ti<sub>2</sub>AlC at 600°C in the flowing steam at 50 mg/s and 100 mg/s, respectively. The white arrows in **Figure 5.9** (a) indicate the locations of possible cracks initiated on the surface after oxidation at 600°C for 37 h in the flowing steam at 100 mg/s. These cracks, in addition to the obvious porosity of the scale, generated reduced paths for oxygen into the substrate. This is in good agreement with the results obtained from the kinetics behavior for the Ti<sub>2</sub>AlC sample oxidized at 600°C in steam at 100 mg/s. On the other hand, the sample oxidized in steam at low flow rate (50 mg/s) maintained a very dense oxide scale, free from cracks and cavities.

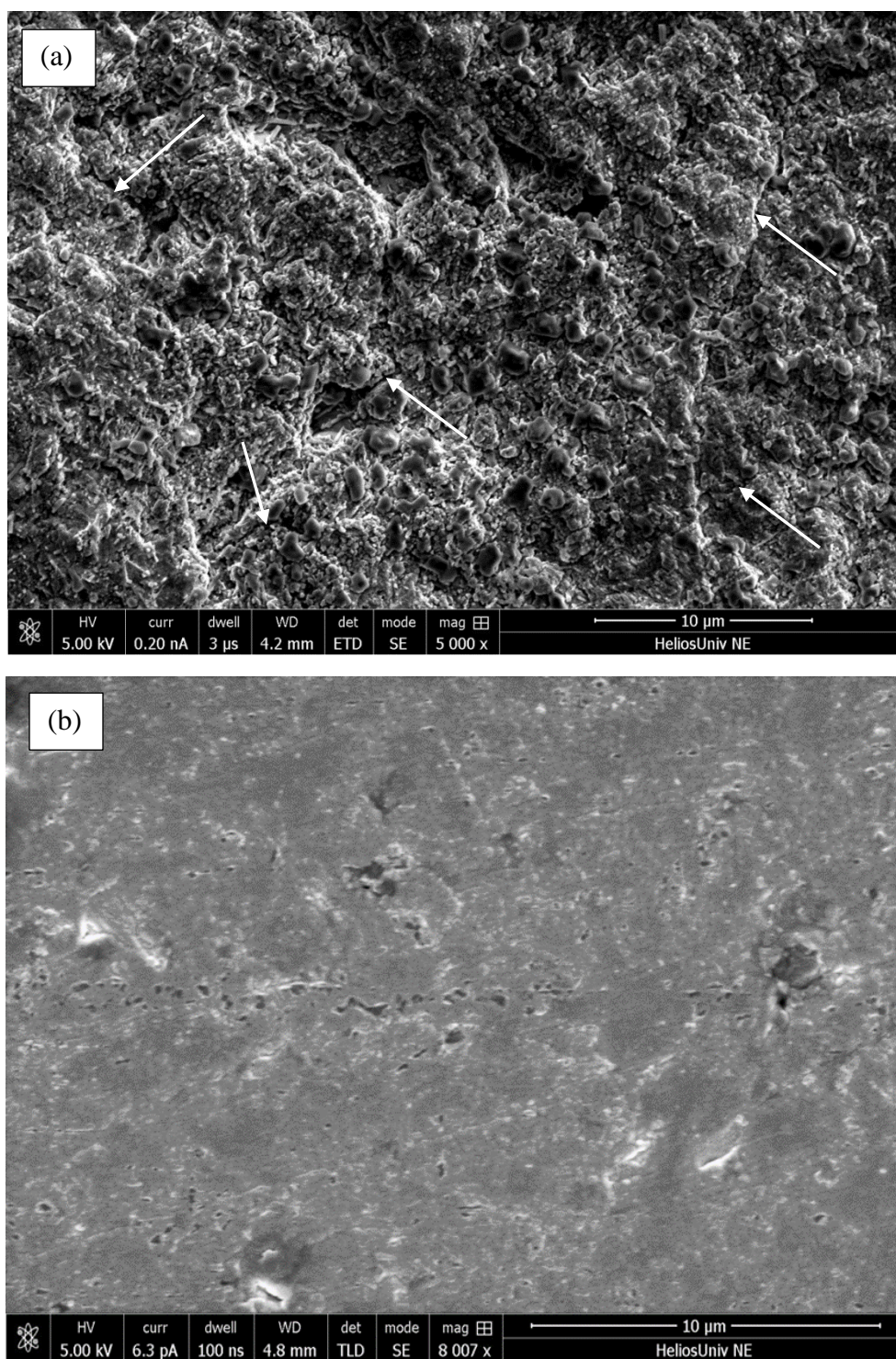


**Figure 5.9.** SEM SE micrographs showing surface morphology of  $\text{Ti}_2\text{AlC}$  oxidized at 600C: (a) High flow rate steam, and (b) low flow rate steam.

**Figure 5.10** (a) and (b) shows the difference in the morphologies of the samples oxidized at 600°C in the flowing steam at 100 mg/s before and after the breakaway oxidation for 10 and 25 hours, respectively. The appearance of the oxide microstructure developed at the post-transition kinetics stage (**Figure 5.10b**) in comparison with the pre-transition stage (**Figure 5.10a**) is highly porous and seemingly non-protective. This microstructural evolution is attributed to the influence of steam flow rate on the oxidation at 600°C, which resulted in the breakaway oxidation. However, the SEM images of the oxide scale formed on the surface of the sample oxidized at 800 and 1000°C (**Figure 5.11**) is very dense and protective. This is associated with the formation of a continuous layer of Al<sub>2</sub>O<sub>3</sub> on the surface.

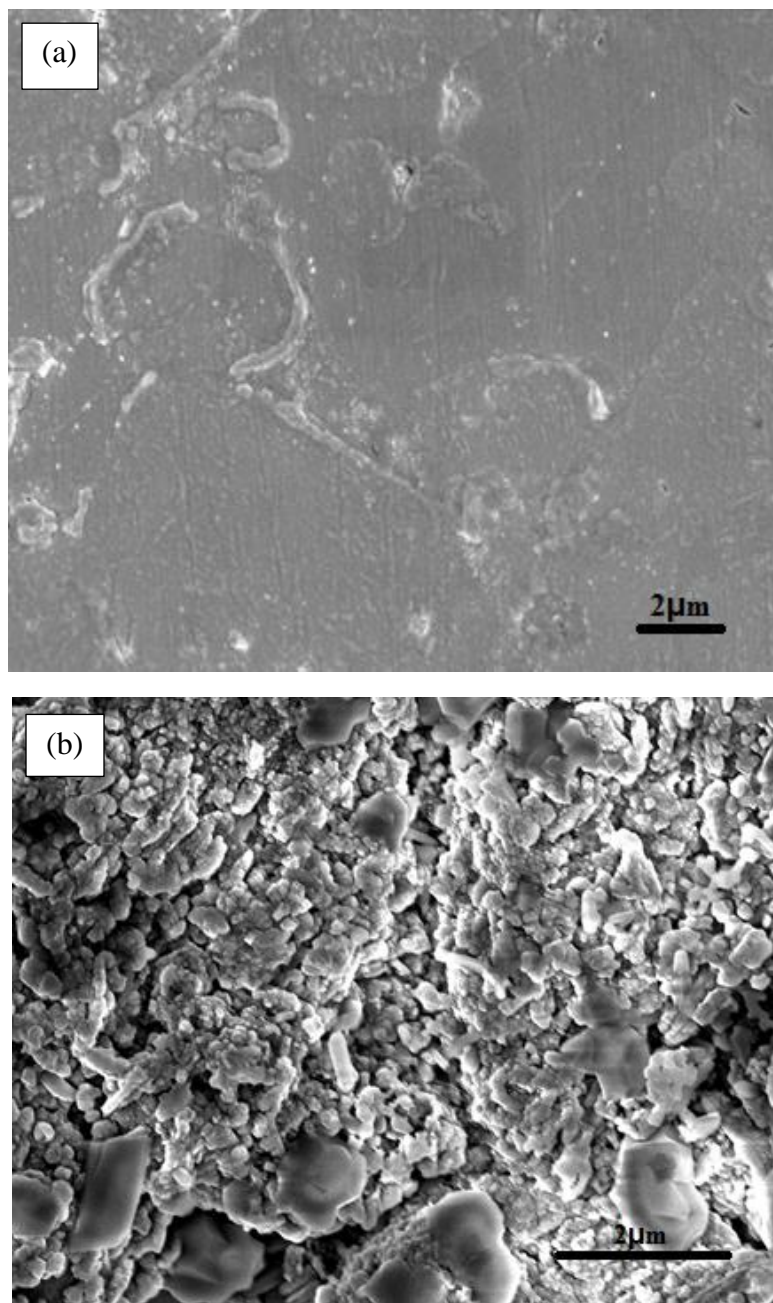


**Figure 5.10.** SEM SE micrographs showing the surface morphology of  $Ti_2AlC$  oxidized at 600°C: (a) Before, and (b) After breakaway.

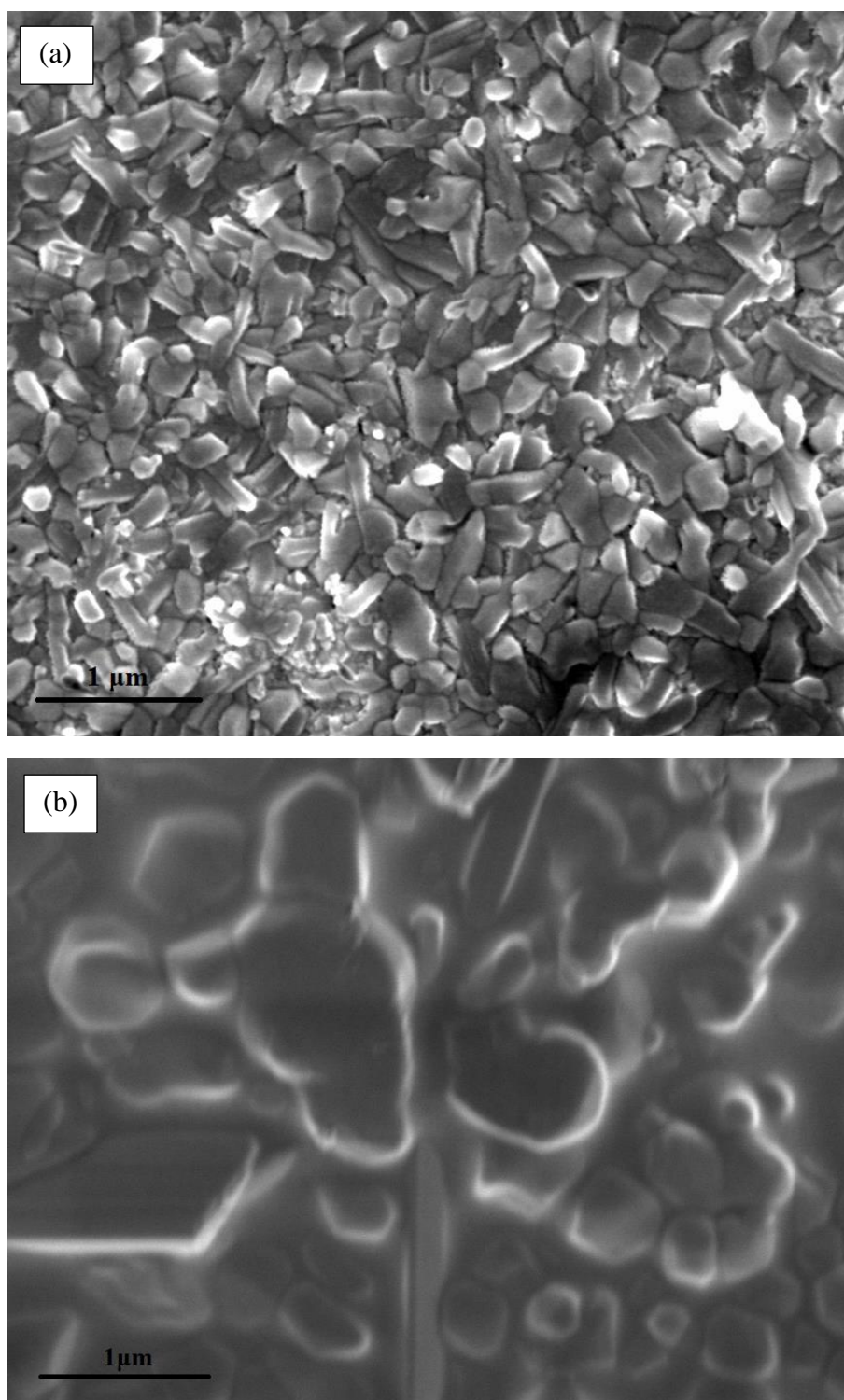


**Figure 5.11.** Typical SEM micrographs of the surface of  $\text{Ti}_2\text{AlC}$  samples oxidized in the flowing steam at 100 mg/s (a) at 800°C, and (b) at 1000°C.

Typical SEM images of the cross-sectional views with the corresponding EDS line-scanning profiles of  $\text{Ti}_2\text{AlC}$  oxidized at 600, 800, and 1000°C in the flowing steam at 100 mg/s are shown in **Figures 5.12-5.14**, respectively. For the sample oxidized at 600°C (**Figure 5.12**), it can be seen that the scale is composed of a mixture of  $\text{TiO}_2$  and  $\text{Al}_2\text{O}_3$  with  $\text{TiO}_2$  being the dominant phase. Dissolution of a small amount of oxygen in  $\text{Ti}_2\text{AlC}$  substrate is also noticeable in the EDS-scanning profiles. However, no cracks are evident within the oxide scale from the SEM cross-sectional view of the sample. For the samples oxidized at 800 and 1000°C, **Figures 5.13** and **5.14**, continuous and protective  $\text{Al}_2\text{O}_3$  oxide scales were observed. This can efficiently protect the  $\text{Ti}_2\text{AlC}$  substrate.

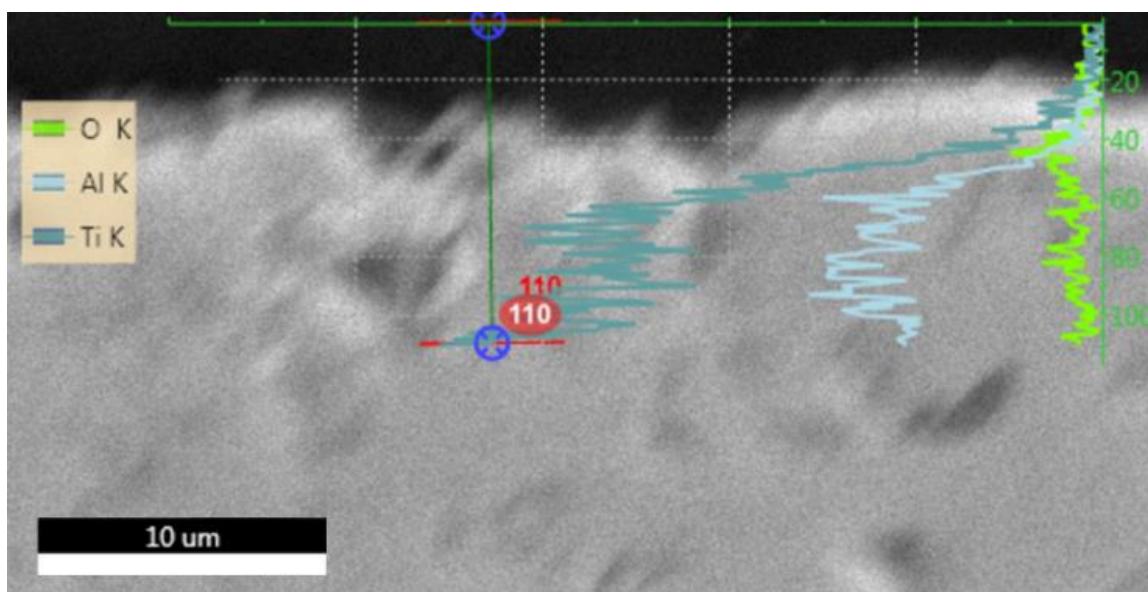
The thickness of the oxide scale formed on  $\text{Ti}_2\text{AlC}$  in the presence of steam increased with the steam flow rate. In comparison with  $\text{Ti}_2\text{AlC}$  samples oxidized in steam at 50 mg/s, the thickness of the oxide was almost doubled for the samples oxidized in steam at 100 mg/s at all investigated temperatures. However, the passivity of the oxide scale remained intact for the samples oxidized at 800 and 1000°C. Porosity and possible cracks, which result in the breakaway oxidation, were observed on the surface of  $\text{Ti}_2\text{AlC}$  oxidized at 600°C. In general, the results obtained from SEM micrographs and EDS analyses are in good agreement with those obtained from the oxidation kinetics. The anomalous oxidation behavior of  $\text{Ti}_2\text{AlC}$  observed at 600°C in the flowing steam at 100 mg/s is most likely related to the amount of  $\text{TiO}_2$  in the oxide scale, which comprised the biggest at 600°C. After oxidation of metallic Ti thin films at low temperatures in dry and wet air, it was found that anatase- $\text{TiO}_2$  only formed during oxidation in wet air [117]. Lin et al. [83] also confirmed the formation of anatase- $\text{TiO}_2$  in addition to a significant amount of rutile with poor crystallinity after oxidation of  $\text{Ti}_2\text{AlC}$  at 600°C in water vapor.

This indicates that anatase-phase  $\text{TiO}_2$  formed firstly during the oxidation of  $\text{Ti}_2\text{AlC}$  in the presence of steam. Since the rutile phase is more stable, anatase transforms to rutile as the oxidation is proceeded. Furthermore, the transformation is enhanced by increasing the amount of water vapor in the atmosphere [83]. This transformation results in a significant difference in volume due to higher density of rutile ( $4.26 \text{ g/cm}^3$ ) than anatase ( $3.84 \text{ g/cm}^3$ ) [116]. As a result, tensile stresses generate in the oxide scale and lead to cracks (**Figure 5.9a**), which provide channels for the transportation of  $\text{H}_2\text{O}$  into the scale and increase the oxidation rate.

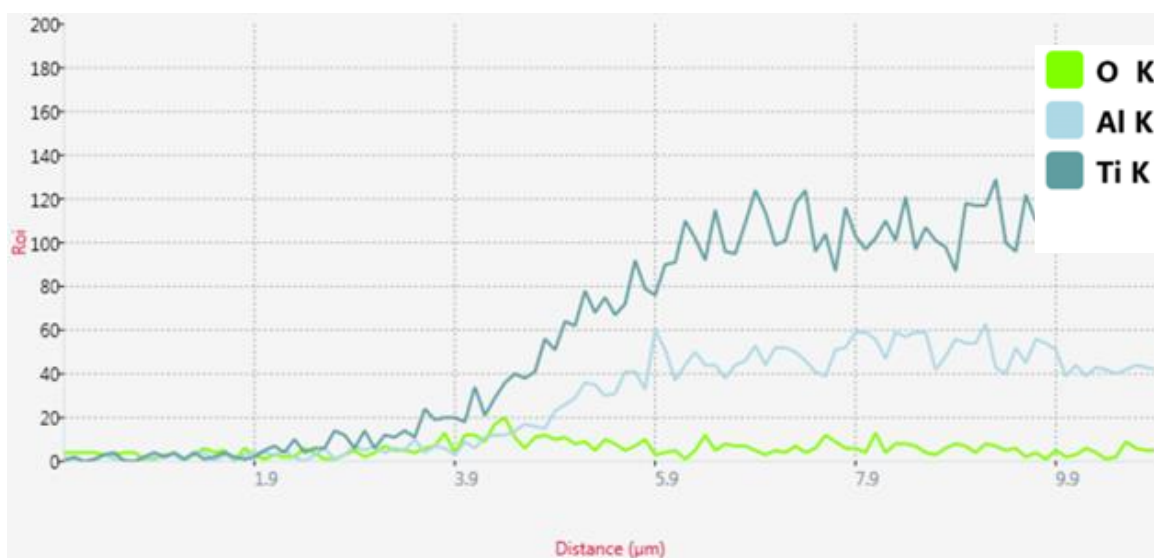
The oxygen transport in materials is primarily controlled by the number of oxygen vacancies, which can be described as follows [83]:

$$O_o^x = V_{\bar{O}} + 2e + 1/2O_2 \quad 5.5$$

Meanwhile, hydrogen generated during the reactions between  $\text{Ti}_2\text{AlC}$  and steam (Eq 5.2 and Eq 5.3) can facilitate Eq. 5.5, and increase the density of oxygen vacancies ( $V_{\bar{O}}$ ). Consequently, the inward diffusion of oxygen is increased.

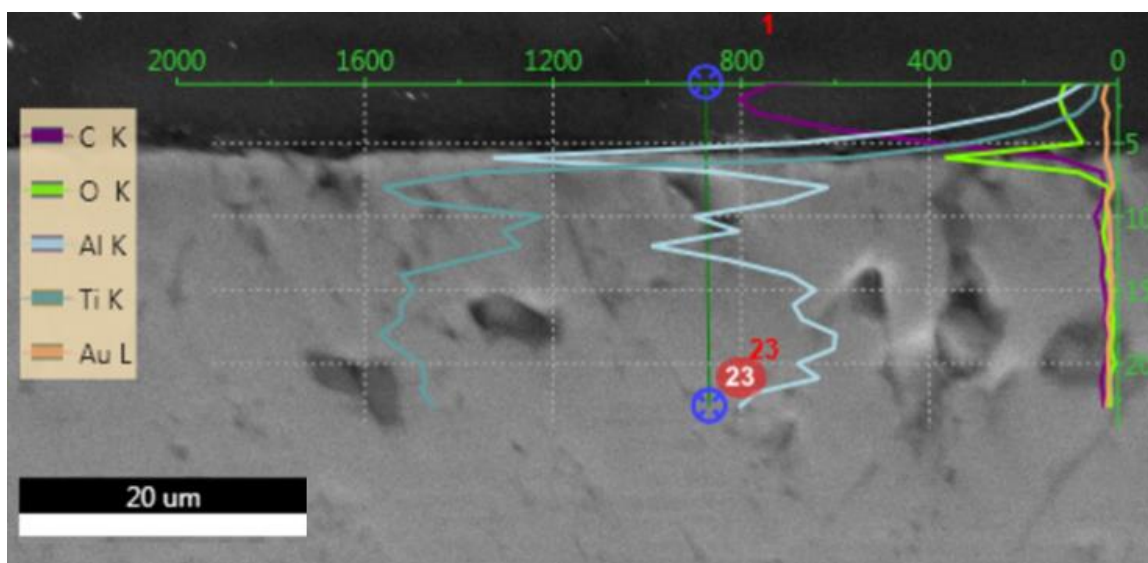


(a)

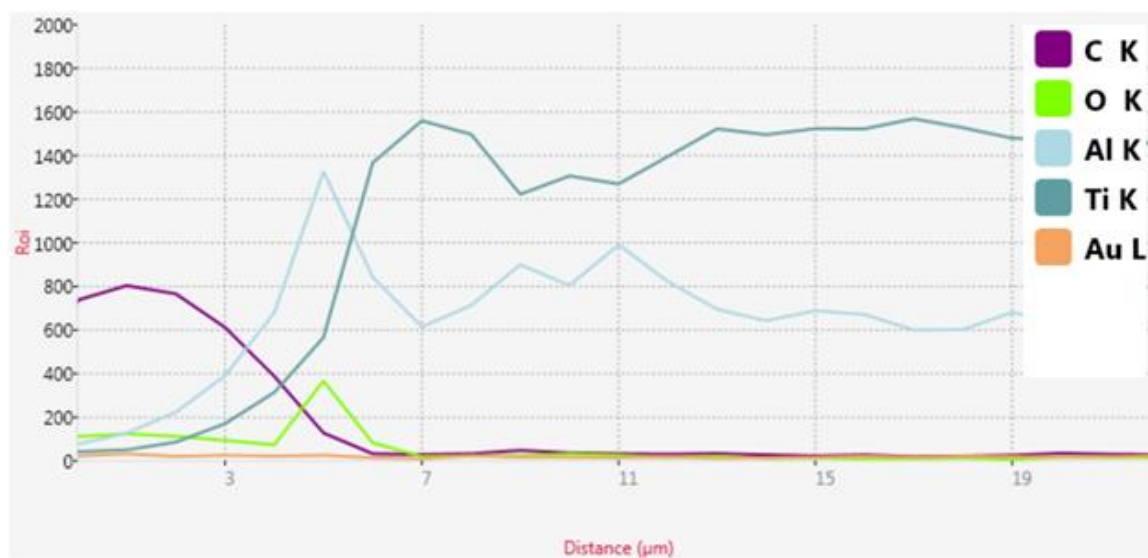


(b)

**Figure 5.12.** (a) SEM image of the polished cross-sectional view of  $\text{Ti}_2\text{AlC}$  oxidized at  $600^\circ\text{C}$  in the flowing steam at  $100\text{ mg/s}$  for  $37\text{ h}$ ; (b) EDS line scan results along the green line as shown in (a).

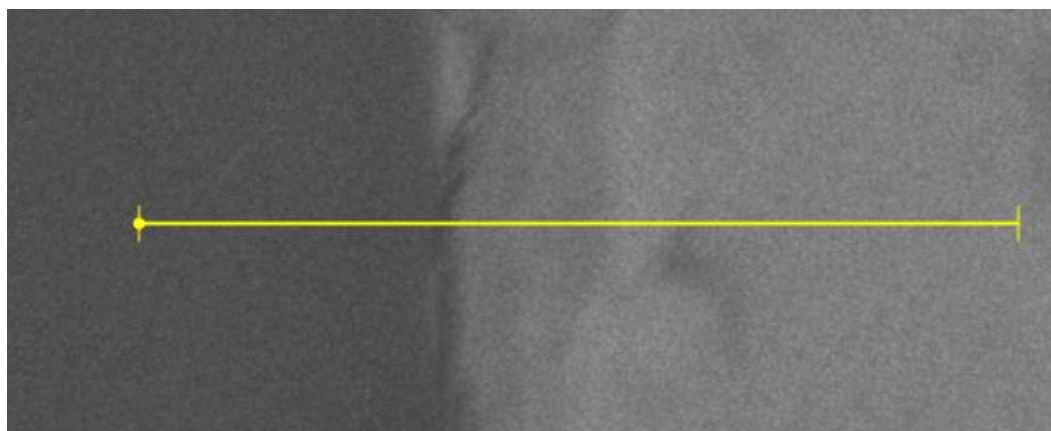


(a)

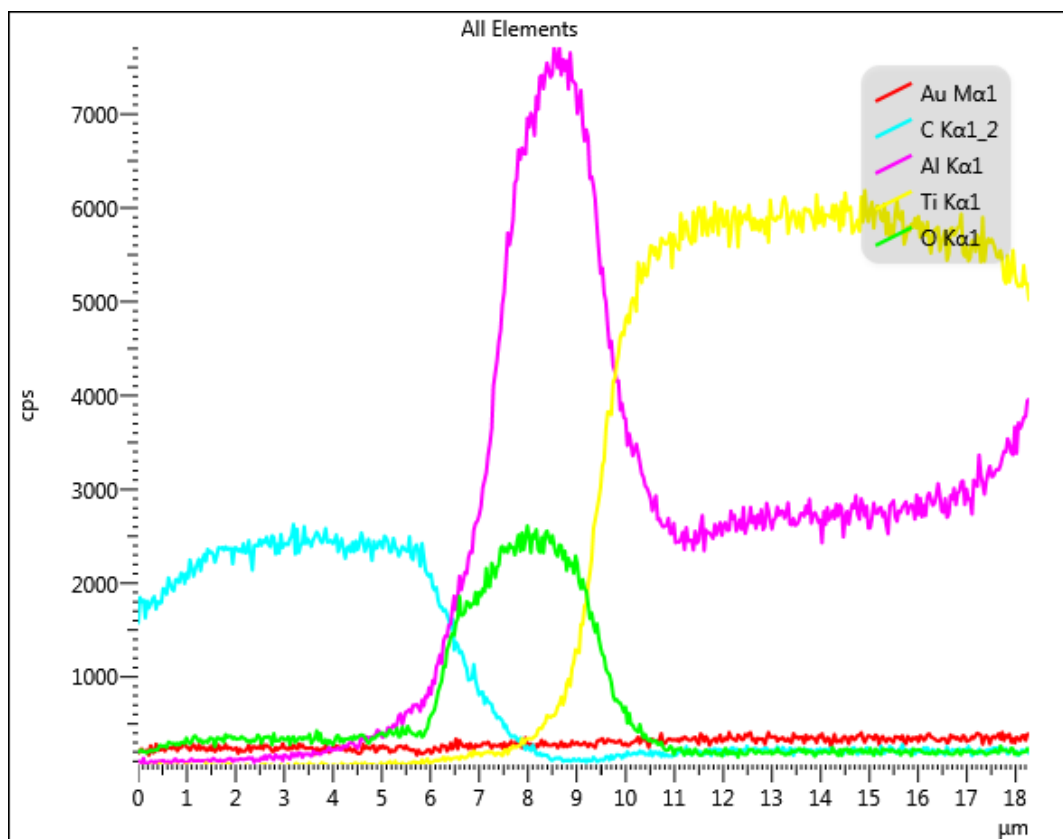


(b)

**Figure 5.13.** (a) SEM image of the polished cross-sectional view of  $\text{Ti}_2\text{AlC}$  oxidized at  $800^\circ\text{C}$  in the flowing steam at  $100\text{ mg/s}$  for  $30\text{ h}$ ; (b) EDS line scan results along the green line as shown in (a).



(a)



(b)

**Figure 5.14.** (a) SEM image of the polished cross-sectional view of  $\text{Ti}_2\text{AlC}$  oxidized at  $1000^\circ\text{C}$  in the flowing steam at  $100\text{ mg/s}$  for  $15\text{ h}$ ; (b) EDS line scan results along the green line as shown in (a).

In this research study, it is postulated that the breakaway oxidation of  $Ti_2AlC$  at  $600^\circ C$  is accounted for by involving the phase transformation of  $TiO_2$ , which is accelerated by increasing steam content in the atmosphere. Although it is significantly affected by the presence of impurities, the transformation of  $TiO_2$  from anatase to rutile phase starts at  $\sim 600^\circ C$  [118]. One of the mechanisms through which this transformation takes place is oxygen vacancies, which are increased in the presence of hydrogen [83, 119]. This is associated with the fact that oxygen vacancies facilitate the rearrangement of ions [118]. Since both expected chemical reactions between  $Ti_2AlC$  and water vapor generate hydrogen (Eq. 5.2 & 5.3) [83], it is not surprising that water vapor accelerates the transformation of  $TiO_2$  from anatase to rutile phase. According to the EDS results obtained from the oxidation of  $Ti_2AlC$  in steam at all investigated temperatures, the highest concentration of  $TiO_2$  is detected at  $\sim 600^\circ C$ . As a result, the biggest change in volume due to the difference in densities between anatase and rutile occurs at  $600^\circ C$  and leads to the initiation of porosities and cracks.

### 5.3. Comparison of the Oxidation Kinetics of Zircaloy-2 (Zry-2) and Ti<sub>2</sub>AlC

**Figure 5.15** compares the oxidation kinetics of Ti<sub>2</sub>AlC with the oxidation kinetics of Zry-2. Oxidation kinetics, represented by the weight gain per unit surface area versus time, is a clear visual indication for the detrimental effect of high temperature oxidation on Zircaloy-2 in comparison with Ti<sub>2</sub>AlC. Among all oxidation experiments, Ti<sub>2</sub>AlC only showed a breakaway oxidation at 600°C in steam at the flow rate of 100 mg/s after oxidation for 17 h. In contrast, Zry-2 experienced this phenomenon at all investigated conditions. Since the high flow rate steam (100 mg/s) significantly accelerates the oxidation rate of Ti<sub>2</sub>AlC, only the results obtained from these experiments are considered for this comparison. At 600°C (**Figure 5.15a**), both materials initially followed a parabolic rate law. However, the kinetics rate constant obtained from the oxidation of Zry-2 ( $5.7 \times 10^{-4} \text{ g}^2 \cdot \text{m}^{-4} \cdot \text{s}^{-1}$ ) was almost two orders of magnitude higher than that for the oxidation of Ti<sub>2</sub>AlC ( $6.4 \times 10^{-6} \text{ g}^2 \cdot \text{m}^{-4} \cdot \text{s}^{-1}$ ) with a coefficient of determination  $R^2=0.99$ . The post-transition linear rate constant for Ti<sub>2</sub>AlC was  $4.0 \times 10^{-5} \text{ g} \cdot \text{m}^{-2} \cdot \text{s}^{-1}$  while the post-transition linear rate constant for Zry-2 was  $1.3 \times 10^{-4} \text{ g} \cdot \text{m}^{-2} \cdot \text{s}^{-1}$ . This is a significantly high variation, and the effect is clearly observed in the SEM images of the microstructural views, discussed in the previous sections. At 800 and 1000°C (**Figure 5.15a and b**), Ti<sub>2</sub>AlC displayed a very small change in mass in comparison with the mass

gain for Zry-2. The oxidation kinetics followed a parabolic rate law for the  $\text{Ti}_2\text{AlC}$  sample oxidized at  $800^\circ\text{C}$  and a cubic rate law for the one oxidized at  $1000^\circ\text{C}$  throughout the oxidation process and no breakaway was observed. This is clearly incomparable to the oxidation behavior of Zry-2 which showed a faster breakaway oxidation as the temperature was increased ( $>600$ ).

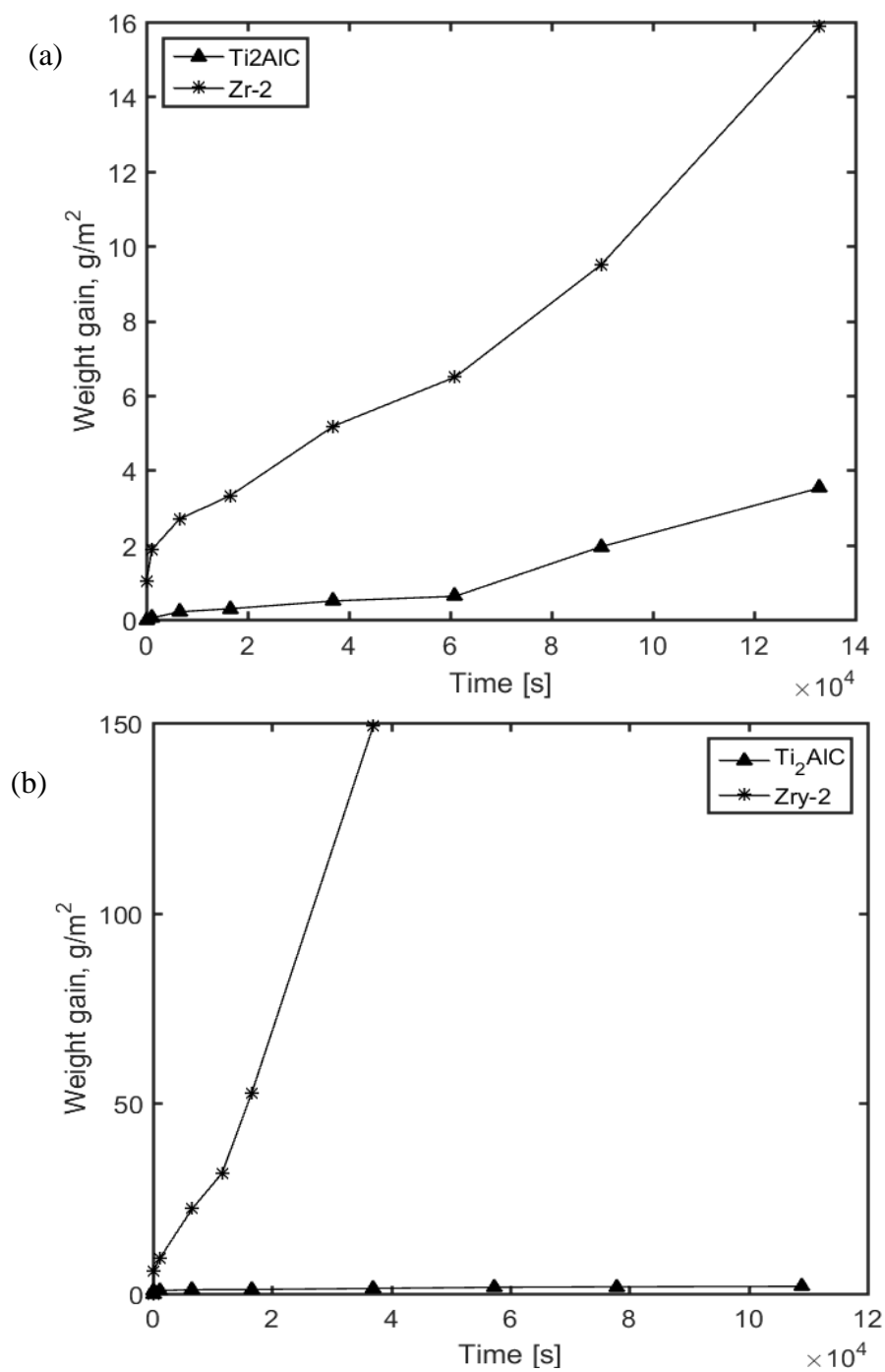


**Figure 5.15.** Comparison of the oxidation kinetics of Ti<sub>2</sub>AlC and Zry-2 in steam at (a) 600, (b) 800, and (c) 1000°C.

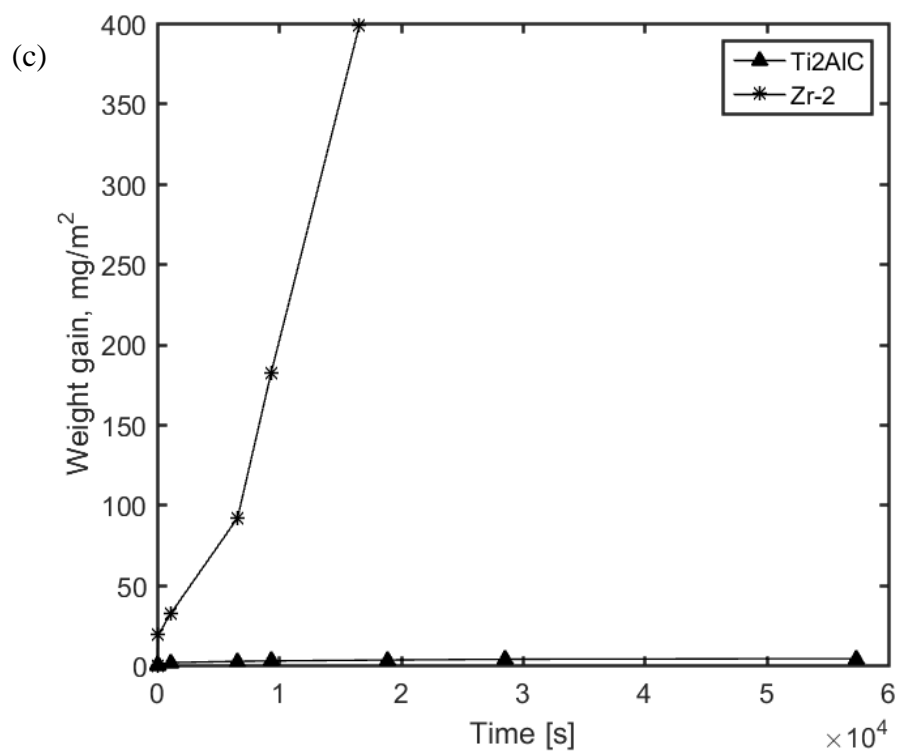


(Figure 5.15 continued)

#### 5.4. Summary

High-temperature oxidation behavior of  $Ti_2AlC$  in steam environment has been investigated.  $Ti_2AlC$  showed an excellent corrosion resistance at all investigated temperatures in steam at the flow rate of 50 mg/s. At 600°C, a discontinuous outer layer of  $TiO_2$  and a continuous inner layer of  $Al_2O_3$  were formed. After oxidation at 800°C, the concentration of  $Al_2O_3$  increased on the surface, and the surface was comprised of a mixture of  $TiO_2$  and  $Al_2O_3$ -rich areas. Volatilization of  $TiO_2$  by steam at higher temperature (1000°C) in the gaseous form of  $TiO_2(OH)$  reduced the concentration of  $TiO_2$  on the surface and  $Al_2O_3$  became the dominant phase.

Although more mass gain was observed at all investigated temperatures when the steam flow rate was increased from 50 mg/s to 100 mg/s, the breakaway phenomenon was only observed at 600°C. The microstructural observation showed that the oxide formed in this condition was porous and possibly cracked, which was in good agreement with oxidation kinetics.

Finally, the oxidation kinetics of  $Ti_2AlC$  was compared to that of Zry-2. At 600°C, the pre-transition parabolic rate constant of  $Ti_2AlC$  was two orders of magnitude lower than that of Zry-2, and the linear post-transition rate constant was lower by one order of magnitude. At all other investigated temperatures, the breakaway occurred rapidly for Zry-2 while no breakaway was observed for  $Ti_2AlC$ .

## 6. CONCLUSION

- The oxidation behavior of the nuclear-grade zirconium alloy (Zry-2) in steam at 600, 800, and 1000°C has been investigated. The maximum oxidation resistance of Zry-2 was observed at 600°C, at which the breakaway oxidation occurred after approximately 16 h. The oxide microstructure transformed from an initially dense and protective to a porous, cracked one as the oxidation time was prolonged or the temperature was increased. The diffusion of alloying elements into the oxide scale was proposed as the main reason for damaging the oxidation resistance of Zry-2.
- Effect of the laser shock peening (LSP) on the oxidation behavior of Zry-2 in air at 600°C has been examined. The surface roughness that was generated by the LSP process in this experiment slightly increased the oxidation kinetics of Zry-2.
- The oxidation kinetics and microstructural evolution of Ti<sub>2</sub>AlC at 600, 800, and 1000°C in the flowing steam has been investigated. The oxidation kinetics of Ti<sub>2</sub>AlC obeyed a parabolic rate law at 600 and 800°C while it followed a cubic rate law at 1000°C. After oxidation at 600°C for 37 h, the oxide microstructure consisted of a discontinuous outer layer of TiO<sub>2</sub> and a continuous inner layer of Al<sub>2</sub>O<sub>3</sub>. After oxidation at 800°C for 30 h, the concentration of Al<sub>2</sub>O<sub>3</sub> increased at the surface to include TiO<sub>2</sub>-rich and Al<sub>2</sub>O<sub>3</sub>-rich areas. At 1000°C for 15 h, steam volatilized TiO<sub>2</sub> in the form of gaseous TiO<sub>2</sub>(OH), leaving an Al<sub>2</sub>O<sub>3</sub>-rich layer on the surface which provided an excellent corrosion protection.
- Effect of the steam flow rate on the oxidation behavior of Ti<sub>2</sub>AlC has also been investigated. The oxidation kinetics increased as the steam flow rate was

increased. Although the oxidation kinetics maintained a parabolic rate law at 600 and 800°C, and a cubic rate law at 1000°C, a breakaway phenomenon was observed after oxidation at 600C for 17 h. This anomalous oxidation behavior was attributed to the rapid transformation of TiO<sub>2</sub> from anatase to rutile-TiO<sub>2</sub> as the steam flow rate was increased, resulting in a rapid change in volume and possible cracks on the surface.

- Finally, the kinetics behavior of Ti<sub>2</sub>AlC in steam at high flow rate was compared to the oxidation of Zry-2 to visualize graphically the huge difference in oxidation behavior.

## 7. FUTURE WORK

Since the discovery of Zirconium alloys for nuclear applications in the 1950s, they have been intensively studied to improve their performance. Further improvement in Zircalloys, if achieved, are unlikely to result in big changes to their performance. Therefore, other materials such as the  $Ti_2AlC$  MAX-phase or  $Ti_3AlC_2/Zr$  composite should be explored for use as alternative nuclear materials.

During the course of oxidation experiments performed on  $Ti_2AlC$  in this study,  $Ti_2AlC$  showed mostly an excellent oxidation resistance at all investigated temperatures. The oxide scale formed after the oxidation of  $Ti_2AlC$  at  $600^\circ C$  in the flowing steam at 50 mg/s was very dense and protective, but a relatively porous and possibly cracked oxide scale was observed as the steam flow rate was doubled. Similarly, several studies have reported this anomalous oxidation behavior at relatively low temperatures (500 and  $600^\circ C$ ).

To validate the utilization of  $Ti_2AlC$  for nuclear applications, the abnormal oxidation behavior of this material at 500 and  $600^\circ C$  must be fully understood. To do so, more oxidation experiments at these temperatures in different steam and air atmospheres are required. Microstructural observation at different time intervals during oxidation, using SEM, EDS, and X-ray diffraction (XRD), could lead to a better understanding of this behavior. This may also require introducing small changes to the parameters used to prepare bulk  $Ti_2AlC$  such as the ratio of mixed powders, pressure and temperature.

Additionally,  $Ti_2AlC$  MAX-phase could be used as an oxidation resistant coating due to its capability of forming a continuous layer of  $Al_2O_3$  in high temperature

environments. Coating a thin layer of  $\text{Ti}_2\text{AlC}$  on Zircalloys, using laser cladding technology, could significantly increase the oxidation resistance of Zircalloys. This is believed to be especially successful for the reason that Zr and  $\text{Ti}_2\text{AlC}$  have very close coefficients of thermal expansion.

The future work could also include spark plasma sintering (SPS) of highly pure  $\text{Ti}_3\text{AlC}_2$  and Zr powders to synthesize  $\text{Ti}_3\text{AlC}_2/\text{Zr}$ . The new composite is believed to possess the potential to combine the excellent properties of both sintered materials such as the high temperature corrosion resistance of  $\text{Ti}_3\text{AlC}_2$  and the low neutron absorption cross-section of Zr. Formation of  $\text{Ti}_x\text{Zr}_{1-x}$  ( $0 < x < 1$ ) solid solution with crystal structure isotypic with bcc Zr and nonstoichiometric  $\text{Ti}_{3-x}\text{AlC}_2$  during sintering at high temperatures ( $\sim 1300^\circ\text{C}$ ) may improve the oxidation resistance of  $\text{Ti}_3\text{AlC}_2$ . The phase diagram of Ti-Zr binary suggests formation of a continuous solid solution  $\text{Ti}_x\text{Zr}_{1-x}$  about  $883^\circ\text{C}$  [120]. In other words, adding a small percentage of Zr ( $\sim 5$  wt% Zr) could change the defect structure of  $\text{Ti}_3\text{AlC}_2$  and increase the Al activity. This, in addition to the weak nature of the chemical bonding between Ti and Al in the crystal structure of  $\text{Ti}_3\text{AlC}_2$ , may change the morphology of the oxide scale during high temperature oxidation, resulting in formation of a protective, dense and thin  $\text{Al}_2\text{O}_3$  scale on the surface of  $\text{Ti}_3\text{AlC}_2/\text{Zr}$ . This idea is based on an experimental study conducted by Cui et al. [121] on sintering  $\text{Ti}_3\text{AlC}_2/\text{W}$  composite.

## 8. REFERENCES

- [1] None, N. (1995). *The History of Nuclear Energy* (No. DOE/NE—0088; DOE/NE-The History of Nuclear Energy\_0). USDOE Office of Nuclear Energy (NE).
- [2] World Nuclear Association (WNA) (2016) “Nuclear Basics”. World-nuclear.org. Retrieved January 21<sup>st</sup>, 2017, from <http://www.world-nuclear.org/Nuclear-Basics/>.
- [2] Goldberg, S. M., & Rosner, R. (2011). Nuclear reactors: Generation to generation. *American Academy of Arts and Sciences, Cambridge, USA*.
- [4] Abram, T., & Ion, S. (2008). Generation-IV nuclear power: A review of the state of the science. *Energy Policy*, 36(12), 4323-4330.
- [5] Toth, F. L., & Rogner, H. H. (2006). Oil and nuclear power: Past, present, and future. *Energy Economics*, 28(1), 1-25.
- [6] Adamantiades, A., & Kessides, I. (2009). Nuclear power for sustainable development: current status and future prospects. *Energy Policy*, 37(12), 5149-5166.
- [7] Lake, J. A. (2002). The fourth generation of nuclear power. *Progress in Nuclear Energy*, 40(3-4), 301-307.
- [8] Shultis, J. K., & Faw, R. E. (2007). *Fundamentals of Nuclear Science and Engineering Second Edition*. CRC press.
- [9] Sanctis, E. D., Monti, S., & Ripani, M. (2016). *Energy from nuclear fission: an Introduction*. Cham: Springer.
- [10] Ferguson, C. D. (2011). *Nuclear energy*. NY, NY: Oxford University Press.
- [11] Knief, R. A. (2008). *Nuclear engineering: theory and technology of commercial nuclear power*. American Nuclear Society.
- [12] United States Nuclear Regulatory Commission (U.S.NRC) (2016) “Power Reactors”. Nrc.org. Retrieved January 21<sup>st</sup>, 2017, from <https://www.nrc.gov/reactors/power.html>.
- [13] United States Nuclear Regulatory Commission (U.S.NRC) (2016) “Power Reactors”. Nrc.org. Retrieved January 22<sup>st</sup>, 2017, from <https://www.nrc.gov/materials/fuel-cycle-fac/stages-fuel-cycle.html>
- [14] United States Nuclear Regulatory Commission. (2008). *Information digest: 2008-2009*. Washington: Division of Planning, Budget and Analysis, Office of the Chief Financial Officer, U.S. Nuclear Regulatory Commission.
- [15] Kok, K. D. (2016). *Nuclear engineering handbook*. Boca Raton: CRC Press/Taylor & Francis Group.
- [16] Glasstone, S., & Sesonske, A. (2012). *Nuclear reactor engineering: reactor systems engineering*. Springer Science & Business Media.

- [17] Azevedo, C. R. F. (2011). Selection of fuel cladding material for nuclear fission reactors. *Engineering Failure Analysis*, 18(8), 1943-1962.
- [18] Nuclear Power for Everybody. (n.d.). Retrieved January 24, 2017, from <http://www.nuclear-power.net/>
- [19] Abram, T., & Ion, S. (2008). Generation-IV nuclear power: A review of the state of the science. *Energy Policy*, 36(12), 4323-4330.
- [20] Cox, B. (2005). Some thoughts on the mechanisms of in-reactor corrosion of zirconium alloys. *Journal of Nuclear materials*, 336(2), 331-368.
- [21] Chang, A. W. (2003). Reactor Grade Zirconium Alloys for Nuclear Waste Disposal. *Technical Data Sheet*.
- [22] Barrett, K., Bragg-Sitton, S., & Galicki, D. (2012). Advanced LWR nuclear fuel cladding system development trade-off study. *Light Water Reactor Sustainability Program, US Department of Energy. Idaho Falls, ID: Idaho National Laboratory*.
- [23] Zinkle, S. J., Terrani, K. A., Gehin, J. C., Ott, L. J., & Snead, L. L. (2014). Accident tolerant fuels for LWRs: A perspective. *Journal of Nuclear Materials*, 448(1), 374-379.
- [24] Bragg-Sitton, S. (2014). Development of advanced accident-tolerant fuels for commercial LWRs. *Nuclear News*, 57(3), 83.
- [25] Goldner, F. (2012, October). Development strategy for advanced LWR fuels with enhanced accident tolerance. In *Enhanced Accident Tolerant LWR Fuels National Metrics Workshop, Germantown, MD*.
- [26] Rickover, H. G., Geiger, L. D., & Lustman, B. (1975). *History of the development of zirconium alloys for use in nuclear reactors*. Energy Research and Development Administration.
- [27] BACZYNSKI, J. R. (2014). *High temperature steam oxidation of titanium-coated Zircaloy-2 and Titanium-Zirconium Alloys* (Doctoral dissertation, University of Illinois at Urbana-Champaign).
- [28] Rebak, R. B., Andresen, P. L., Kim, Y. J., & Dolley, E. J. (2016). Characterization of Advanced Steels as Accident Tolerant Fuel Cladding for Light Water Reactors. *IAEA TECDOC SERIES*, 79.
- [29] Ni, N., Lozano-Perez, S., Jenkins, M. L., English, C., Smith, G. D. W., Sykes, J. M., & Grovenor, C. R. M. (2010). Porosity in oxides on zirconium fuel cladding alloys, and its importance in controlling oxidation rates. *Scripta Materialia*, 62(8), 564-567.
- [30] Ni, N., Hudson, D., Wei, J., Wang, P., Lozano-Perez, S., Smith, G. D. W., ... & Cottis, R. (2012). How the crystallography and nanoscale chemistry of the metal/oxide interface develops during the aqueous oxidation of zirconium cladding alloys. *Acta Materialia*, 60(20), 7132-7149.

- [31] Ni, N., Lozano-Perez, S., Sykes, J., & Grovenor, C. (2011). Quantitative EELS analysis of zirconium alloy metal/oxide interfaces. *Ultramicroscopy*, 111(2), 123-130.
- [32] Adamson, R., Garzarolli, F., Cox, B., Strasser, A., & Rudling, P. (2007). Corrosion mechanisms in zirconium alloys. *ZIRAT12 Special Topic Report*.
- [33] Zirconium alloy. (2015). In Wikipedia. Retrieved March 28, 2016 from [https://en.wikipedia.org/wiki/Zirconium\\_alloy](https://en.wikipedia.org/wiki/Zirconium_alloy)
- [34] Whitmarsh, C. L. (1962). *Review of Zircaloy-2 and Zircaloy-4 properties relevant to NS Savannah reactor design* (No. ORNL-3281). Oak Ridge National Lab., Tenn..
- [35] Todreas, N. E., & Kazimi, M. S. (2011). *Nuclear Systems Volume 1: Thermal Hydraulic Fundamentals*
- [36] Valdés-Parada, F. J., Romero-Paredes, H., & Espinosa-Paredes, G. (2013). Numerical analysis of hydrogen generation in a BWR during a severe accident. *Chemical Engineering Research and Design*, 91(4), 614-624.
- [37] Zinkle, S. J., Terrani, K. A., Gehin, J. C., Ott, L. J., & Snead, L. L. (2014). Accident tolerant fuels for LWRs: A perspective. *Journal of Nuclear Materials*, 448(1), 374-379.
- [38] Hirano, M., Yonomoto, T., Ishigaki, M., Watanabe, N., Maruyama, Y., Sibamoto, Y., ... & Moriyama, K. (2012). Insights from review and analysis of the Fukushima Dai-ichi accident: Fukushima NPP accident related. *Journal of Nuclear Science and Technology*, 49(1), 1-17.
- [39] Allen, T. R., Konings, R. J. M., & Motta, A. T. (2012). 5.03 corrosion of zirconium alloys. *Comprehensive nuclear materials*, 49-68.
- [40] Motta, A. T., Couet, A., & Comstock, R. J. (2015). Corrosion of Zirconium Alloys Used for Nuclear Fuel Cladding. *Annual Review of Materials Research*, 45, 311-343.
- [41] Jones, D. A. (1992). *Principles and prevention of corrosion*. Macmillan.
- [42] Billot, P., Cox, B., Ishigure, K., Johnson, A. B., Lemaignan, C., Nechaev, A. F., ... & Sukhanov, G. I. (1993). Corrosion of zirconium alloys in nuclear power plants. In *TECDOC-684*. International Atomic Energy Agency (IAEA).
- [43] Causey, Rion A., Coowgill, Donald F, and Nilson, Robert H. (2005). Review of the oxidation Rate of zirconium Alloys. *Sandia National Laboratories*.
- [44] Duriez, C., Dupont, T., Schmet, B., & Enoch, F. (2008). Zircaloy-4 and M5® high temperature oxidation and nitriding in air. *Journal of Nuclear Materials*, 380(1), 30-45.
- [45] T. Ahmed, L.H. Keys, Breakaway oxidation of zirconium and its alloys – Review, *J. Less-Common Met.* 39 (1975) 99–107.
- [46] Guerain, M., Duriez, C., Grosseau-Poussard, J. L., & Mermoux, M. (2015). Review of stress fields in Zirconium alloys corrosion scales. *Corrosion Science*, 95, 11-21.

- [47] Oskarsson, M. (2000). Study on the Mechanisms for Corrosion and Hydriding of Zircaloy.
- [48] Cox, B. (1969). Processes occurring during the breakdown of oxide films on zirconium alloys. *Journal of Nuclear Materials*, 29(1), 50-66.
- [49] Coindreau, O., Duriez, C., & Ederli, S. (2010). Air oxidation of Zircaloy-4 in the 600–1000° C temperature range: Modeling for ASTEC code application. *Journal of Nuclear Materials*, 405(3), 207-215.
- [50] Zhou, B. X. (1989, January). Electron microscopy study of oxide films formed on Zircaloy-2 in superheated steam. In *Zirconium in the Nuclear Industry: Eighth International Symposium*. ASTM International.
- [51] Wadman, B. (1993). *Mechanisms of uniform corrosion of zirconium alloys in water and steam*. Chalmers University of Technology.
- [52] Steinbrück, M. (2009). Prototypical experiments relating to air oxidation of Zircaloy-4 at high temperatures. *Journal of Nuclear Materials*, 392(3), 531-544.
- [53] Selmi, N., & Sari, A. (2013). Study of oxidation kinetics in air of zircaloy-4 by in situ X-ray diffraction. *Advances in Materials Physics and Chemistry*, 3(02), 168.
- [54] Idarraga, I., Mermoux, M., Duriez, C., Crisci, A., & Mardon, J. P. (2012). Raman investigation of pre-and post-breakaway oxide scales formed on Zircaloy-4 and M5® in air at high temperature. *Journal of Nuclear Materials*, 421(1), 160-171.
- [55] Fendrych, F., Taylor, A., Peksa, L., Kratochvilova, I., Vlcek, J., Rezacova, V., ... & Nesladek, M. (2010). Growth and characterization of nanodiamond layers prepared using the plasma-enhanced linear antennas microwave CVD system. *Journal of Physics D: Applied Physics*, 43(37), 374018.
- [56] Gong, W., Zhang, H., Qiao, Y., Tian, H., Ni, X., Li, Z., & Wang, X. (2013). Grain morphology and crystal structure of pre-transition oxides formed on Zircaloy-4. *Corrosion Science*, 74, 323-331.
- [57] Gong, W., Zhang, H., Wu, C., Tian, H., & Wang, X. (2013). The role of alloying elements in the initiation of nanoscale porosity in oxide films formed on zirconium alloys. *Corrosion Science*, 77, 391-396.
- [58] Baek, J. H., & Jeong, Y. H. (2008). Breakaway phenomenon of Zr-based alloys during a high-temperature oxidation. *Journal of Nuclear Materials*, 372(2), 152-159.
- [59] Yurek, G. J., Cathcart, J. V., & Pawel, R. E. (1976). Microstructures of the scales formed on zircaloy-4 in steam at elevated temperatures. *Oxidation of Metals*, 10(4), 255-276.
- [60] Takeda, K., & Anada, H. (2000). Zirconium in the Nuclear Industry: Twelfth International Symposium. *ASTM STP*, 1354, 592.

- [61] Garde, A. M., Pati, S. R., Krammen, M. A., Smith, G. P., & Endter, R. K. (1994, January). Corrosion behavior of Zircaloy-4 cladding with varying tin content in high-temperature pressurized water reactors. In *Zirconium in the Nuclear Industry: Tenth International Symposium*. ASTM International.
- [62] Zhang, X. Y., Shi, M. H., Li, C., Liu, N. F., & Wei, Y. M. (2007). The influence of grain size on the corrosion resistance of nanocrystalline zirconium metal. *Materials Science and Engineering: A*, 448(1), 259-263.
- [63] Platt, P., Allen, V., Fenwick, M., Gass, M., & Preuss, M. (2015). Observation of the effect of surface roughness on the oxidation of Zircaloy-4. *Corrosion Science*, 98, 1-5.
- [64] Ni, N., Lozano-Perez, S., Sykes, J. M., Smith, G. D. W., & Grovenor, C. R. M. (2011). Focussed ion beam sectioning for the 3D characterisation of cracking in oxide scales formed on commercial ZIRLO™ alloys during corrosion in high temperature pressurised water. *Corrosion Science*, 53(12), 4073-4083.
- [65] Sawarn, T. K., Banerjee, S., Samanta, A., Rath, B. N., & Kumar, S. (2015). Study of oxide and  $\alpha$ -Zr (O) growth kinetics from high temperature steam oxidation of Zircaloy-4 cladding. *Journal of Nuclear Materials*, 467, 820-831.
- [66] Opila, E. (2013). High Temperature Materials Corrosion Challenges for Energy Conversion Technologies. *Electrochemical Society Interface*, 69.
- [67] Birchley, J., & Fernandez-Moguel, L. (2012). Simulation of air oxidation during a reactor accident sequence: Part 1—Phenomenology and model development. *Annals of Nuclear Energy*, 40(1), 163-170.
- [68] Kratochvílová, I., Škoda, R., Škarohlíd, J., Ashcheulov, P., Jäger, A., Racek, J., ... & Shao, L. (2014). Nanosized polycrystalline diamond cladding for surface protection of zirconium nuclear fuel tubes. *Journal of Materials Processing Technology*, 214(11), 2600-2605.
- [69] Maier, B. R., Garcia-Diaz, B. L., Hauch, B., Olson, L. C., Sindelar, R. L., & Sridharan, K. (2015). Cold spray deposition of Ti 2 AlC coatings for improved nuclear fuel cladding. *Journal of Nuclear Materials*, 466, 712-717.
- [70] Lin, Z. J., Zhuo, M. J., Zhou, Y. C., Li, M. S., & Wang, J. Y. (2006). Microstructural characterization of layered ternary Ti 2 AlC. *Acta materialia*, 54(4), 1009-1015.
- [71] Wang, X. H., & Zhou, Y. C. (2003). High-temperature oxidation behavior of Ti 2 AlC in air. *Oxidation of Metals*, 59(3), 303-320.
- [72] Radovic, M., & Barsoum, M. W. (2013). MAX phases: bridging the gap between metals and ceramics. *American Ceramics Society Bulletin*, 92(3), 20-27.
- [73] Jeitschko, W., Nowotny, H. & Benesovsky, F. Monatshefte für Chemie (1963) 94: 672.
- [74] Zhou, Y., & Sun, Z. (2000). Electronic structure and bonding properties of layered machinable Ti 2 AlC and Ti 2 AlN ceramics. *Physical Review B*, 61(19), 12570.

- [75] Wang, X. H., & Zhou, Y. C. (2002). Intermediate-temperature oxidation behavior of Ti<sub>2</sub>AlC in air. *Journal of Materials Research*, 17(11), 2974-2981.
- [76] Barsoum, M. W., Brodtkin, D., & El-Raghy, T. (1997). Layered machinable ceramics for high temperature applications. *Scripta Materialia*, 36(5), 535-541.
- [77] Barsoum, M. W., El-Raghy, T., & Ali, M. (2000). Processing and characterization of Ti<sub>2</sub>AlC, Ti<sub>2</sub>AlN, and Ti<sub>2</sub>AlC<sub>0.5</sub>N<sub>0.5</sub>. *Metallurgical and Materials Transactions A*, 31(7), 1857-1865.
- [78] Wang, X., & Zhou, Y. (2002). Solid-liquid reaction synthesis and simultaneous densification of polycrystalline Ti<sub>2</sub>AlC. *Zeitschrift für Metallkunde*, 93(1), 66-71.
- [79] Tang, C., Steinbrück, M., Große, M., Bergfeldt, T., & Seifert, H. J. (2017). Oxidation behavior of Ti<sub>2</sub>AlC in the temperature range of 1400° C–1600° C in steam. *Journal of Nuclear Materials*.
- [80] Basu, S., Obando, N., Gowdy, A., Karaman, I., & Radovic, M. (2011). Long-term oxidation of Ti<sub>2</sub>AlC in air and water vapor at 1000–1300 C temperature range. *Journal of the Electrochemical Society*, 159(2), C90-C96.
- [81] Smialek, J. L. (2017). Environmental resistance of a Ti<sub>2</sub>AlC-type MAX phase in a high pressure burner rig. *Journal of the European Ceramic Society*, 37(1), 23-34.
- [82] Wang, X. H., & Zhou, Y. C. (2003). Oxidation behavior of Ti<sub>3</sub>AlC<sub>2</sub> at 1000–1400 C in air. *Corrosion Science*, 45(5), 891-907.
- [83] Lin, Z. J., Li, M. S., Wang, J. Y., & Zhou, Y. C. (2008). Influence of water vapor on the oxidation behavior of Ti<sub>3</sub>AlC<sub>2</sub> and Ti<sub>2</sub>AlC. *Scripta Materialia*, 58(1), 29-32.
- [84] Cui, B., Jayaseelan, D. D., & Lee, W. E. (2011). Microstructural evolution during high-temperature oxidation of Ti<sub>2</sub>AlC ceramics. *Acta Materialia*, 59(10), 4116-4125.
- [75] Byeon, J. W., Liu, J., Hopkins, M., Fischer, W., Garimella, N., Park, K. B., ... & Sohn, Y. H. (2007). Microstructure and residual stress of alumina scale formed on Ti<sub>2</sub>AlC at high temperature in air. *Oxidation of metals*, 68(1-2), 97-111.
- [86] Barsoum, M. W., Tzenov, N., Procopio, A., El-Raghy, T., & Ali, M. (2001). Oxidation of Ti<sub>n+1</sub>AlX<sub>n</sub> (n= 1 3 and X= C, N): II. Experimental Results. *Journal of The Electrochemical Society*, 148(8), C551-C562.
- [87] Sonestedt, M., Frodelius, J., Sundberg, M., Hultman, L., & Stiller, K. (2010). Oxidation of Ti<sub>2</sub>AlC bulk and spray deposited coatings. *Corrosion Science*, 52(12), 3955-3961.
- [88] Cui, B. (2011). *Microstructural evolution and oxidation behavior of spark plasma sintered Mn<sub>1-x</sub>Al<sub>x</sub>N ceramics* (Doctoral dissertation, Imperial College London).
- [89] Nguyen, Q. N. (2008). *High temperature volatility and oxidation measurements of titanium and silicon containing ceramic materials* (Doctoral dissertation, Cleveland State University).

- [90] Sundberg, M., Malmqvist, G., Magnusson, A., & El-Raghy, T. (2004). Alumina forming high temperature silicides and carbides. *Ceramics International*, 30(7), 1899-1904.
- [91] Barsoum, M. W. (2001). Oxidation of  $Ti_{n+1}AlX_n$  ( $n=1, 3$  and  $X=C, N$ ) I. Model. *Journal of the Electrochemical Society*, 148(8), C544-C550.
- [92] Angle, J. P., Morgan, P. E., & McCartney, M. L. (2013). Water Vapor-Enhanced Diffusion in Alumina. *Journal of the American Ceramic Society*, 96(11), 3372-3374.
- [93] Hua, Y., Rong, Z., Ye, Y., Chen, K., Chen, R., Xue, Q., & Liu, H. (2015). Laser shock processing effects on isothermal oxidation resistance of GH586 superalloy. *Applied Surface Science*, 330, 439-444.
- [94] Ren, N. F., Yang, H. M., Yuan, S. Q., Wang, Y., Tang, S. X., Zheng, L. M., ... & Dai, F. Z. (2014). High temperature mechanical properties and surface fatigue behavior improving of steel alloy via laser shock peening. *Materials & Design*, 53, 452-456.
- [95] Gomez-Rosas, G., Rubio-Gonzalez, C., Ocaña, J. L., Molpeceres, C., Porro, J. A., Chi-Moreno, W., & Morales, M. (2005). High level compressive residual stresses produced in aluminum alloys by laser shock processing. *Applied Surface Science*, 252(4), 883-887.
- [96] Rubio-González, C., Gomez-Rosas, G., Ocaña, J. L., Molpeceres, C., Banderas, A., Porro, J., & Morales, M. (2006). Effect of an absorbent overlay on the residual stress field induced by laser shock processing on aluminum samples. *Applied Surface Science*, 252(18), 6201-6205.
- [97] Brockman, R. A., Braisted, W. R., Olson, S. E., Tenaglia, R. D., Clauer, A. H., Langer, K., & Shepard, M. J. (2012). Prediction and characterization of residual stresses from laser shock peening. *International Journal of Fatigue*, 36(1), 96-108.
- [98] Wang, F., Zhang, C., Lu, Y., Nastasi, M., & Cui, B. (2016). Laser Shock Processing of Polycrystalline Alumina Ceramics. *Journal of the American Ceramic Society*.
- [99] Instruments, N. (2017). Nanoscience instruments. Retrieved February 15, 2017, from <http://www.nanoscience.com/>
- [100] Williams, D. B. and Carter, C. B. (2009) *Transmission Electron Microscopy*. Springer Science & Business Media, New York.
- [101] NERcF FEI Helios NanoLab 660. (2017). Retrieved February 16, 2017, from <http://engineering.unl.edu/nercf/fei-helios-fibsem-650/>
- [102] University of Nebraska-Lincoln | Web Developer Network. (n.d.). Electron Nanoscopy Instrumentation Facility. Retrieved February 16, 2017, from <http://ncmn.unl.edu/enif/home>
- [103] "X-Ray Fluorescence (XRF): Understanding Characteristic X-Rays" [PDF]. Retrieved February 16, 2017.

- [104] Baek, J. H., & Jeong, Y. H. (2008). Breakaway phenomenon of Zr-based alloys during a high-temperature oxidation. *Journal of Nuclear Materials*, 372(2), 152-159.
- [105] Denny, A. J. (1996). Principles and prevention of corrosion. *Prentice-Hall Inc., Upper Saddle River, NJ*, 76-90.
- [106] Duriez, C., Dupont, T., Schmet, B., & Enoch, F. (2008). Zircaloy-4 and M5® high temperature oxidation and nitriding in air. *Journal of Nuclear Materials*, 380(1), 30-45.
- [107] Coindreau, O., Duriez, C., & Ederli, S. (2010). Air oxidation of Zircaloy-4 in the 600–1000° C temperature range: Modeling for ASTEC code application. *Journal of Nuclear Materials*, 405(3), 207-215.
- [108] Hua, Y., Bai, Y., Ye, Y., Xue, Q., Liu, H., Chen, R., & Chen, K. (2013). Hot corrosion behavior of TC11 titanium alloy treated by laser shock processing. *Applied Surface Science*, 283, 775-780.
- [109] Trdan, U., & Grum, J. (2014). SEM/EDS characterization of laser shock peening effect on localized corrosion of Al alloy in a near natural chloride environment. *Corrosion Science*, 82, 328-338.
- [110] Montross, C. S., Wei, T., Ye, L., Clark, G., & Mai, Y. W. (2002). Laser shock processing and its effects on microstructure and properties of metal alloys: a review. *International Journal of Fatigue*, 24(10), 1021-1036.
- [111] Fabbro, R., Peyre, P., Berthe, L., & Scherpereel, X. (1998). Physics and applications of laser-shock processing. *Journal of laser applications*, 10(6), 265-279.
- [112] Petan, L., Ocaña, J. L., & Grum, J. (2016). Effects of Laser Shock Peening on the Surface Integrity of 18% Ni Maraging Steel. *Strojniški vestnik-Journal of Mechanical Engineering*, 62(5), 291-298.
- [113] Quadackers, W. J. (1990). Growth mechanisms of oxide scales on ODS alloys in the temperature range 1000–1100 C. *Materials and Corrosion*, 41(12), 659-668.
- [114] Rao, J. C., Pei, Y. T., Yang, H. J., Song, G. M., Li, S. B., & De Hosson, J. T. M. (2011). TEM study of the initial oxide scales of Ti 2 AlC. *Acta Materialia*, 59(13), 5216-5223.
- [115] Liao, T., Wang, J., & Zhou, Y. (2008). Ab initio modeling of the formation and migration of monovacancies in Ti 2 AlC. *Scripta Materialia*, 59(8), 854-857.
- [116] Du, Y., Liu, J. X., Gu, Y., Wang, X. G., Xu, F., & Zhang, G. J. (2017). Anisotropic corrosion of Ti 2 AlC and Ti 3 AlC 2 in supercritical water at 500°C. *Ceramics International*.
- [117] Lee, K. S., & Park, I. S. (2003). Anatase-phase titanium oxide by low temperature oxidation of metallic Ti thin film. *Scripta materialia*, 48(6), 659-663.
- [118] Hanaor, D. A., & Sorrell, C. C. (2011). Review of the anatase to rutile phase transformation. *Journal of Materials science*, 46(4), 855-874.

[119] Shannon, R. D. (1964). Phase Transformation Studies in TiO<sub>2</sub> Supporting Different Defect Mechanisms in Vacuum-Reduced and Hydrogen-Reduced Rutile. *Journal of Applied Physics*, 35(11), 3414-3416.

[120] Kumar, K. H., Wollants, P., & Delacy, L. (1994). Thermodynamic assessment of the Ti-Zr system and calculation of the Nb-Ti-Zr phase diagram. *Journal of alloys and compounds*, 206(1), 121-127.

[121] Cui, B., Zapata-Solvas, E., Reece, M. J., Wang, C. A., & Lee, W. E. (2013). Microstructure and High-temperature Oxidation Behavior of Ti<sub>3</sub>AlC<sub>2</sub>/W Composites. *Journal of the American Ceramic Society*, 96(2), 584-591.

## 9. LIST OF PUBLICATIONS

[1] Smoqi, Z., Wang, F. and Cui, B. Oxidation Mechanism of Ti<sub>2</sub>AlC in Steam Environment at 600 - 1000°C, will be submitted to Journal of the American Ceramic Society.